THE UNIVERSITY *of* EDINBURGH

Damaged Reinforced Concrete Structures in Fire

Adam Ervine
Department of Civil Engineering
University of Edinburgh

A thesis submitted for the degree of
PhilosophiæDoctor (PhD)

2012

1. Reviewer (external): Prof. Yong Wang

2. Reviewer (internal): Dr. Yong Lu

Day of the defence: 15th March 2012

Abstract

It is crucial for a building to maintain structural stability when subjected to multiple and sequential extreme loads. Safety and economic considerations dictate that structures are built to resist extreme events, such as a earthquakes, impacts, blasts or fires, without collapse and to provide adequate time for evacuation of the occupants. However, during such events, some structural damage may be permissible. Design codes do not account for the scenario where two extreme events occur consecutively on a structure nor do they address the situation of the structure having some initial damage prior to being subjected to a fire load.

This work begins by detailing the major inconsistancies between designing reinforced concrete structures for extreme mechanical loads and designing for fire. The material behaviour and traits of the constitutive parts (i.e. the concrete and the steel), including post yielding behaviour, thermal relationships and their interaction with each other are all explored in detail.

Comprehensive experimental and numerical investigations are undertaken to determine whether, and to what extent, phenomena such as tensile cracking and loss of the concrete cover affect the local and global fire resistance of a member or structure.

The thermal propagation through tensile cracks in reinforced concrete beams is examined experimentally. A comparison is made between the rate of thermal propagation through beams that are undamaged and beams that have significant tensile cracking . The results show that, although small differences occur, there is no significant change in the rate of thermal propagation

through the specimens. Consequently, it is concluded that the effects of tensile cracking on the thermal propagation through concrete can be ignored in structural analyses. Significantly this means that analyses of heated concrete structures which are cracked can be carried out with heat-transfer and mechanical analyses being conducted sequentially, as is currently normal and fully-coupled thermo-mechanical analyses are not required.

The loss of concrete cover and the impact on the thermal performance is examined numerically. A comparison is made of the thermal propagation, beam deflections and column rotations between structures that are undamaged and structures that have partial cover loss in a variety of locations and magnitudes. Results show that any loss of cover can lead to unsymmetrical heating, causing larger deflections in both vertical and horizontal directions, which can result in a more critical scenario. It is concluded that the effect of cover loss on the thermal performance of the structure is extremely significant.

A new approach to numerically simulating the loss of cover by mechanical means from a member is developed. This new approach provides the user with an extremely flexible yet robust method for simulating this loss of cover. The application of this method is then carried out to show its effectiveness.

A large experimental study carried out at the "Indian Institute of Technology, Roorkee" and separately numerically modelled at the "University of Edinburgh". Unfortunately, due to unforseen curcumstances, the experimenatal data available is limited at this time and as a result the validation of the numerical simulation is limited.

Through these investigations it is clear that it is necessary to develop a method in enhance the stability and integrity of the concrete when subjected to the scenario of a fire following another mechanically extreme event.

Therefore, finally a method is proposed and experimentally investigated into the use of fibres to increase the post crushing cohesiveness of the concrete when subjected to thermal loads. Results show that the fibrous members display an increased thermal resistance by retaining their concrete cover through an enhanced post crushing cohesion. From this investigation, it is concluded that the use of fibrous concrete is extremely beneficial for the application of enhancing the performance under extreme sequential mechanical and thermal loading.

Acknowledgements

I would like to thank Dr. Martin Gillie and Dr. Pankaj, my supervisors, for their guidance and support throughout the course of my research.

The financial support of EPSRC and the BRE trust fund is gratefully acknowledged, as well as the help and perspective offered from my industrial colleagues, Dr. Danny Hopkins, Debbie Smith and Tom Lennon.

An extended thanks to the John Muir building and entire Edinburgh University Fire group. It's been emotional!

I would like to give a special thanks to Derek Jardine, Jim Hutchison, Michal Krajcovic and Thomas Lowry for the huge amount of support and advice they gave throughout the experimental investigations.

Finally, thanks to my Mum. You have been indispensable when it came time to the arduous task of writing.

Declaration

I hereby declare that:

(a) the thesis has been composed entirely by myself under the supervision of Dr. M. Gillie and Dr. P. Pankaj;

(b) the work is my own, except where clearly indicated, and originated in the School of Engineering at The University of Edinburgh;

(c) the work has not been submitted for any other degree or professional qualification.

Signed:

Adam Ervine

University of Edinburgh

Date submitted

Publications

Journal Papers

Ervine, A., Gillie, M., Stratford, T.J., Pankaj, P., 2011, *Thermal Propagation through Tensile Cracks in Reinforced Concrete*, Journal of Materials in Civil Engineering, posted ahead of print 3 November 2011.

Conference Papers

Ervine, A., Gillie, M., Stratford, T.J., Pankaj, P., 2011, *Thermal Diffusivity of Tensile Cracked Concrete*, Application of Structural Fire Design, Prague, Czech Republic

Ervine, A., Gillie, M., Stratford, T.J., Pankaj, P., 2010, *Behaviour of Earthquake Damaged Reinforced Concrete Structures in Fire*, 9th US and 10th Canadian Conference on earthquake Engineering, Toronto, Canada

Ervine, A., Gillie, M., Pankaj, P., 2009, *Behaviour of Earthquake Damaged Reinforced Concrete*, Structures in Fire, Michigan, USA

Contents

List of Figures

LIST OF FIGURES

List of Tables

Chapter 1

Introduction

The fundamental concern during the design of building structures is to ensure the life safety of its occupants. During extreme loads such as earthquakes, impacts, fire, etc. the design needs to provide adequate time for evacuation of the occupants and extend to ensuring the life safety of any emergency services. In addition to this, the design should aim to minimise structural and non-structural damage to prevent collapse and hence protect the structure and any surrounding infrastructure.

When designing for a fire scenario, adequate fire resistance is required to prevent failure and to ensure safety of the occupants. In terms of a reinforced concrete structure, the concrete is generally accepted as a non-combustible material and will act as a thermal insulator. Therefore the fire resistance is typically defined in terms of the temperature of reinforcement and hence the concrete cover provided. The required concrete cover to achieve a certain fire resistance can be obtained directly from design codes (Eurocode 2004) or can be obtained using some sequential thermal mechanical numerical analysis. However, thus far both approaches have a severe fundamental drawback in that they do not take into account a scenario whereby the concrete cover has undergone some damage prior to a thermal load.

1.1 The driving question

Structural loads such as earthquakes, impacts and blasts can cause widespread damage to structural and non-structural components. Economic considerations dictate that for designing reinforced concrete structures under these extreme loads there is an allowable capacity for plastic deformations to occur. Due to the nature of reinforced concrete, these allowable plastic deformations can bring about localised effects such as tensile cracking or compressive crushing and removal of the concrete cover. These localised effects can be devastating in terms of the fire resistance of the structure as the concrete cover may have been become compromised. The thermal insulation properties of the concrete cover may have become reduced or the cover may be removed completely leading to direct heating of the reinforcement.

Here lies the fundamental and major inconsistency between the design methods for fire and other extreme events that cause mechanical damage.

This research aims to address the issue of reinforced concrete structures being subjected multiple and sequential extreme loads with particular reference to a fire following another extreme mechanical event. The section below details a variety of examples where a fire has followed another mechanically extreme event.

1.2 Historical examples of post-earthquake fires

Throughout history there are many examples where fires have broken out as a result of a subsequent mechanically extreme event. This section presents documented examples of when fires have followed earthquakes with costly consequences. Due to high density, built up urban areas have been more prone to post earthquake fires. Bagchi et al. (2008) and Scawthorn et al. (2005) provide a comprehensive overview of the post-earthquake fires from an emergency response, societal preparedness and disaster mitigation point of view. In addition they include discussions of the major historical fire following earthquake events such as the 1906 San Francisco and the 1923 Tokyo earthquakes that led to major widespread fire resulting in far greater damage and loss of life than

caused by the original shaking. Other notable events where major conflagration broke out include the 1989 Loma Prieta, 1994 Northbridge and 1995 Kobe earthquake.

1.3 Research Outline

The aim of this research is to provide a better understanding of the structural behaviour of reinforced concrete structures, both globally and locally when subjected to multiple extreme loading scenarios.

This was achieved through a series of experimental and numerical investigations with the aims of:

a) defining the modes of local damage that occur within reinforced concrete structure when subjected to extreme mechanical events (i.e. large displacements, stresses and strains) and how these can be effectively modelled,

b) understanding to what extent these modes affect the thermal resistance and thermal response of the structure with validation from experimental results, and

c) providing a method, if required, to retain and/or enhance the stability and integrity of the structure when subjected to multiple extreme events.

1.4 Chapter Outline

Chapter 1 - Introduction - A brief overview of the thesis and the reason for undertaking the research is given, highlighting the major issues and conflicts between different design methods for reinforced concrete structures under extreme loading conditions.

Chapter 2 - Factors affecting material and structural behaviour and how they can be modelled - An overview of the material and structural properties of steel and concrete are discussed. This includes rupture of the steel, compressive crushing and

tensile cracking of the concrete and the interaction between these materials. Furthermore, the effect of tenmperature are also briefly discussed with reference to strength and stiffness degradation and how geometrical phenomenon, such as tensile cracking, may influence. In addtion to this, the numerical simulation of the above aspects is discussed.

Chapter 3 - Thermal propagation through tensile cracks in reinforced concrete - An investigation is undertaken into the effects of excessive tensile cracking on the thermal propagation through a reinforced concrete member. This was carried out in the form of a comprehensive experimental study where multiple beams underwent some flexural loading resulting in tensile cracking and were then subjected to a thermal load while the temperature throughout the section was recorded.

Chapter 4 - Compression damage in reinforced concrete and its effects on the thermo-mechanical behaviour - An investigation is undertaken into the effects of partial removal of the concrete cover on the global behaviour of a reinforced concrete structure. This investigation is carried out in the form of a comprehensive numerical feasibility study, where a reinforced concrete portal frame is subjected to a variety of cover loss scenarios. Furthermore, a method is developed for automatically determining the location and magnitude of the loss of cover for use in numerical modelling.

Chapter 5 - Case Study: Global modelling of a reinforced concrete structure under multiple extreme loading - This chapter utilises the knowledge acquired in Chapter 3 and Chapter 4 with the objectives of accurately numerically modelling (both thermally and mechanically) an on-going experimental research program where the behaviour of a damaged full scale reinforced concrete structure subjected to a fire loading is investigated. Due to unforseen curcumstances, limited experimental data is available for full verification.

Chapter 6 - Fibre implementation for improved concrete cohesion - This chapter utilises the knowledge acquired in Chapter 4 and Chapter 5 to design a method of retaining the fire resistance of a reinforced concrete structure when subjected to multiple extreme loadings. This was carried out in the form of a comprehensive experimental study where the composition of multiple beams was altered with the use of fibres with the aim of improving the cohesiveness of crushed concrete.

Chapter 7 - Conclusions and further work - This chapter comprises a discussion of the conclusions of the research and their implications, together with suggestions for further work to be undertaken.

Appendix A - Concrete mix for use in experimentation - This appendix provides the full concrete design for the experimental programmes detailed in Chapter 3 and Chapter 4. It provides a summary of the main constitutive ingredients (cement, coarse and fine aggregates and water).

Appendix B - Water absorption of synthetic fibres - Synthetic fibres will absorb some of the free water added to the concrete mix, therefore this appendix investigates the absorption capabilities and provides a summary of the extra water to be added to the mix to accommodate this.

Appendix C - Thermocouple placement techniques - This appendix illustrates the methods used for the placement of the thermocouples embedded within the concrete specimens.

Appendix D - Calculation of necking and rupture strains in reinforcing steel - An experimental investigation is undertaken to determine the stress-strain relationship of steel under excessive loading. The strains are recorded for the phenomena of necking and rupture.

Appendix E - Digital imaging correlation technique - This appendix outlines the digital imaging correlation technique used for determining the crack widths in Chapter 3 and the compressive strains in Chapter 6. This method was also used when calculating useful values for the determination of the loss of concrete cover as detailed in Chapter. 4.

Appendix F - Study of the radiant heat flux uniformity from the radiant heating panels - This appendix presents a short study on the homogeneity of the radiant panels used in Chapter 6. A number of factors are taken into account and investigated to obtain a relatively high and uniform heat flux to be applied to the beams under investigation.

Appendix G - Numerical convergence study on the element density required for the accurate modelling of bending using solid elements - Solid elements are quite stiff in bending, therefore a sufficient element mesh density is required to accurately calculate the bending. This appendix outlines a numerical convergence study performed to determine the element mesh density to produce a suitably accurate result.

Appendix H - Discussion on the element type for the modelling of reinforced concrete structures under extreme loading conditions - A discussion is presented on the abilities and flaws of different elements and modelling techniques within ABAQUS and their suitability for the simulation of reinforced concrete under multiple extreme events.

Appendix I - Numerical model material inputs, including subroutine simulating loss of concrete cover - This appendix provides the full detailed material model values used throughout the thesis. In addition, the subroutine to calculate the

loss of concrete cover is also reported.

Appendix J - Calculations of the applied loading for the "case study" frame - The calculations of the vertical loading that are to be applied to the numerical simulation of the case study frame are detailed in this appendix.

Chapter 2

Factors affecting material and structural behaviour and how they can be modelled

2.1 Introduction

Designing a reinforced concrete structure to withstand extreme mechanical or thermal loads and understanding the local and global behaviour in such an event first requires knowledge of how the constitutive materials (steel and concrete) behave. This chapter aims to give a brief overview of:

(a) the material behaviour of steel and concrete subjected to large stresses and strains and what implications this has for the onset and progression of damage,

(b) the material and structural behaviour of steel and concrete subjected to increasing temperatures,

(c) the implications and consequences when considering the scenario of a fire following some mechanically extreme event, and

(d) how the above factors are generally numerically simulated.

It should be noted that the material properties for both steel and concrete are based on the data obtained from material testing for the full scale tests detailed in Chapter

5. Eurocode 2 Part 1-2 (2004) is then used to extrapolate the properties for high temperatures and for the thermal properties. The reason for this is that, although the Eurocode are utilised for design purposes, they still provide a clear and coherent set of general material properties (mechanical and thermal) for both reinforcing steel and concrete that incorporate temperature dependence and provide allowances for softening behaviour.

It should also be noted that this chapter only provides the frame work of the material model. Full details of the numeric values of the material properties are listed in Appendix I.

2.2 Steel reinforcement

The material behaviour of steel reinforcement at ambient temperatures and under normal loading conditions is usually considered to be relatively simple. However, it can become much more complex when subjected to extreme conditions such as those that occur during earthquakes, impacts, blasts or fires. The effects brought about by these events can cause loss of strength and stiffness and excessive stresses and strains to develop that can lead to rupture of the reinforcing steel resulting in a reduced load carrying capacity.

2.2.1 Stress-strain relationship

Reinforcing steel properties at ambient temperatures have been well researched and documented (Cooke 1988, Elghazouli et al. 2009, Kirby and Preston 1988, Outinen and Makelainen 2002, Twilt 1988). At ambient temperatures steel is considered to have a relatively simple stress-stain behaviour in both compression and tension with quite a well defined yielding point. Within the plastic region the steel undergoes a small region of hardening up to its ultimate stress state before softening or necking begins to occurs and, if the strains continue to increase, will finally end in rupture of the specimen. The behaviour is also temperature dependent and with temperatures as low as 200^oC the

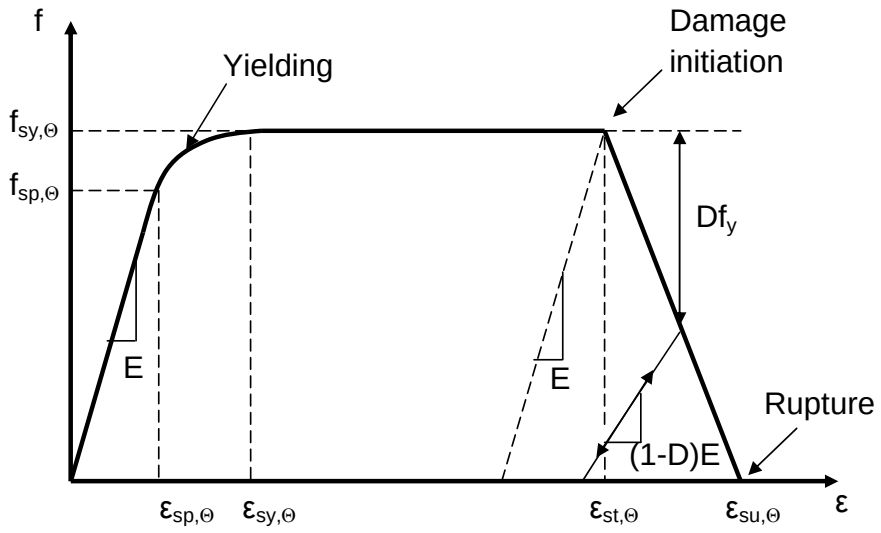

Figure 2.1: Numerical stress-strain general input for reinforcing steel in both compression and tension. The stiffness, strength and key strains are defined under ambient and increasing temperatures are defined though the equations.

strength and stiffness begins to reduce. At temperatures exceeding 400^{o}C the ultimate strength decreases rapidly and the yielding point becomes less defined. As temperatures rise further the material behaviour becomes increasingly ductile and non-linear. This behaviour of steel at elevated temperature has been well researched and documented (Cooke 1988, Elghazouli et al. 2009, Holberg and Anderberg 1993, Kirby and Preston 1988, Kodour and Dwaikat 2007, Outinen and Makelainen 2002, Twilt 1988).

This is represented in numerical models with the curve illustrated in Fig. 2.1 and the equations below.

For the elastic strain range $0 \leq \epsilon \leq \epsilon_{sy,\Theta}$ of a steel section:

$$f_\Theta = \epsilon E_{s,\Theta} \tag{2.1}$$

$$\text{Tangent Modulus} = E_{s,\Theta} \tag{2.2}$$

The transition from elastic behaviour to plastic behaviour ($\epsilon_{sp,\Theta} \leq \epsilon \leq \epsilon_{sy,\Theta}$) is

described by the equations:

$$f_{\Theta} = f_{sp,\Theta} - c + (b/a)[a^2 - (\epsilon_{sy,\Theta} - \epsilon)^2]^{0.5} \tag{2.3}$$

$$\text{Tangent Modulus} = \frac{b(\epsilon_{sy,\Theta} - \epsilon)}{a[a^2 - (\epsilon - \epsilon_{sy,\Theta})^2]^{0.5}} \tag{2.4}$$

Within the plastic range $\epsilon_{sy,\Theta} \leq \epsilon \leq \epsilon_{st,\Theta}$ it is assumed to be perfectly plastic and no hardening behaviour is included. In other words, as the strain increases there is no further increase in stress, therefore:

$$f_{\Theta} = f_{sy,\Theta} \tag{2.5}$$

$$\text{Tangent Modulus} = 0 \tag{2.6}$$

This behaviour continues until "damage" is initiated at $\epsilon_{st,\Theta}$ and softening of the material begins to occur until rupture at $\epsilon_{si,\Theta}$. This behaviour is given by:

$$f_{\Theta} = f_{sy,\Theta}.\frac{1 - (\epsilon - \epsilon_{st,\Theta}}{\epsilon_{su,\Theta} - \epsilon_{st,\Theta}} \tag{2.7}$$

Whilst the values of ($\epsilon_{st,\Theta}$) and ($\epsilon_{su,\Theta}$) are assumed through Eurocode 2 part 1-2 to be 0.15 and 0.2 respectively, these values were also calculated through an experimental investigation that is set out and explained in Appendix D. Through this investigation the values of ($\epsilon_{st,\Theta}$) and ($\epsilon_{su,\Theta}$) for the numerical modelling in this thesis were changed to 0.1 and 0.21 respectively.

If the steel is unloaded within this strain range, due a change in the atomic structure of the steel, the unloading branch does not follow a path parallel to that of the initial elastic stiffness but rather unloads with a reduced stiffness as illustrated in Fig. 2.1. The degree to which the stiffness reduces is defined as "(1-D)E" where "E" is the initial modulus of elasticity and "D" is the dimensionless damage parameter which linearly

varies from 0 at $\epsilon_{st,\Theta}$ to 1 at $\epsilon_{si,\Theta}$ (Hillerborg et al. 1976)

2.2.2 Thermal expansion

The thermal properties can be subdivided into three main categories; thermal expansion, thermal conductivity and specific heat capacity. The thermal expansion is generally defined by:

$$\alpha_\Theta = \frac{\epsilon_{th,\Theta}}{\Delta T} = \frac{\Delta l}{L \Delta T} \tag{2.8}$$

where "$\epsilon_{th,\Theta}$" is the strain resulting from the change in temperature, "ΔT" is the change in temperature, "L" is the original ambient length and "Δl" is the change in length brought about by thermal expansion.

Under increasing temperatures, steel will tend to expand and this thermal expansion has been shown to be, for the most part, linear with only a small non-linearity at approximately 700^{o}C due to a phase change in the atomic structure of the steel (change from face centered to body centered structure) (Anderberg 1988, Cooke 1988, Kodur et al. 2010). Kodur et al. presents the thermal strain behaviour measured and predicted by many experimental programs and analytical models as shown in Fig. 2.2.

Eurocode 2 part 1-2 provides a set of algebraic equations (below) to describe the thermal elongation which includes the plateau relating to the phase change. This phase change occurs at 750^{o}C and continues to 860^{o}C.

For temperature ranging from 20^{o}C (ambient) to 750^{o}C:

$$\epsilon_{th,\Theta} = -2.416e^{-4} + 1.2e^{-5}\Theta + 0.4e^{-8}\Theta^2 \tag{2.9}$$

for 750^{o}C to 860^{o}C:

$$\epsilon_{th,\Theta} = 11e^{-3} \tag{2.10}$$

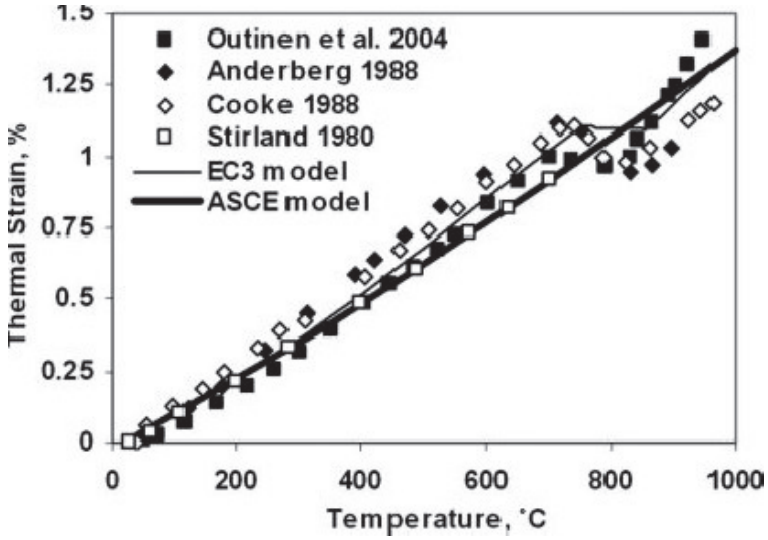

Figure 2.2: Thermal elongation of reinforcing steel under increasing temperature presented by Kodur et al. (2010). A comparison of various models.

and for 860^{o}C to 1200^{o}C

$$\epsilon_{th,\Theta} = -6.2e^{-3} + 2e^{-5} \tag{2.11}$$

2.2.3 Thermal properties

While the thermal expansion describes how the material is affected by a thermal load, the conductivity and specific heat capacity (and density) describes how a thermal load is transmitted through the material. Among construction materials, the thermal conductivity of steel is high whilst the specific heat capacity is quite low. These also vary slightly with temperature as reported upon by Kodur et al. (2010). In general, the thermal conductivity exhibits an almost linear decrease as the temperature increases (ranging from 50W/m.K to 30W/m.K) whilst there is a slight increase in the specific heat capacity with an increase in temperature (ranging from 900J/K to 1100J/K). Around 750^{o}C to 800^{o}C there is a sharp spike in the specific heat capacity resulting from the phase change as previously described.

Having these thermal properties where the conductivity is high and the specific heat capacity is low, results in the steel having the ability to transfer thermal energy quite readily. Considering the fact that reinforcing steel, for most applications, is of a small cross-section, it can be said to be "thermally thin". As a result, heat transfer is not performed across the reinforcement's cross-section but instead is assumed to have constant temperature through its cross-section. This is particularly useful for numerical modelling as the steel can then be modelled using truss elements (i.e. one dimensional elements) with only one integration point through the cross section, allowing the model to run much more efficiently. However, the heat transfer is performed along the length of the reinforcement, hence, the conductivity and specific heat capacity still have to be defined. It should be noted that, to enhance th stability of the numerical model, the sharp spike in specific heat capacity as observed in experiments around 750^{o}C to 800^{o}C has been removed.

2.3 Concrete

The material behaviour of concrete at ambient temperatures and under normal loading conditions is usually considered, for design purposes, to be relatively simple. However, it can become much more complex when subjected to extreme conditions such as those that occur during earthquakes, impacts, blasts or fires. The effects brought about by these events can cause loss of strength and stiffness and excessive stresses and strains to develop that can lead to cracking and crushing of the concrete. In addition to this, increasing temperatures can also cause geometrical changes such as spalling. All these factors can cause excessive and detrimental deflections to develop and an overall reduction in load bearing capacity.

2.3.1 Stress-strain relationship

Unlike steel, the stress-strain behaviour of concrete is not the same in both compression and tension. There are two significant differences which can be highlighted. Firstly the yield strength in compression is considerably higher than that of the strength in tension, usually assumed to be approximately ten to fifteen times higher in a normal concrete mix. The second difference is that concrete in compression provides a small amount of ductility whereas in tension concrete is extremely brittle. It is therefore rare that pure concrete is used in an application and it is more likely that the concrete will be reinforced with an internal steel cage.

Under normal structural situations it is common that only small deflections occur within a reinforced concrete structure, hence softening behaviour is generally ignored. Once again however, this post yielding behaviour can not be ignored for scenarios such as earthquakes, impacts and blasts where displacements and strains have the potential to exceed the maximum stress state, leading to crushing in compression and cracking in tension.

Furthermore, although reinforced concrete has traditionally been taken to be a fairly inert material in the presence of fire, in reality, the behaviour of concrete in response

to fire can be very complex with loss of strength and stiffness, differential thermal expansions, moisture migration and increased pore pressure all occurring simultaneously.

2.3.1.1 Compressive behaviour

Concrete is used in structural applications for its high compressive strength to density ratio. However, large forces and displacements placed upon a concrete member or specimen causes microcracks to form within the concrete matrix. The formation of these microcracks is represented macroscopically as softening behaviour (Lee and Fenves 1998a,b) (i.e. the load carrying capacity of concrete rapidly reduces). This softening behaviour was illustrated by Karsan and Jirsa (1969) and Lam (1980) in which a series of experimental compressive loading tests were performed on cylinders of plain concrete (see Fig. 2.3). The data is normalised and placed on the same graph for comparative purposes. However, as highlighted by Legeron et al. (2005) the compressive strain that a concrete specimen will accommodate can be much greater when confined. This confinement, for most structural applications, is provided by the steel reinforcement. This results in the concrete cover having a different material behaviour to the concrete core.

Crushing of concrete not only reduces the load carrying capacity but also has the ability to decrease the elastic stiffness of the material. Karsan and Jirsa (1969) and Lam (1980) also presented experimental data on cyclic compressive loading of plain concrete which concluded that as the compressive strains exceeded the maximum stress state the elastic stiffness began to reduce quite rapidly. This has been incorporated into the numerical simulation as illustrated in Fig. 2.4 where in the post yielding behaviour, any unloading of the concrete does not result in an unloading path parallel to the initial elastic stiffness but rather follows an unloading path with a reduced stiffness. Some research has been carried out on obtaining "damage" values for this behaviour (Cosenza and Manfredi 2000, Kappos 1997, Lee and Fenves 1998b). However, this can be difficult as they will vary slightly from specimen to specimen depending on the mix design, loading, boundary conditions and geometrical setup.

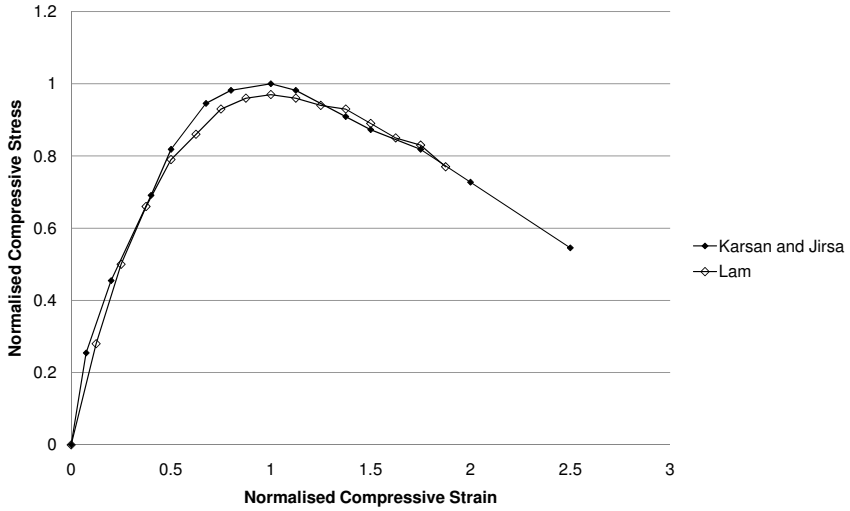

Figure 2.3: Stress-strain behaviour of concrete in compression at ambient temperature. Results obtained from (Karsan and Jirsa 1969, Lam 1980) and clearly illustrates the softening behaviour after the ultimate strength.

Similar to steel, concrete undergoes a reduction in strength and stiffness when subjected to increasing temperatures Holberg and Anderberg (1993), Kodour and Dwaikat (2007), Long-yuan and Purkiss (2005). These reductions are a result of the differential thermal expansions of the cement paste and aggregate causing micro cracks to form, dehydration of the concrete matrix and chemical decomposition.

Temperatures increases above 100^oC cause the free water within the pore of the concrete to begin to evaporate. This evaporated free water can become trapped within the concrete resulting in micro cracks being formed and the pore water pressure to increase. The implications of this pore pressure is discussed further in Section 2.3.3.1. As temperatures increase above 400^oC, the cement hydration products start to decay causing a reduction of the chemically bonded water within the cement paste itself (Biolzi et al. 2008), which in turn results in a decreased bulk density and an increased permeability. It is this increase in permeability that gives rise to the reduced strength and stiffness.

Simulation of concrete under extreme loads requires a complex and robust modelling framework. To achieve this, a concrete damaged plasticity (CDP) material framework

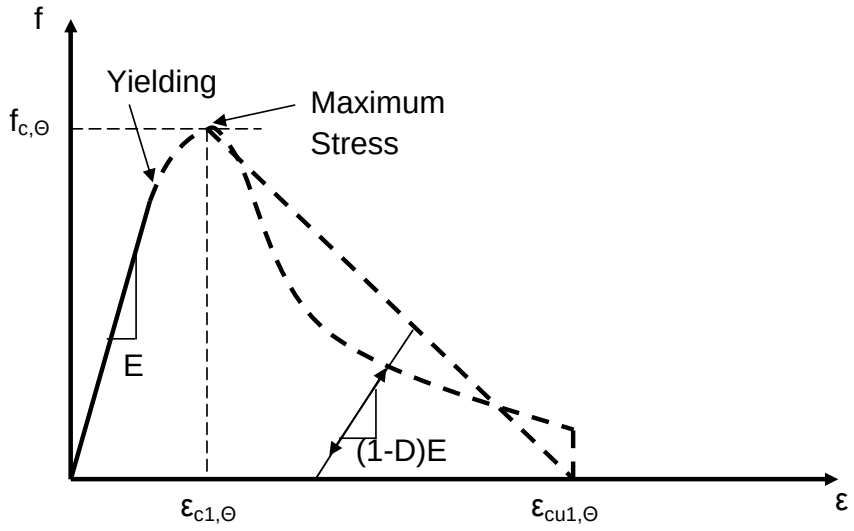

Figure 2.4: Numerical stress-strain general input for concrete in compression. The stiffness, strength and key strains are defined under ambient and increasing temperatures are listed in Appendix I.

is adopted (Lee and Fenves 1998a,b). This framework allows for characteristics such as different compressive and tensile properties to be defined with independent hardening branches, softening branches and a variable change in strength and stiffness depending on the temperatures and stress states.

Similarly to steel, the material properties of concrete were based on the Eurocode representation. The compressive behaviour as illustrated in Fig. 2.4 defines the stress-strain relationship in compression. The behaviour up to the maximum compressive stress is defined in Eurocode 2 Part 1-2 as:

$$f_\Theta = \frac{3\epsilon f_{c,\Theta}}{\epsilon_{c1,\Theta}(2 + (\frac{\epsilon}{\epsilon_{c1,\Theta}})^3)} \tag{2.12}$$

After the maximum stress state is achieved, the concrete softens which is numerically modelled by defining a softening branch in the stress-strain data which for the model used in this thesis is defined as a linear reduction. A linear reduction was chosen to

keep the material behaviour as simple as possible. However, to avoid numerical issues and singularity points, the minimum stress defined in the softening branch does not reduce to zero but to a very small finite value (i.e. $1/100^{th}$ of the initial yield stress).

2.3.1.2 Tensile behaviour

Design of reinforced concrete assumes that the concrete has no tensile strength and that all tensile loading is transfered to the steel reinforcement. However, in reality the concrete, although brittle, will possess some tensile strength as illustrated in Fig. 2.5.

As stated, the main issue with a pure concrete specimen under tension is that it is brittle, therefore once a crack occurs the tensile strength across that crack rapidly reduces to zero, the area of specimen being subjected to that tensile force reduces and hence propagation of the crack through the specimen accelerates. However, this reduction of tensile strength is not instantaneous as the interaction of the cement paste with the aggregate and the aggregate interlocking will help to partially retain some tensile strength as a crack opens (see Fig. 2.5). This behaviour is know as tension softening and can be quite difficult to numerically model.

For instance, consider a unit piece of pure concrete, with three strain gauges (A, B and C), that undergoes uniaxial tension (Figure 2.6) (Pankaj 1990). As the load is applied, the stress and strain increase in a linear fashion up to the point where the concrete develops a localised micro crack that will propagate through the width of the specimen. At this point, if the crack intersects gauge 'A' and 'C', three very different behaviours will arise from the same sample when looking at the different gauges. Measurements from gauge 'A' displays a clear softening branch whereas the portion of concrete measured by gauge 'B' will begin to relax and hence will display an unloading behaviour. The overall stress-strain relationship represented by gauge 'C' will be an average of gauges 'A' and 'B'.

This simple example shows just how localised the phenomenon of tensile cracking is and how defining material properties in terms of a stress-strain relationship may be erroneous due to the dependency on the length of the gauge. To address this problem,

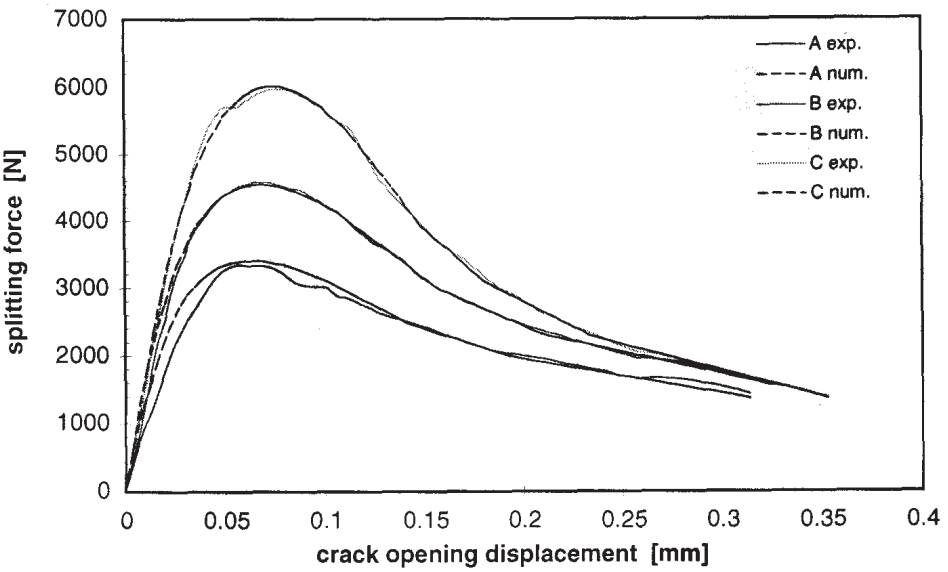

Figure 2.5: Results obtained by a wedge splitting test for three types of concrete with the addition of a numerical representation (Wittmann 2002)

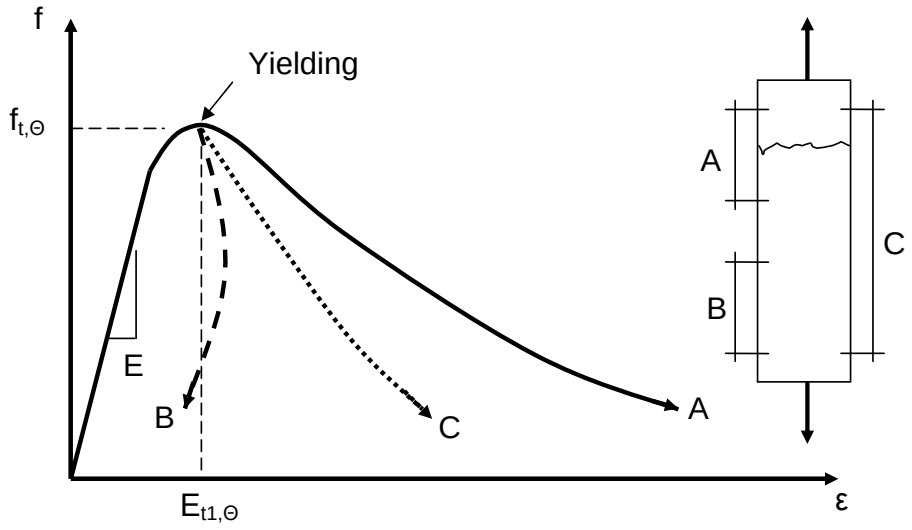

Figure 2.6: Stress-strain behaviour of concrete in tension ambient temperatures illustrating localisation issues; redrawn from Pankaj (1990).

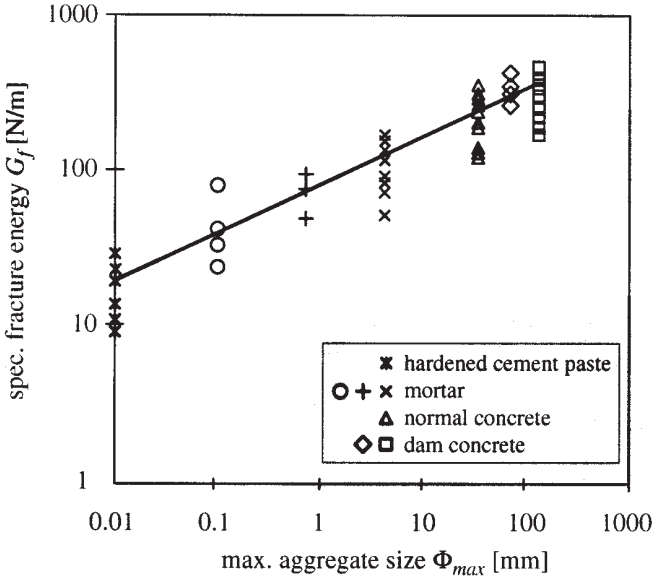

Figure 2.7: A plot illustrating how the fracture energy (G_f) of cement-based materials varies as a function of aggregate size. Illustrated from Wittmann (2002).

the tensile behaviour can be modelled in terms of fracture energy G_f. Fracture energy is defined as "the energy required to create a unit area of fracture surface (Guo and Gilbert 2000) and is affected by the geometry of the specimen, the specimen's material properties and the applied stress field (Harder 1992).

Trunk and Wittmann(2001) and Wittmann (2002) investigated how the aggregate sizing affected the fracture energy of a concrete specimen, Fig. 2.7. It was found to vary with reasonable linearity when drawn on a logarithmic scale with the lowest fracture energy being measured on pure hardened cement paste (i.e. aggregate dimensions of 0.01mm) rising to a fracture energy of the order of $1x10^2$N/m with aggregate sizing of 120mm. The relationship between the aggregate sizing and fracture energy shown in Fig. 2.7 can be defined by equation G_f=a.ϕ^n where the parameters a=80.6 and n=0.32.

Further to this, the geometry of the specimen and its effect on the fracture energy has also undergone much investigation (Duan et al. 2003, Guo and Gilbert 2000, Trunk and Wittmann 2001). Common structural elements typically have dimensions

of the order of ten times greater than that of the aggregate dimensions. Therefore, in these cases (as also implemented in design) the heterogeneity of the material can be neglected. However, for common structural elements it has been shown that the fracture energy is still a function of the dimensions(Trunk and Wittmann 2001). X.H. Guo and R.I. Gilbert (2000) carried out a series of experimental investigations examining in detail how the fracture energy can be affected by the cross-sectional dimensions. The dimensions of the elements used were of the order of those found in common structural elements with depths and widths ranging from 150mm to 600mm and 100mm to 600mm respectively. The results obtained showed that the fracture energy varied from 120N/m to as high as 443N/m, therefore clearly showing that the cross-sectional dimensions of a structural member can significantly affect the fracture energy.

Throughout the numerical analyses of this thesis a fracture energy of 100N/m was used. This value was obtained from ambient text that were performed as part of the full scale tests as detailed in Chapter 5. As no data was available for high temperatures, the fracture energy was assumed to remain constant for all temperatures.

Although the fracture energy method reduces the mesh sensitivity issue, it also reduces the stress state to zero at the crack which, although may be strictly correct may cause numerical problems due to singularity issues. To overcome this, instead of specifying a fracture energy in a numerical model, the fracture energy is used along with defining a characteristic element length to specify a stress-strain curve that defines the softening branch. Once again, instead of reducing to zero, it reduces to a very small value (i.e. $1/100^{th}$ of the failure stress).

The tensile stress-strain relationship is assumed to be linear elastic up to the initiation of yielding. The strength of concrete in tension is relatively small and at ambient temperature is usually assumed to be approximately $1/10^{th}$ that of the compressive strength. This tensile behaviour is also temperature dependent where the maximum strength and stiffness of the material decreases as the temperature increases. The elastic stiffness of the concrete is assumed to be the same in both compression and tension, therefore the tensile stiffness reduces with increasing temperature with the same rela-

tionship as in compression. The maximum strength in tension also reduces where the reduction factor is defined as:

$$f_{ck,t\Theta} = k_{c,t\Theta} f_{ck,t20} \tag{2.13}$$

where $k_{c,t\Theta}$ is the reduction factor that varies with temperature as defined in Eurocode 2 Part 1-2 (2004).

The use of concrete in structural applications is reinforced with steel in order for the member to withstand the tensile forces and flexural moments. Therefore, further to the work on the tensile behaviour previously discussed, the tension stiffening behaviour and fracture energy of the concrete needs to be adjusted once again as described in Feenstra and de Borst (1995). In this case, the tension stiffening behaviour is denoted as the ability of the concrete to gradually redistribute load to the steel following the onset of cracking.

Fig. 2.8(a) shows the stress-strain relationship of the concrete in tension, illustrating its brittle nature. However, the interaction between the concrete and the steel increases the ductility of the concrete. As a result the concrete will retain some of its strength up to the yielding point of the steel. This is accommodated in the material properties by defining the post yielding tensile behaviour of the concrete as shown in Fig. 2.8(b). When combined with the stress-strain relationship of steel the combined stress-strain relationship is as illustrated in Fig. 2.8(c), where the tension stiffening is clearly shown and the concrete retains some tensile strength up to the point whereby yielding of the steel reinforcement occurs.

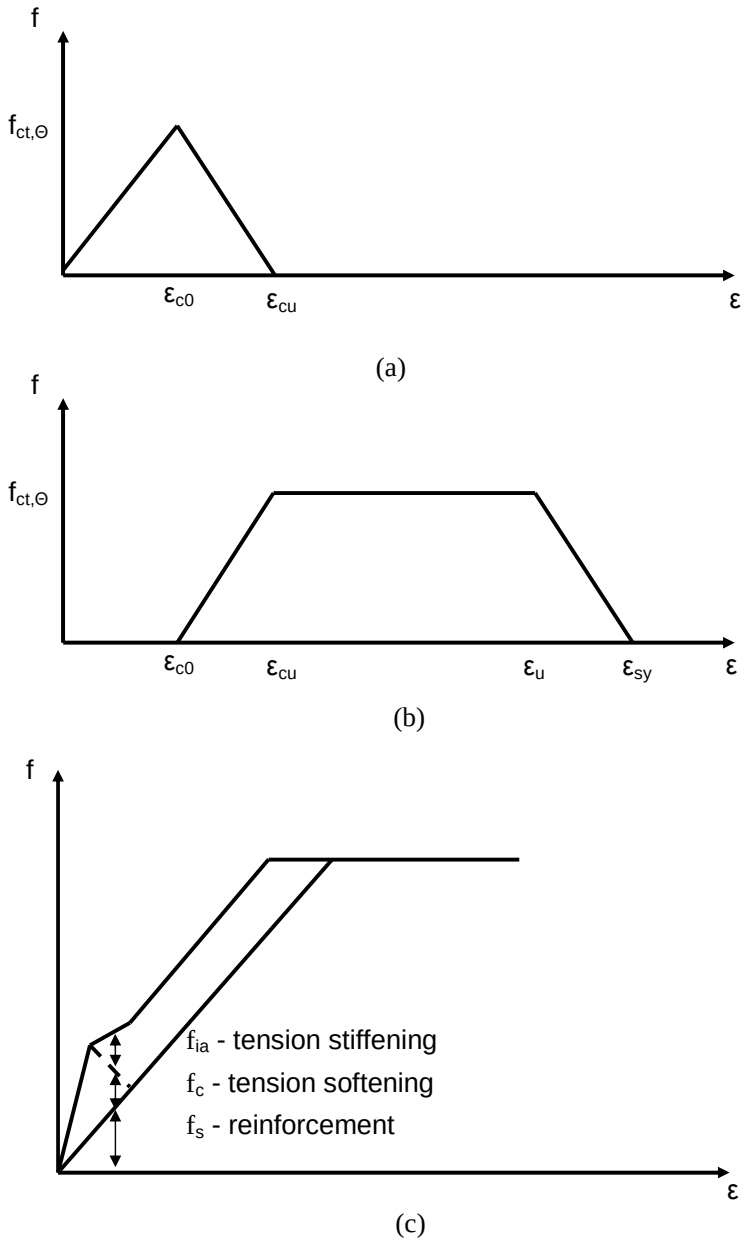

Figure 2.8: Idealised representation of constitutive model for reinforced concrete in tension. a) The true tension stress-strain relationship of pure concrete with softening behaviour, b) The numerical input for the concrete component incorporating the interaction between the concrete and the steel reinforcement and c) Overall tension stress-strain relationship for reinforced concrete

2.3.2 Thermal expansion

The thermal expansion of concrete is more complex that that of steel due to the differential expansions of the constituent ingredients and depends on factors such as stress levels, aggregate to cement ratio and the heating rate (Naus 2006). It is suggested by Neville (Neville 1996) that typically the coefficient of expansion "α" ranges from 5.9x10^{-6} /^{o}C to 13.1x10^{-6} /^{o}C. This coefficient of thermal expansion also is temperature dependent and leads to a thermal elongation of concrete that is non-linear as discussed in Lie and Kodur (1995).

Unlike steel, the the thermal expansion of concrete is also dependent on the stress levels applied (Khoury 2006, Petkovski 2010). If the stress reaches levels greater than 45% of the uniaxial compressive strength it has been observed that contraction occurs when a thermal load is applied (Law 2010, Petkovski and Crouch 2008).

Eurocode 2 Part 1-2 provides a simplified relationship to describe the thermal elongation of siliceous concretes which are shown through the equations below and Fig. 2.9.

for temperatures from 20^oC to 700^oC

$$\epsilon_{c,\Theta} = -1.8e^{-4} + 9e^{-6}\Theta + 2.3e^{-11}\Theta^3 \tag{2.14}$$

for temperatures from 700^oC to 1200^oC

$$\epsilon_{c,\Theta} = 14e^{-3} \tag{2.15}$$

2.3.3 Thermal properties

Once again, the thermal propagation through a material is defined by k/ρc_p. The low conductivity and high specific heat capacity of concrete make it ideal for use as a thermal insulator. The thermal conductivity and specific heat capacity of concrete define the rate of heat transfer through a section and relies heavily on both the moisture and

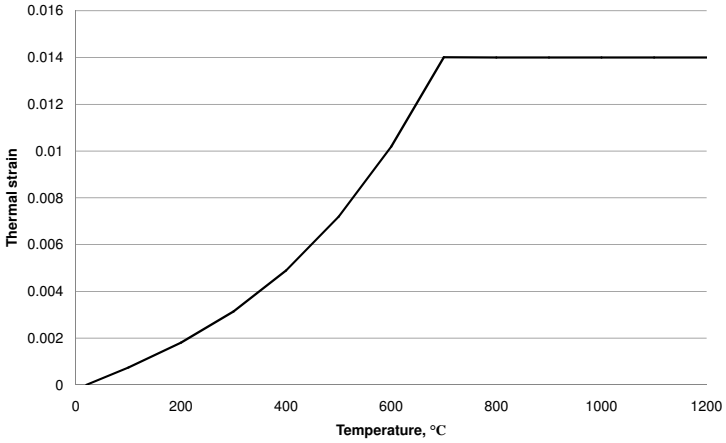

Figure 2.9: Numerical representation of the thermal expansion of siliceous concrete under increasing temperatures.

the type of concrete. For concrete, these thermal properties have been well documented (Eurocode 2004) and researched (Bratina et al. 2005, Holberg and Anderberg 1993, Kim et al. 2003). An in depth experimental study by Kim et al. (2010) concluded that the main factors affecting the conductivity was the aggregate volume fraction and moisture of the specimen. Typical values for conductivity and specific heat capacity of concrete range from 1.95W/m.K and 900J/K at ambient to 0.72W/m.K and 1100J/K at high temperatures (i.e. 800^oC) respectively and generally behaves linearly in between independent of moisture content. It should be noted that experimental data illustrates a shape spike in the specific heat capacity around 100^oC due to the state change (liquid to vapour) of the moisture within the concrete.

However, most of this data relates to concrete in its undamaged state. Under extreme conditions the concrete can become damaged in multiple ways. For instance, if there is a loss of concrete cover, possibly due to crushing, the designed fire resistance provided will become significantly reduced within the region of cover loss. This type of damage can occur prior to a thermal load or during the thermal load as described later in this chapter. On the other hand, reinforced concrete can become significantly cracked when subjected to high tensile loads. When the concrete cover becomes damaged in such a way that there is considerable tensile cracking (i.e. cracks of the order of $1x10^1$mm), the rate of thermal propagation through the cracks regions may be sig-

nificantly different to the thermal propagation through the solid concrete of an intact section and could lead to earlier structural failure during a fire.

Tensile cracking of the concrete cover is an extremely localised geometrical phenomenon that has the potential to alter the thermal propagation through a section within those localised regions. Therefore, as tensile cracking is a structural phenomenon, it will not truly alter a materials thermal properties, yet it may still have an effect that can be described, for the purposes of numerical modelling, in terms of a local change in material properties.

Kong et al (2007), and Beeby and Scott (2005) studied the behaviour of average tensile crack width with respect to the tensile stress within reinforcement. However, the stresses and strains considered all fell into the elastic region of the reinforcement which corresponds to very small crack widths (of the order of $1x10^{-1}$mm). It would be inappropriate to extrapolate this information to situations where the reinforced concrete members are severely damaged and include a high degree of plasticity, as may occur in extreme events, such as earthquake. In such cases, local yielding of the reinforcement may cause crack widths of the order of $1x10^{1}$mm or greater.

Vejmelkov et al's (2008) study on the effects of cracks on the hygric and thermal characteristics of concrete and obtained data suggesting the conductivity of cracked concrete decreased due to the increased porosity of the material and only increased with an increase in moisture content. They suggested that the air within cracks acts as an insulator and hence hinders the propagation of heat through the structure. A significant limitation of this work is the fact that the crack dimensions were not reported so the results cannot be combined with the work by Kong et al (2007) to find a relationship between crack width and conductivity. In addition, plain, unreinforced concrete was used for this investigation hence application of the results to a real world structure would be difficult.

Contrary to Vejmelkov et al(Vejmelkov et al. 2008), Shi et al's(Shi et al. 2004) study yielded the opposite conclusion where the tensile cracking had a profound effect on the fire resistance of the section. The aim was to compare experimentally ascertained re-

sults to a theoretical method for determining structural failure of sections with differing concrete covers in terms of gas temperatures. The disagreement between the theoretical and experimental ultimate temperatures was attributed to flexural cracking affecting the thermal distribution and causing local heating of the reinforcement. This effect was not included in the theoretical method. However, for the experiments that this was concluded neither the thermal profile through the section nor crack widths were measured. Therefore, the conclusion that the tensile cracking has a profound effect can only be acknowledged as an assumption based on an indirect method of measurement (i.e. the disagreement between the theoretical and experimental ultimate temperatures).

Thus, work aimed at determining the thermal properties of crack-damaged reinforced concrete is very limited and conceptual. The work that has been undertaken has either been with unreinforced concrete or within the elastic range of the reinforcement, and crack width has not been directly measured. The inclusion of reinforcement in the concrete during an experiment that considers cracking is vital because the reinforcement drastically alters the cracking pattern and crack propagation though a section. During extreme events it is unreasonable to assume that the reinforcement remains within its elastic range as these extreme events will cause larger cracks to form in the concrete. The larger the cracks within the concrete cover the more influential the buoyancy and radiative effects within these cracks may become. The air within the cracks may no longer act as an insulator as Vejmelkov et al(Vejmelkov et al. 2008) suggest but may effectively allow heat to instantaneously penetrate the concrete to the reinforcement level as suggested by Shi et al(Shi et al. 2004).

Similar to steel, these thermal properties vary with temperature and moisture content but for the purposes of the numerical model, it is assumed that the concrete is "dry", therefore, it should be noted that the spike in specific heat capacity at the approximate temperature of 100^oC is not present. The geometric effects such as loss of concrete cover due to a build up of excessive plastic strains can also be simulated by changing the material properties as explained and described in Chapter 4.

2.3.3.1 Spalling

In addition and as a result of thermal expansion, thermal strains and increasing pore water pressure reinforced concrete members are also susceptible to spalling. Spalling is the process of the disintegration and loss of portions of concrete from the main body. Due to the insulative properties of concrete, this process is considered to be more of an issue when a concrete member is placed under a thermal load. A thermal load applied to a concrete specimen can cause sharp thermal gradients to form within the concrete and the migration and evaporation of free water (water that is not chemically bonded to the cement) through the concrete.

The formation of the sharp thermal gradients within a concrete specimen can result in high differential thermal strains throughout the specimen depth which can exceed the tensile strength of the concrete leading to spalling of the cover. This mechanism of spalling depends strongly on the rate of thermal loading and the composition of the specimen. The higher the thermal loading rate, the sharper are the thermal gradients that form and as a result the potential for spalling increases (Ali 2002, Hertz 2003, Khoury 2000).

In addition to the thermal stresses that develop, it has been shown that the moisture content and moisture migration through the concrete specimen has a profound effect on the spalling (most notably explosive spalling) of a concrete specimen (Buchanan 2001, Khoury 2000, van der Heijden et al. 2007). As the temperature of the concrete surface increases, the free water within the concrete matrix is forced to migrate deeper into the section. This migration of the free moisture results in an increased pore pressure within the specimen, which if not released can increase to exceed the tensile strength of the concrete, leading to an increased rate of thermal spalling (Hertz 2003).

Spalling of a reinforced concrete specimen is a significant concern when dealing with thermal loadings. As described earlier in the chapter, the fire resistance design mainly relies upon the concrete cover remaining intact and providing an insulating barrier to the steel reinforcement. The action of spalling directly compromises this design by providing mechanisms for removal of the concrete cover.

2.4 Combined steel and concrete behaviour

As previously stated, concrete is inherently weak and brittle in tension and as a result steel reinforcement is introduced to increase the tensile strength of a member. The effectiveness of this is partially dependent on the interaction between the concrete and the steel. Under normal ambient loading conditions this interaction is assumed to be be "perfect". In other words, the surface interaction between the concrete and the steel is completely bonded and exhibits no slip. However, when a member is subjected to large stresses and strains this interaction between the concrete and steel reinforcement may not be "perfect" and consequently may be subject to failure or partial failure. This phenomenon is known as "bond-slip".

Research into the cyclic response of reinforced concrete columns and structures (D'Ambrisi and Filippou 1999, Spacone et al. 1992, Wan et al. 2001) have alluded to the realisation that shear cracking of the concrete around the reinforcement and bond-slip at the steel concrete interface leads to a response known as "pinching", illustrated in Fig. 2.10. Shear cracking and bond-slip within a reinforced concrete member subjected to pure tension has also been experimentally investigated by Beeby and Scott (2005). Through this investigation it was concluded that the most significant failure mechanism between the steel reinforcement and the concrete arose from internal shear cracking of the concrete rather than bond failure.

Furthermore, this bond strength can also become significantly affected by increases in temperature. Tanyildizi et al (2008) performed an in depth experimental study into how high temperatures affected the bond strength between concrete and reinforcing steel. It was shown that the bond strength reduced by 20 to 25% at 400^o and as much as 76% at 800^o. The bond slip at high temperatures can be, in part, attribted to the differential expansions of the cement paste, aggregate and steel as previously discussed in the chapter. This reduction of bond strength reduces the stress transfer between the concrete and steel, which in combination with the reduction of the material properties, results in a significantly reduced load carrying capacity (Haddad et al. 2008).

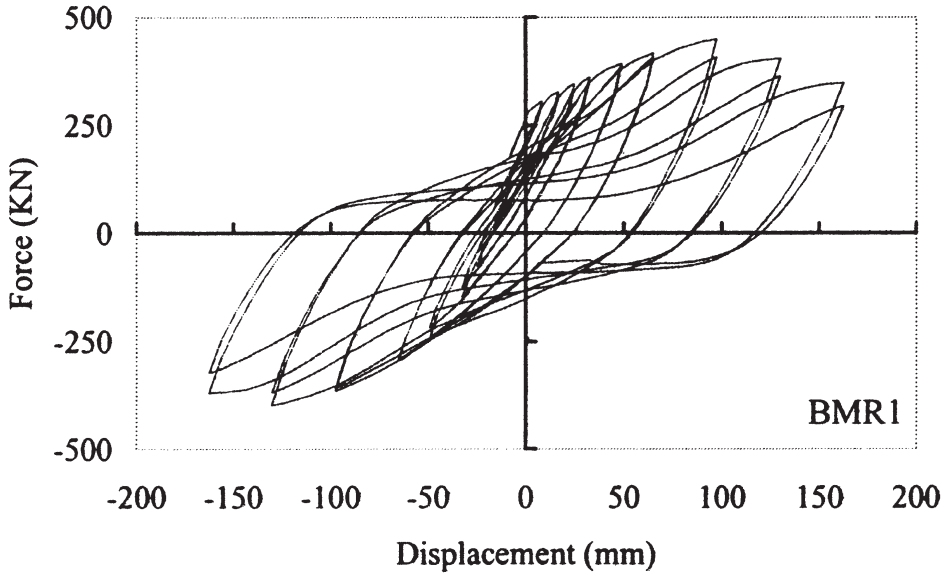

Figure 2.10: Plot showing the load deflection relationship of a reinforced column subjected to a horizontal cyclic load (Wan et al. 2001). Particular reference is to be made to the "pinching" phenomenon illustrated.

2.5 Conclusions

There has been much research undertaken into the material properties of both steel and concrete subjected to excessive tensile and compressive loading and a large variety of loading types. It has been shown that the simplistic stress-strain relationship generally associated with steel under normal ambient loading conditions becomes much more complex as the strains increase beyond the yielding of the material, ultimately resulting in rupture (in tension) and the complete loss of load carrying capacity.

Concrete under excessive loading also is much more complex that its design characteristics. Concrete in compression, like steel, undergoes a region of hardening followed by a region of softening behaviour up the the point where crushing occurs and the reduction of the load carrying capacity. However, concrete in tension has little or no hardening behaviour as it is extremely brittle, although work performed by Wittmann (2001), in particular, has shown that concrete in tension does exhibit softening behaviour after its initial yielding. This is in contrary to design where it is assumed that concrete has no tensile strength.

2. FACTORS AFFECTING MATERIAL AND STRUCTURAL BEHAVIOUR AND HOW THEY CAN BE MODELLED

The principles of the numerical model used to simulate the mechanical and thermal behaviour of a reinforced concrete structure subjected to extreme loading scenarios was presented. It has explained and described the main issues faced, such as post yielding behaviour, softening and phase changes within the materials which can lead to numerical instabilities. It has also covered the issue of mesh sensitivity when dealing with brittle materials with the addition of presenting the procedures undertaken to minimise or eliminate the impact of these issues.

While the research presented have been useful in furthering the knowledge of the structural behaviour of reinforced concrete structures subjected to large stresses and strains, it is clearly necessary to develop a better understanding of how the localised effects such as tensile cracking and compressive crushing contribute to the global thermo-mechanical behaviour of the structure.

If considering the scenario of a mechanically extreme event occurring prior to the outbreak of a fire, the resistance to this subsequent thermal loading can be significantly reduced due to sustained initial damages and as a result can lead to a reduced time to failure. It is clear that there is a requirement to further understand how geometrical effects and non-linearities affect the thermal performance of concrete members and structures.

Chapter 3

Thermal propagation through tensile cracks in reinforced concrete

3.1 Introduction

The fire resistance of concrete structures depends strongly on the concrete cover provided to the reinforcing steel because it acts as a form of insulation, keeping the steel relatively cool. In several loading scenarios, such as earthquake, impact or blast, the cover may become damaged. The effectiveness of the cover in providing fire resistance may then be significantly reduced leading to the situation where a subsequent fire will have a more severe effect. Damage to concrete cover can be in the form of tensile cracking, crushing or complete removal. Clearly if the cover is removed then there is no longer any effective insulation to the steel. However, it is less clear what effect tensile cracking has on the insulating properties of the cover.

The rate of heat transfer through a section is governed by the conductivity, specific heat capacity and density of a material. For concrete, these thermal properties have been well documented Eurocode (2004) and researched (Bratina et al. 2005, Holberg and Anderberg 1993, Kim et al. 2003). However, most of this data relates to concrete in its undamaged state. When the concrete cover becomes damaged in such a way that there is considerable tensile cracking (i.e. cracks of the order of $1x10^{1}$mm), the rate of

thermal propagation through the cracks may be significantly different to the thermal propagation through the solid concrete of an intact section and could lead to earlier structural failure during a fire.

Tensile cracking of the concrete cover is an extremely localised geometrical phenomenon that has the potential to alter the thermal propagation through a section within those localised regions. Therefore, tensile cracking will not truly alter the materials thermal properties, yet it may still have an effect that can be described, for the purposes of numerical modelling, in terms of a local change in material properties.

The experiments detailed in this paper are designed to establish whether tensile cracking alters the thermal propagation within the localised region of the cracks to a degree whereby the change cannot be neglected in the analyses of structures subjected to fire. There are three hypotheses considered:

Hypothesis I

Tensile cracking increases the thermal propagation through the concrete so that heat transfer is more rapid, hence the reinforcement layers will experience high temperatures more quickly than in an intact section. This would cause the steel to be subjected to localised heating and elongation which could lead to failure of a member or structure more quickly than an undamaged structure.

Hypothesis II

Tensile cracking decreases the thermal propagation through the concrete so that heat transfer is less rapid, hence the reinforcement layers will experience high temperatures later in a fire than an intact section. This could cause structures to perform better than an undamaged structure.

Hypothesis III

Tensile cracking does not significantly affect the thermal propagation through the concrete. The reinforcement layers will experience similar temperatures in a similar time

to those experienced by an intact section. This would mean that the effects of tensile cracking on thermal propagation through a section are negligible and do not need to be accounted for in analyses or design.

3.2 Experimental Methods and Materials

3.2.1 Apparatus

Concrete beams were loaded in "four point bending" to deflection levels that caused damage in the form of cracking of various degrees of severity (detailed below) on their tensile faces. The tensile faces were then heated and the thermal profiles produced within the beams recorded by embedded thermocouples. The method used to place these thermocouples can be found in Appendix C. Comparison of the thermal profiles for different levels of damage allowed it to be determined whether tensile cracking significantly altered the thermal propagation. These arrangements are shown in Fig. 3.1 to Fig. 3.4 and the individual test beams are detailed in Table 3.1.

The beams were doubly reinforced with a span of 870mm and cross-sectional dimensions of 90x160mm. Concrete cover was 20mm on all sides, with the exception of the tensile face which had a cover of 40mm. Increased cover on the tensile face was designed to induce larger tensile crack widths which would be representative of beams of larger, more realistic dimensions.

The beams were loaded vertically upwards in four point bending as shown in Fig. 3.1, either to failure (i.e. beams 1 and 2) or to the required deflection depending on the stage of the experiment as detailed in Table 3.5. This arrangement allowed for a suitable length of the beam to be placed in pure bending, which in turn ensured a uniform distribution of tension cracks. After the required deflection had been obtained by mechanical loading, heat was applied to the tension face of the beams from above via a propane gas fuelled radiant panel. The radiant panel was adjusted to provide a constant thermal load of the 35kW/m^2 at the tensile face for one hour, after which it was switched off and the apparatus allowed to cool naturally. During the heating and

3. THERMAL PROPAGATION THROUGH TENSILE CRACKS IN REINFORCED CONCRETE

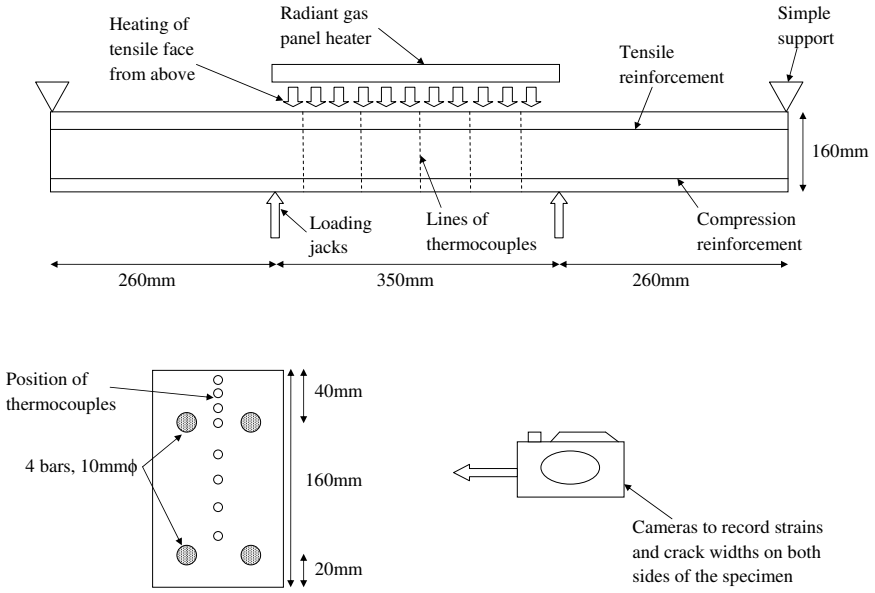

Figure 3.1: Experimental apparatus set-up for the investigation into the thermal propagation through tensile cracks in reinforced concrete. Showing a side-view of a beam, a typical section and general locations of the thermocouples.

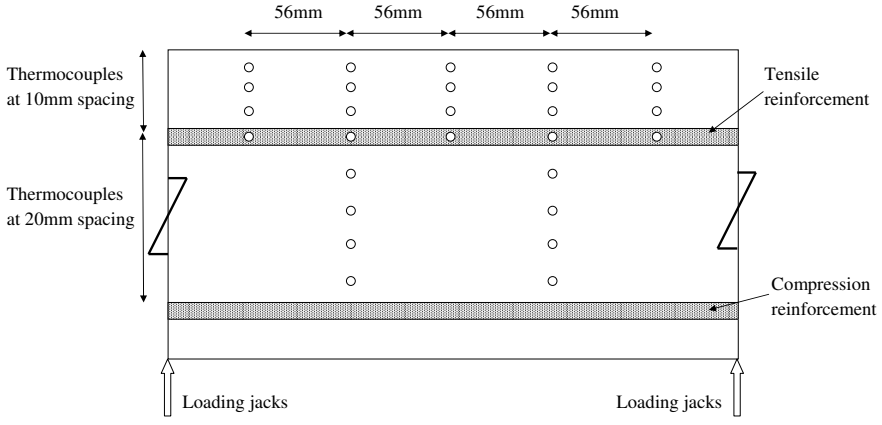

Figure 3.2: Thermocouple locations embedded within the beams at the mid-span for the investigation into the thermal propagation through tensile cracks in reinforced concrete.

Table 3.1: Load cases to be performed for the investigation into the thermal propagation through tensile cracks in reinforced concrete. The minor and major damge limits are defined later in the chapter.

Beam	Thermo-couples	Loading Phase	Heating Phase	Description
1	-	√	-	Loaded incrementally to failure to determine crack widths and distribution as a function of load.
2	-	√	-	Repeat of beam one.
3	√	-	√	Thermal loading only to determine the rate of thermal propagation through an undamaged section.
4	√	-	√	Repeat of beam three.
5	√	√	√	Loaded to induce minor damage and subsequently heated to determine the effect on thermal propagation.
6	√	√	√	Repeat of beam five.
7	√	√	√	Loaded to induce major damage and subsequently heated to determine the effect on thermal propagation.
8	√	√	√	Repeat of beam seven.

cooling phases of the experiment the load applied to the beam was controlled constantly to maintain the desired deflection and hence maintain the required crack width. Fireboard insulation was used to ensure that only the tensile face was heated and 1-D heat transfer was produced as well as to ensure that the remainder of the apparatus (and ends of the beam) was not heated. The experiment was performed with loading from below to ensure that if the beam failed it did not damage the radiant panel.

Loads were recorded using load cells placed under the loading jacks and deflections from gauges at mid-span and other key locations, such as under the supports to monitor for settlement. The load and deflection data was recorded in real time at 5s intervals. High resolution digital photographs were taken of both sides of the beam within the constant moment region between the loading points, and these were post-processed to determine the crack width development in the beam. The digital image correlation (DIC) method used is discussed in Appendix E.

Temperatures in the beams were recorded using a large number of thermocouples,

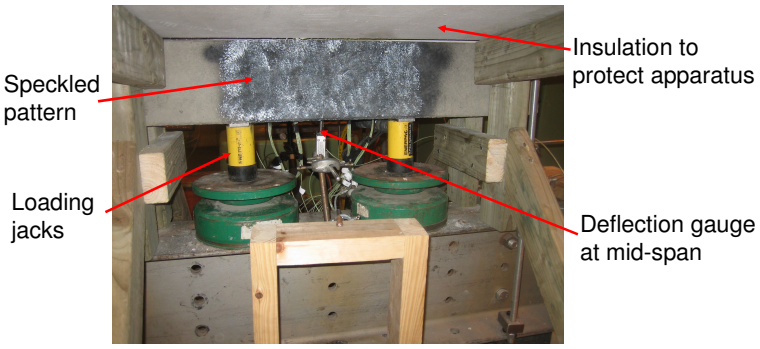

Figure 3.3: Photo: The loading set-up used to produce the tensile cracking of the tensile surface. The jacks have a maximum output capacity of 10 tonnes each. The speckled area (black and white pattern) used for displacement measurements is also shown as well as the deflection meter at the mid-span of the beam.

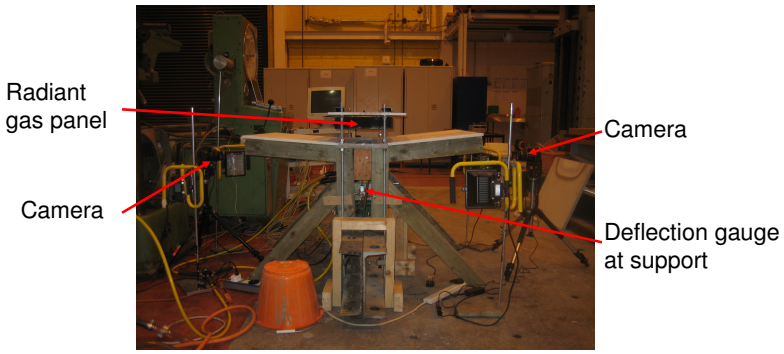

Figure 3.4: Photo: Overall set-up for the thermal testing of the tensile cracked beams (before testing commenced), showing the digital image correlation method set-up, support deflection gauges, radiant heat panel and insulation set-up.

the locations of which are shown in Fig. 3.1 Fig. 3.2. K-Type thermocouples were used throughout which have a tolerance of $\pm 1.5\,^{\circ}\mathrm{C}$. As the investigation aimed to determine if tensile cracking of the concrete cover affected the thermal propagation through the cracked region, the majority of the thermocouples were placed within the concrete cover on the tensile side of the beam. All these details and other aspects of the experiments are shown in Fig. 3.1 to Fig. 3.4.

To ensure that the thermocouples would not be displaced by settling concrete they were placed in the concrete beams after casting but while the concrete was still wet.

This was quite a crude process and it was difficult to be certain of their locations during the tests. Consequently, post-experimental destructive testing of the specimens was used to determine the actual locations of the thermocouples. In general this was found to be better than expected, nonetheless, when calculating the average temperature at a specified depth within the beam (discussed later) only those thermocouples within a tolerance of ±1mm of the stated depth are included in the calculations and graphical representations. See Fig. 3.6 to Fig. 3.12.

Comparison of cracking patterns in purely mechanical load beams (i.e. load beams 1 and 2 in Table 3.1), and tests where embedded thermocouples were used, showed that the presence of thermocouples did not affect the tensile cracking pattern. As tensile cracking is an extremely localised phenomenon, cracks would have to be at or close to the thermocouple trees to ensure any effect on thermal propagation through the crack was recorded. For this reason, when conducting the experimental repeats on the damaged specimens (beams 2, 4, 6 and 8), grooves were cut into the concrete before testing at the location of the thermocouple trees to force cracking to occur where the measurements were being taken. These grooves were located over thermocouple trees two and four from the left, see Fig. 3.1. This proved very successful as the crack locations were then fixed whereas the crack widths were not altered. Dimensions of these pre-testing cut grooves were 1mm thick (thickness of the cutting blade) by 5mm deep (half the thickness of the nominal grade of the coarse aggregate) and spanned the width of the beam.

3.2.2 Materials

Portland-fly ash cement conforming to BS EN 197-1:2000 (BSI 2000a) with a percentage fly ash of 5% to 7% was used throughout the experimenal programme. The chemical composition of this cement is detailed in Table 3.3.

The course aggregate was uncrushed and had a nominal diameter of 10mm. The fine aggregate was also uncrushed and was characterised as 80% passing a 600μmm sieve. The design ratios of cement, coarse aggregate, fine aggregrate and water are

Table 3.2: Concrete mixing ratios for the investigation into the thermal propagation through tensile cracks in reinforced concrete.

Cement (kg/m3)	Coarse Agg. (kg/m3)	Fine Agg. (kg/m3)	Water (kg/m3)
454.05	1129.73	635.14	137.84

Table 3.3: Chemical composition of the portland fly-ash (% by weight).

Compound	% weight
CaO	40.9
SiO_2	33.2
Al_2O_3	6.3
Fe_2O_3	4.1
SO_3	1.6
Na_2O	0.1
K_2O	1.2
Insoluble	21.6

shown in Table 3.2. Full design details are reported in Appendix A.

A slump test was carried out to assess the workability of the wet concrete. This was performed in accordance with BS EN 12350-2:2009 (BSI 2009). The slump of the concrete mix for all mixes ranged between 50mm to 65mm.

3.2.3 Concrete Properties

All beams were tested 56 days after casting which consisted of a 28 day curing period for the concrete to reach its characteristic strength with the addition of a further 28 days, required to finalise the setup of the testing apparatus and allow the moisture content to drop further before performing thermal tests. The compressive and tensile strength of the concrete was carried out conforming to BS EN 12390-3:2002 (BSI 2002) and BS EN 12390-6:2000 (BSI 2000b) respectively. The compressive strength, tensile strength and density are shown in Table 3.4. These show that the tensile strength of the concrete is approximately 7% of the compressive strength.

Table 3.4: Concrete compression and tension properties for the specimens used in the investigation into the thermal propagation through tensile cracks in reinforced concrete (based on 32 specimens).

	Compressive Cube strength(N/mm^2)	Split cylinder tensile strength(N/mm^2)	Density kg/m^3
Average	41.1	2.9	2382
Maximum	44.2	3.1	2419
Minimum	38.6	2.6	2328
Standard Deviation	1.8	0.15	21

3.2.4 Damage definition

Critical to the test programme was comparing the heat-transfer in the beams when they were damaged to different degrees. The thermal profiles of beams which were "intact", or had "minor" or "major" damage levels were obtained and compared. To allow the different damage levels to be defined, two beams were loaded without heating (beams 1 and 2 in Table 3.1) and their load-deflection behaviour and crack widths recorded. These definitions of damage are displayed in Fig. 3.5 which plots both mid-span deflection and average crack width against load for the two beams. It is difficult to define these damage states in terms of load applied, in particular for the major damage state. Therefore throughout the experimental program the damage states were defined in terms of their mid-span deflections and as a result the beams were deflection controlled rather than of load controlled. Furthermore, the mid-span deflection was used as the controlling variable as crack widths were only calculated in the post processing of the images. Having a defined mid-span deflection for a defined damage level allowed the beam to be put under the same curvature and hence similar cracking patterns were achieved. As it can be seen from Fig. 3.5, the tolerance of the crack widths ranged from being completely negligible at pre-yielding of the beams to ± 0.7mm at post-yielding of the beams.

Using an average of the load-deflection relationships, transition from elastic to plastic behaviour was found to occur at a mid-span deflection of 3mm and the ultimate load at a deflection ranging from 6mm to 20mm whereby the failure of the beam occurred.

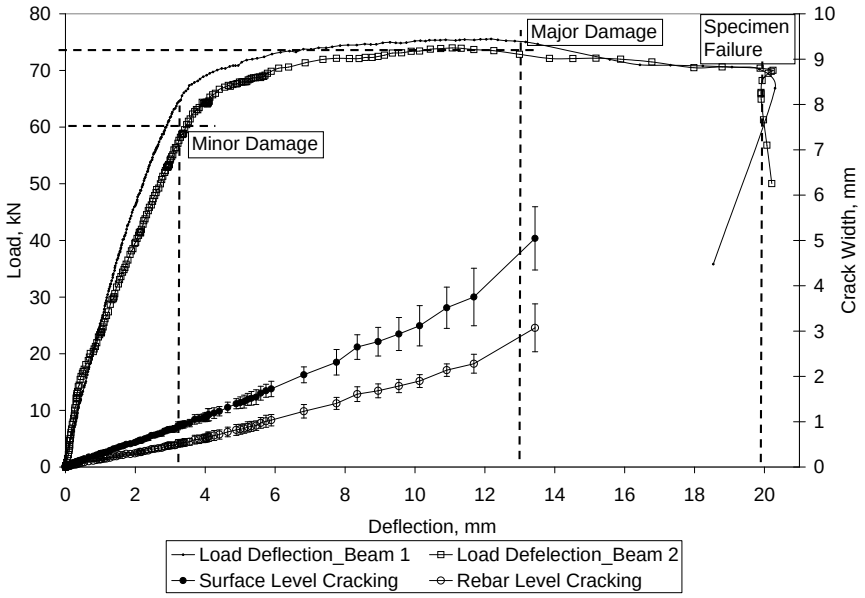

Figure 3.5: Plot showing the load versus mid-span deflection relationship (left axis) and crack width versus mid-span deflection (right axis) for the unheated beams (beams 1 and 2) as given in Table 3.5 for the investigation into the thermal propagation through tensile cracks in reinforced concrete.

Therefore, minor damage was defined as a deflection of 3mm giving crack widths of 1mm at the surface and 0.5mm at the reinforcement level. A state of a major damage was defined at a deflection of 13mm giving crack widths of 5mm (±0.7mm) at the surface and 3mm (±0.5mm) at the reinforcement level (see Table 3.5). These tolerances are calculated from the range of crack widths obtained from all mechanically loaded beams.

Table 3.5: Summary of the damage states defined for the investigation into the thermal propagation through tensile cracks in reinforced concrete. The load, mid-span deflection and average crack widths at the tensile surface and reinforcement levels are defined.

	Undamaged	Minor damage	Major damage
Load (kN)	0	60	74
Mid-span deflection (mm)	0	3	13
Average surface crack Width (mm)	0	1	5±0.7
Average rebar level crack Width (mm)	0	0.5	3±0.5

A mid-span deflection of 3mm was chosen to define a state of minor damage as this is the point where the tensile steel in an unheated beam ceased to behave elastically. This state may be reached under serviceability loading in a typical structure. Within the context of the load-deflection curve of the beam, this point lay at the end of the initial bilinear relationship that encompasses the onset of the tensile cracking of the concrete and the elastic behaviour of the tensile reinforcement.

A mid-span deflection of 13mm was chosen to define a state of major damage for a number of reasons, the foremost of which was its location on the load-deflection-crack width plot. It lay approximately half way through the plastic range of the beam and produced sufficiently large tensile cracks. This displacement was also easily held throughout the entire experiment without risk of runaway failure.

3.3 Thermal profile comparison

The maximum temperatures within the system reach approximately 1200°C at the surface of the radiant heating panel, 800°C at the surface of the beams and the temperatures within the beams range from 425°C 10mm from the surface to 250°C at the level of the reinforcement.

The key results from the tests are shown in Fig. 3.6 and Fig. 3.7 which compare the thermal profiles recorded in the undamaged sections with those recorded in sections with minor and major damage respectively. Temperatures are plotted at depths of 10mm to 40mm from the heated face of the beams. In each case the temperatures plotted are the average of all thermocouples at the appropriate depth for the beams tested.

In both figures there is a clear change in gradient at about 100°C for all curves. This is caused by the latent heat required to evaporate the moisture from the concrete during heating. Throughout the heating phase, differences are seen between the damaged and undamaged beams while during cooling the differences are no longer present. The differences are largest for the case of major damage (Fig. 3.7) and also at greater depths. The recorded differences in temperatures between the damaged and undamaged beams

remain small at all times (a peak difference of about 10% occurs for major damage at around 2000s and 40mm depth). Fig. 3.8 to Fig. 3.10 illustrates the variation of the recorded temperatures of the beams for each magnitude of load.

Fig. 3.11 and Fig. 3.12 show the curves from individual thermocouples at depths of 10mm and 40mm. Individual curves are either associated with thermocouples that were on a crack line or with thermocouples in concrete that remained uncracked. The different numbers of curves in the two figures is due to some thermocouples not being located sufficiently precisely; as noted above these were ignored in all results. It is clear from these figures that local temperatures around cracks were only marginally higher than in the surrounding concrete. This indicates that the cracks were not the cause of the lower average temperatures found in the damaged sections. A further possible source of error is due to the curvature of the damaged beams. Spacing between the radiant heat panel and the section was measured at the mid-span therefore it is important to note that larger mid-span deflections as occurring in the damaged beams will have caused off-centre thermocouples to be fractionally further from the radiant heat panel than with the undamaged beams. This additional spacing to off-centre thermocouples due to the curvature is, at maximum, of the order of 1mm but may still contribute somewhat to the lower temperatures observed. Furthermore, the combined effect from small variations in the concrete mixes, crack widths, thermocouple placement in the specimens and spacing between the specimen and radiant heat panel may have contributed to the small differences in the thermal profiles as observed.

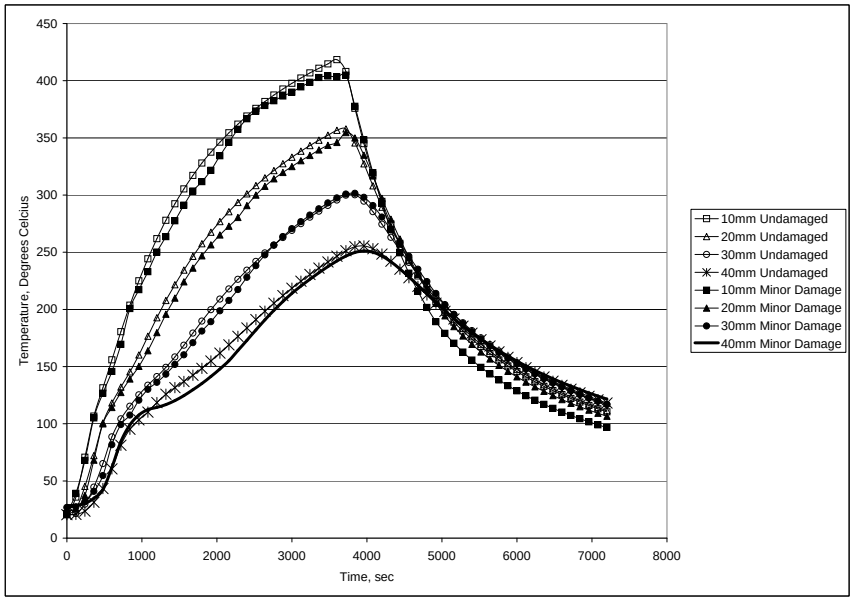

Figure 3.6: Comparison of temperature profile for undamaged and minor damaged sections for the investigation into the thermal propagation through tensile cracks in reinforced concrete.

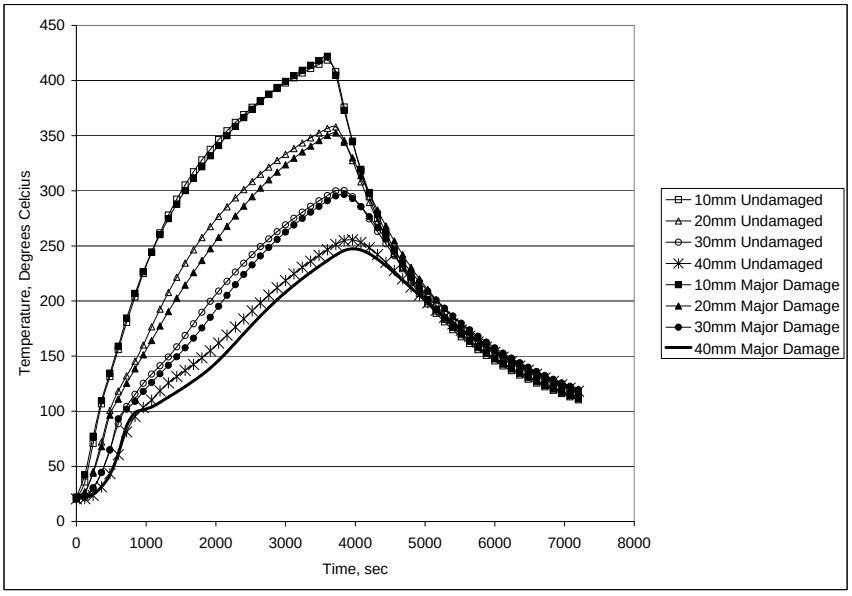

Figure 3.7: Comparison of temperature profile for undamaged and major damaged sections for the investigation into the thermal propagation through tensile cracks in reinforced concrete.

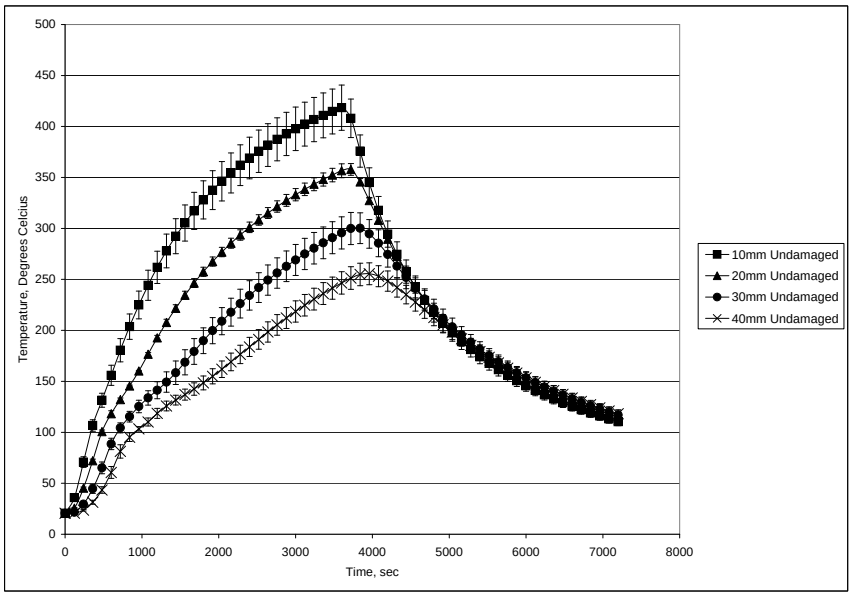

Figure 3.8: A plot showing one standard deviation from the average temperature at different depths into the concrete cover of an undamaged beam for the investigation into the thermal propagation through tensile cracks in reinforced concrete.

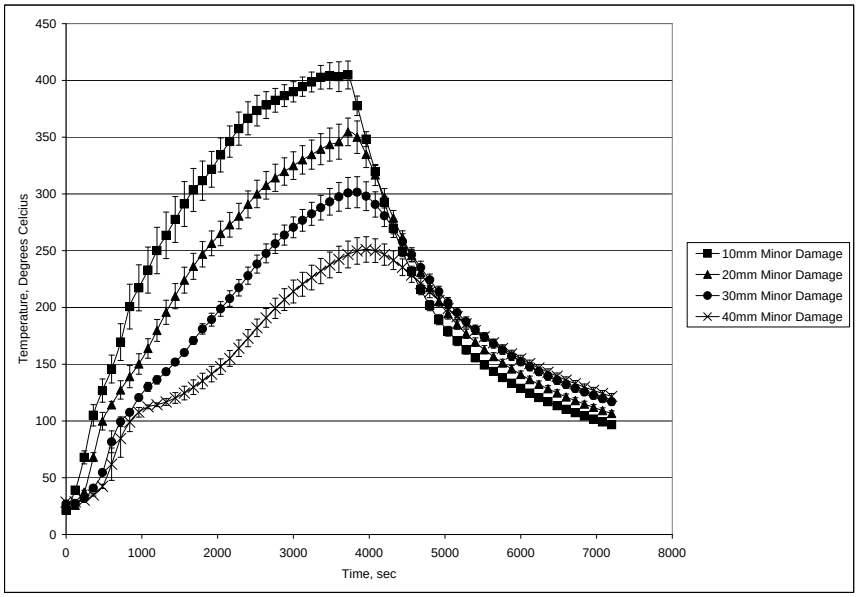

Figure 3.9: A plot showing one standard deviation from the average temperature at different depths into the concrete cover of a beam subject to minor damage for the investigation into the thermal propagation through tensile cracks in reinforced concrete.

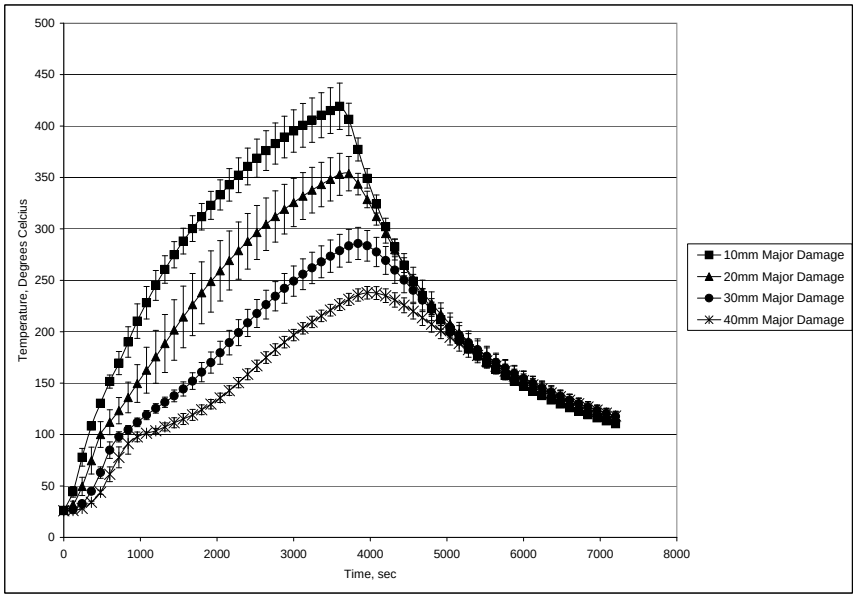

Figure 3.10: A plot showing one standard deviation from the average temperature at different depths into the concrete cover of a beam subject to major damage for the investigation into the thermal propagation through tensile cracks in reinforced concrete.

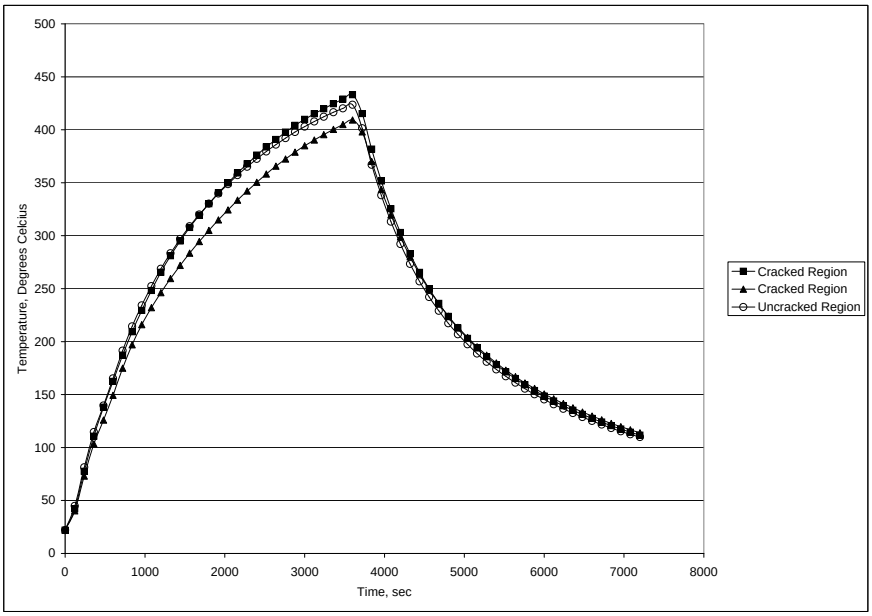

Figure 3.11: Temperature variations at 10mm from the tensile surface of thermocouples within the cracked regions and without the cracked regions for a specimen under major damage for the investigation into the thermal propagation through tensile cracks in reinforced concrete.

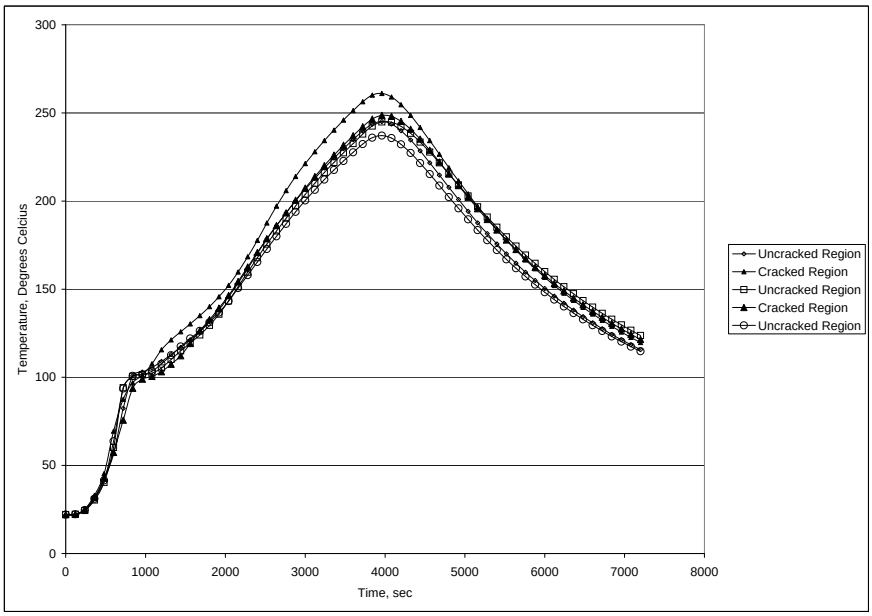

Figure 3.12: Temperature variations at 40mm from the tensile surface of thermocouples within the cracked regions and without the cracked regions for a specimen under major damage for the investigation into the thermal propagation through tensile cracks in reinforced concrete.

3.4 Conclusions

The main conclusion of this work is that that there is no significant increase or decrease in the thermal propagation through concrete with tensile cracking where the cracks are up to the order of 10^1mm at the heated surface. That is, hypothesis III is broadly accepted while hypotheses I and II are rejected. This conclusion is significant because it implies that, in calculations, material thermal properties do not need to be made a function of strain or crack width for these conditions. This information is particularly relevant for numerical simulations because it means that performing a thermal and then a mechanical analysis of heated structures sequentially, as is typically undertaken currently, remains a valid approach. It remains the case that fully coupled thermal-mechanical analyses, which involve substantially more complex numerical solutions, are not necessary for structural fire calculations even when significant tensile damage is induced in the structure.

Three points need to be kept in mind with the above conclusion. Firstly, while the maximum crack width considered in the tests reported is large by normal standards, it is possible that larger cracks still could develop in severely deformed redundant structures. There clearly must come a point when the size of a crack is sufficient to allow more rapid heating of the reinforcement. However, the tests reported here show that this will occur only when the section has undergone substantial plastic rotations and is in its post peak-capacity range (see Fig. 3.5).

Seconly, the effects of convection are not direcly measured due to the heating being performed from above. Therefore the mechanism of convection still needs to be studied in greater detail to fully understand the magnitude of its implications.

Thirdly, the results do in fact indicate a minor decrease in the thermal propagation through the concrete when cracked. The most likely reasons for this decrease have been discussed in the previous section but it is not possible at present to be absolutely certain whether its cause is due to experimental shortcomings or other phenomena. Despite this the above conclusion remains valid as the differences in thermal propagation are small in comparison to other uncertainties in concrete material behaviour and, in any case, ignoring a reduction in thermal propagation in calculations would be a conservative assumption.

Chapter 4

Compression damage in reinforced concrete and its effect on the thermo-mechanical behaviour

4.1 Introduction

The area of concrete within a reinforced concrete member can be subdivided up into two distinct regions. First being the central "core" which is the region enclosed by the reinforcement. The second is the concrete "cover" which is the section that encases the reinforcement and fulfills the role of corrosion resistance and provides the majority of the designed passive fire resistance of that member.

During extreme load cases, such as earthquakes, impacts and blasts, excessive deflections, compressive forces and compressive strains can be induced that are above and beyond that which can be resisted without the onset of damage. In the context of reinforced concrete members, these excessive deflections and compressive forces can lead to the crushing of the concrete. Within normal concretes, the cover has little support in the direction "normal" to its face, therefore when the cover becomes crushed, there is little restraint stopping this region from being removed by the forces of gravity or inertial effects. This brings about a scenario where the steel reinforcement, at the location of the crushing, becomes exposed and hence has little to no fire protection, resulting in

any subsequent thermal load possibly leading to an earlier structural failure.

Within this chapter:

(a) a numerical investigation into the location and magnitude of cover loss is carried out and how the thermo-mechanical behaviour is affected in terms of thermal profiles, deflections and column rotations,

(b) the major mechanisms that account for the thermo-mechanical behaviour are outlined,

(c) a new method to automatically simulate the loss of concrete cover as a result from a build up of excessive compressive plastic strains is developed, and

(d) the method above is then applied to a test frame to show how it numerically manifests.

Due to the removal or partial removal of the concrete cover through crushing the reinforcing steel will become subjected to direct heating in localised regions and as a result, the temperature of the reinforcement can not be used as a comparison variable through the simulations. Therefore, the global structural deflections, such as mid-span beam deflection, storey drift and column rotations are used here to compare the different scenarios.

4.2 Numerical Model and Methodology

The results in this chapter were created and analysed using the computer modelling software, ABAQUS. ABAQUS is a finite element analysis (FEA) program that can solve a wide range of simulations. ABAQUS is orientated to solving implicit and explicit analysis such as static, dynamic and thermal problems therefore making it an ideal program to model the behaviour of damaged reinforced concrete structures. ABAQUS also has additional add-on and interface products, as well as being able to interface with third party products which allows the user to make model changes in accordance

with the state of the model. This feature becomes especially useful in representing mechanical damage for a subsequent thermal analysis.

4.2.1 Model description

Many structures, such as office blocks and high rise buildings, are made with reinforced concrete, of which the form is frequently of portal frame design (i.e. beam-column-slab design). Therefore, for this investigation a simple three dimensional reinforced concrete portal frame was created. The dimensions (detailed below) were chosen as realistic dimensions and to coincide with the dimensions used in Chapter 5. It consists of two 2.77m (internal dimension) high columns with a cross-section of 0.3 x 0.3m. The columns are connected at the top by a beam spanning 2.7m (internal dimension) with a cross section of 0.3m wide and 0.23m deep (see Fig. 4.2 and Fig. 4.3). The steel reinforcement cage is discretely modelled and orientated within the concrete frame. The reinforcement is constrained to the concrete frame in all degrees of freedom (DoF's) (i.e. for this study the relevant DoF's were in translation, rotation and temperature). This form of constraint (also known as a "tie") allows the translation and rotational movement as well as the temperature of the steel to be directly correlated to the respective movement and temperature of the surrounding concrete elements. In addition to allowing full access to results such as the stresses, strains and temperatures, modelling the reinforcement in this way allows the modelling of the confining pressure that will be exerted onto the concrete "core".

The column reinforcement consists of 8 x 20mmϕ steel bars acting as longitudinal reinforcement, wrapped by 10mmϕ shear links at 0.075m spacing at the column ends (500mm from foundations and connections) and 0.15m spacing at mid-height. The beam has 6 x 16mmϕ bars acting in the longitudinal direction and has 6mmϕ shear links at 0.1m spacing spanning the full length (see Fig. 4.2 and Fig. 4.3). The columns have a uniform concrete cover of 0.04m to the reinforcement whilst the beam has a uniform cover of 0.025m.

The foundations of the portal frame (i.e. the base of the columns) are considered

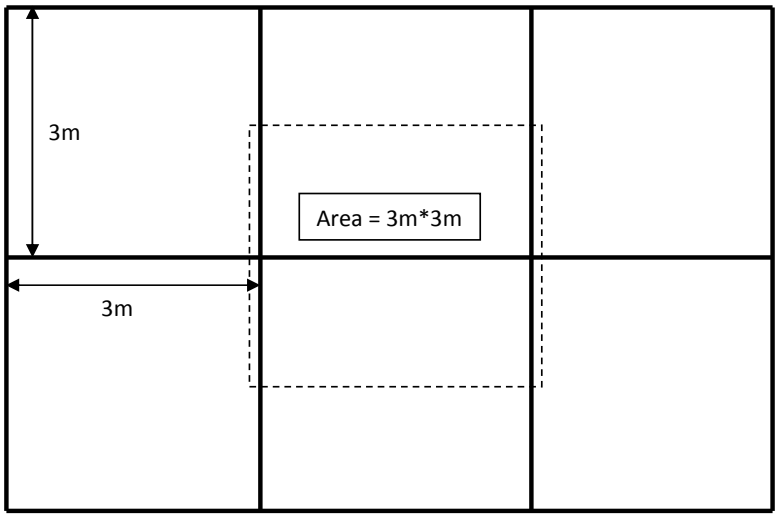

Plan of Building

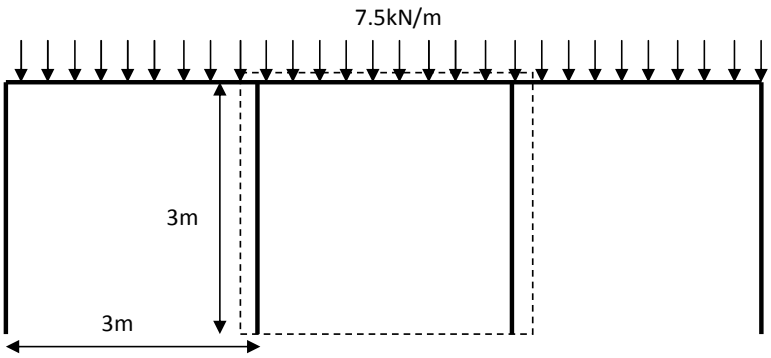

Elevation of Building

Figure 4.1: General layout of the example building used in the numerical analysis for the investigation into the effect of loss of concrete cover. The plan and elevation is given with a bordered segment illustrating the portion of the building to be analysed.

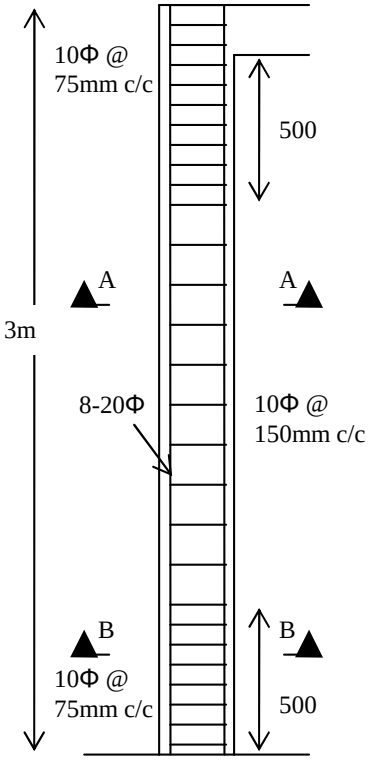

Reinforcement of Column (300x300)

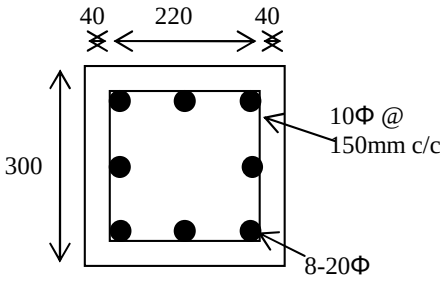

Section A-A

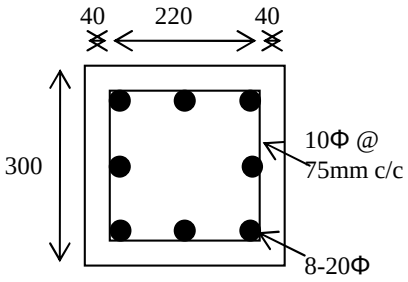

Section B-B

Figure 4.2: Geometrical details of the concrete column and column reinforcement of the example building used in the numerical analysis for the investigation into the effect of loss of concrete cover.

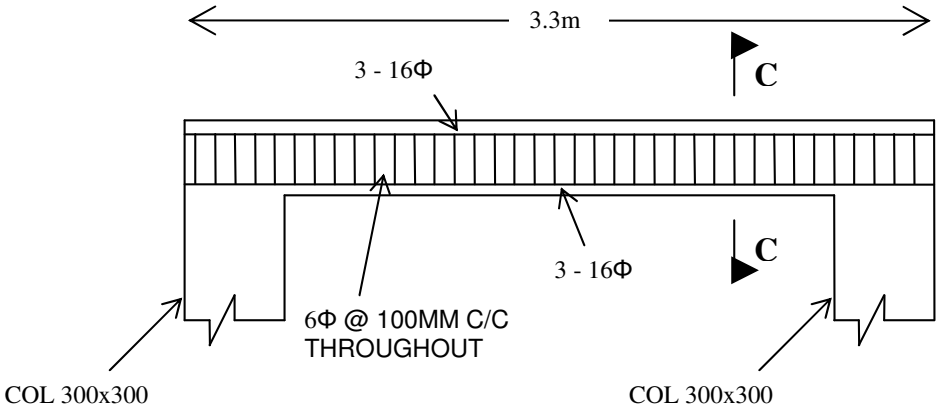

Section of Beam (300 x 230)

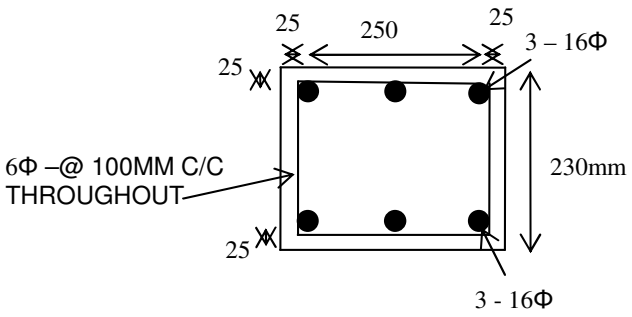

Section C-C

Figure 4.3: Geometrical details of the concrete beam and beam reinforcement of the example building used in the numerical analysis for the investigation into the effect of loss of concrete cover.

to be completely fixed in both translation and rotation whilst the rest of the frame is free to deflect and rotate.

The concrete was modelled using three dimensional solid elements. The reason for this is to insure that the discretely modelled reinforcement picks up the correct temperature from the concrete. Reduced integration is also used (i.e. only one integration point per element) to reduce the computational time. Solid elements are quite a stiff element, therefore a high density of elements are used with each element having nominal dimensions of 0.03x0.03x0.03m (i.e. each column had a cross section of 10 by 10 elements) to allow bending to be accurately modelled. A convergence study was performed on element density and the result are presented in Appendix G

The steel reinforcement was modelled using truss elements with a nominal length of 0.03m which allows all the degrees of freedom (DOF's), including translations, rotations and temperature from the surrounding concrete solid elements to be transferred to the steel reinforcement.

4.2.2 Material properties

Both concrete and steel material properties are assumed to be isotropic, non-linear, temperature dependent and take into account stiffness degradation that will occur through excessive loading. See Chapter 2 and Appendix I for full details. At ambient temperature the steel reinforcement has a yield stress of 415MPa and a modulus of elasticity of 200e^{3}Pa and is assumed to be perfectly elastic plastic. As the temperature increases the strength is reduced in accordance with Eurocode 2 Part 1-2 (2004).

At ambient temperature the maximum stress (f'$_c$) of the concrete is 30MPa at a strain of 0.25% after which it linearly reduces to close to zero at a strain of 1.0%. Again as the temperature increases the strength reduces in accordance with Eurocode 2 Part 1-2 (2004).

These material properties were chosen for this model as to imitate the nominal material properties for the experimental case study as detail in Chapter 5. This was done for continuity reasons throughout the thesis.

To model the removal of the concrete cover, a very simplistic approach is first used. The portion of the cover that has undergone some damage, whether it is on the column or beam, is identified and the conductivity increased by a factor of 100 to allow the thermal transfer to become much more rapid (see Fig. 4.4) hence thermally mimicking the removal of that portion of concrete. It must be noted that this alteration to the conductivity is only applied to the "damaged" section of the concrete cover and does not continue on into the core of the member as the core is assumed to be held in place by the confinement of the reinforcement cage. Furthermore, the compressive and tensile strength of the "damaged" section is reduced to zero to simulate the fact the material is no longer there and hence will no longer fulfill any structural role.

The second method involves utilizing the subroutine detailed in later in this Chapter to continuously simulate the loss of cover throughout the analysis.

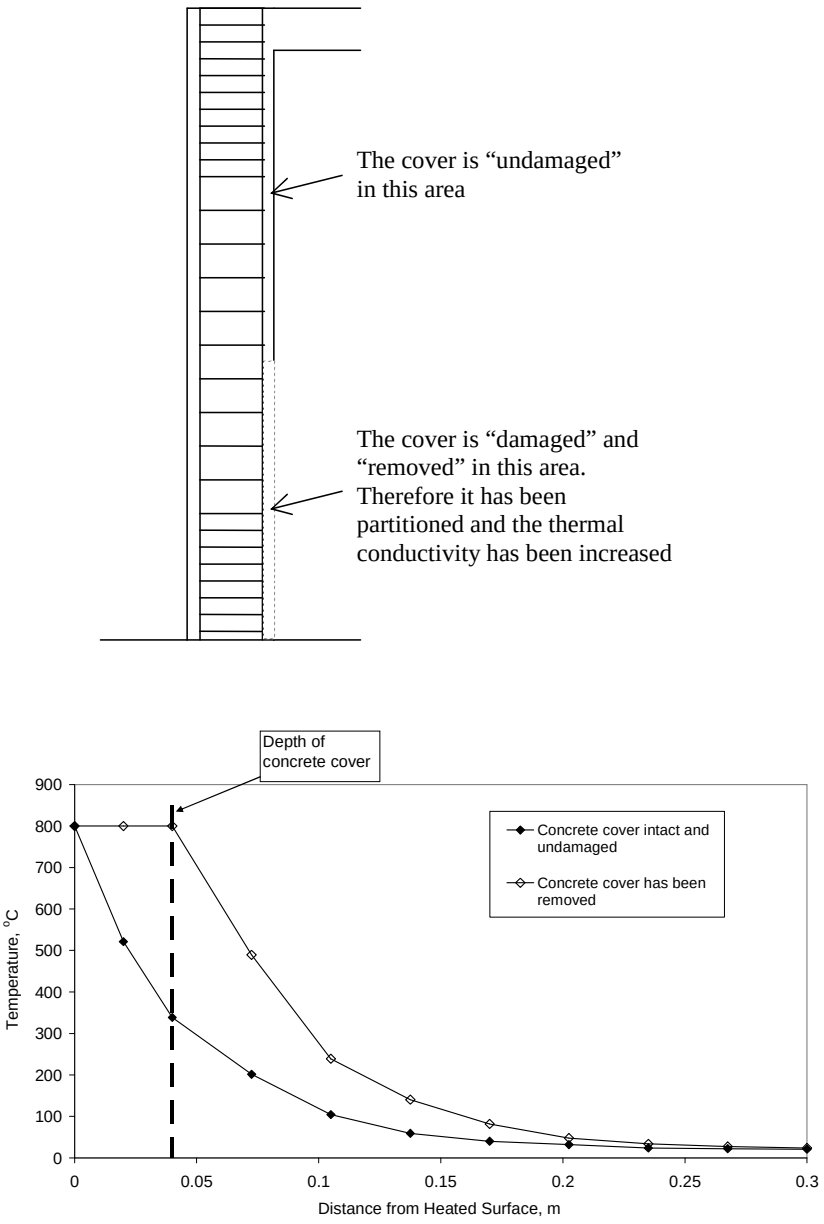

Figure 4.4: Conceptual thermal profile comparison through an intact region and region where there is a loss of concrete cover.

4.2.3 Applied loading

In addition to gravity loading the frame was statically loaded with a uniformly distributed load (UDL) of magnitude 7.5kN/m applied along the length of the beam and

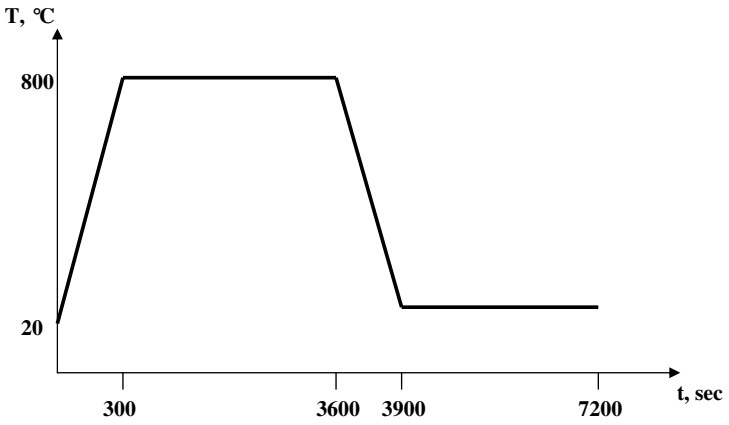

Figure 4.5: Plot of the temperature time relationship applied as a boundary condition to the internal surfaces of the frame (not drawn to scale).

top of columns. This loading is based on "office load, B1" (Eurocode 2005) applied along the over a floor surface area of 3m x 3m (Fig. 4.1). Gravity loading and the UDL is continued throughout the heating and cooling phases of the applied thermal load.

The fire is applied to the internal surfaces of the concrete frame with a thermal boundary condition in the form of a T-t curve (Fig. 4.5). The T-t curve provides a constant temperature of 800^{o}C that is ramped up over a period of the first 300 seconds and is held for a further 3300 seconds (summing to one hour). At this point the temperature is then reduced back to ambient temperature (i.e 20^{o}C) over a period of 300 seconds and held for a further 3300 seconds (summing to a two hour cycle of heating and cooling).

4.2.4 Damaged scenarios

When a reinforced concrete structure becomes damaged due to some extreme loading there are two generalised locations where compression damage occurs; the first being the columns and the second being the connecting beams (Fig. 4.6. The damage locations used in this study are extrapolated from the generalised locations that would occur from a horizontal cyclic motion. (i.e. base of the columns and on the beam near the

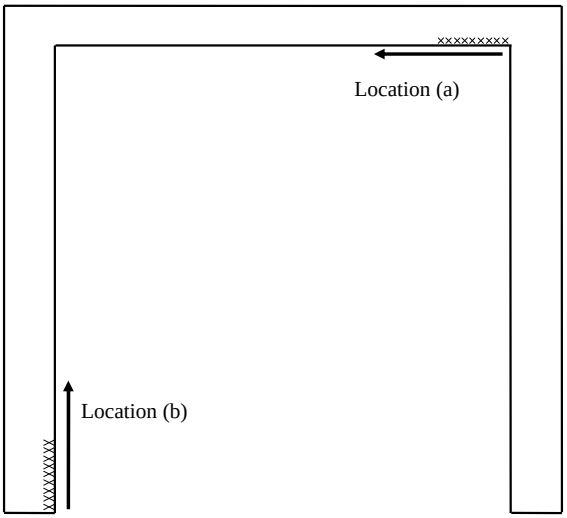

Figure 4.6: Conceptual diagram illustrating where compressive damage and cover removal occurs in correspondence with "Location a)" and "Location b)".

beam-column connection). Therefore, the two separate locations to which damage is applied to the concrete cover is defined as;

Location a) along the internal side of the beam only. The magnitude of the damage starts from the right-hand connection and incrementally increases in length across the length of the beam until all cover is removed from the internal face, and

Location b) along the internal side of the left-hand column only. The magnitude of the damage starts from the base and incrementally increases in length up the height of the column until all cover is removed from the internal face.

The locations as described above are the generalised locations of each damage scenario. Table. 4.1 fully details all damage cases taken into account throughout the feasibility study.

Table 4.1: Damage cases to be performed for the investigation into the loss of concrete cover and its effect on the thermo-mechanical behaviour.

Damaged Case	Damage Location	Damage Magnitude
Undamaged	No Damage	N/A
B2	Location a	2% of internal length
B4	Location a	4% 〃
B10	Location a	10% 〃
B20	Location a	20% 〃
B40	Location a	40% 〃
B50	Location a	50% 〃
B100	Location a	100% 〃
C2	Location b	2% of internal height
C4	Location b	4% 〃
C10	Location b	10% 〃
C20	Location b	20% 〃
C40	Location b	40% 〃
C50	Location b	50% 〃
C100	Location b	100% 〃

4.3 Results and Discussion

4.3.1 Undamaged frame

The undamaged reinforced concrete portal frame, illustrated in Fig. 4.2 and Fig. 4.3 when subjected to a thermal load undergoes a number of mechanical and thermal processes over time, as shown in Fig. 4.7 to Fig. 4.8. Prior to the application of the thermal load, the portal frame is subjected to a vertical mechanical load as previously described in Section 4.2.3. This static loading produces an initial mid-span downwards deflection of 0.00041m (0.41mm) and causes an inward rotation of the top of the columns (Fig. 4.8(b)). When the thermal load is initially applied ($0 \leq t \leq 200$ seconds), the relative mid-span deflection (i.e. the differential deflection between the mid-span and the tops of the columns) reduces due the expansion of the internal sides of the columns, causing the columns to become more vertical and hence, due to the moment restraint of the connections, pulls the beam up to become more horizontal (Fig. 4.8(c)). However, as the thermal front propagates through the concrete ($200 \leq t \leq 450$ seconds), the temperature of the lower face of the beam and the lower steel reinforcement within the beam

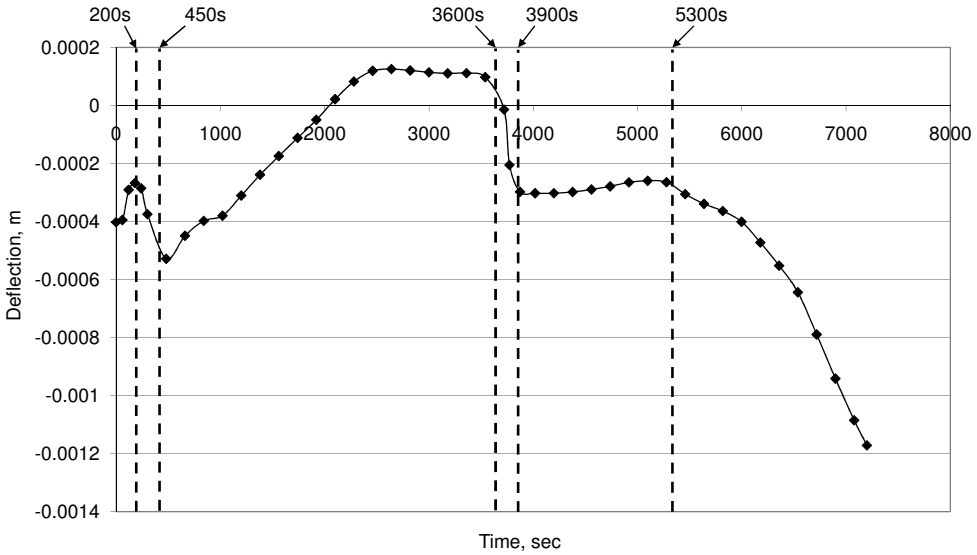

Figure 4.7: Plot showing the mid-span beam deflection of an undamaged portal frame subjected to the thermal loading defined in Fig. 4.5

increases causing thermal expansion and the material strength and stiffness to degrade. This reduction in material properties means that the beam new provides less restraint to the applied static loading and together with expansion of the lower face of the beam the relative mid-span deflection increases once again (Fig. 4.8(d)). This is further illustrated by Fig. 4.9 which is explained later. As the thermal load continues ($450 \leq t \leq 3600$ seconds) the moment restraint of the connections becomes more dominant. The inner reinforcement of the columns begin to increase in temperature causing the columns to continue to rotate outwards and effectively pull the beam up to the point whereby the mid-span of beam rises above the top of the columns (Fig. 4.8(e)).

After the heating phase, the internal faces of the portal frame were subjected to the cooling phase, detailed in Fig. 4.5. Initially ($3600 \leq t \leq 3900$ seconds) the cooling of the columns is the most dominant action. As the internal surfaces of the columns cool and contract, together with the moment restraint of the connection, compresses the beam, forcing it to deflect downwards relative to the column tops (Fig. 4.8(f)). As

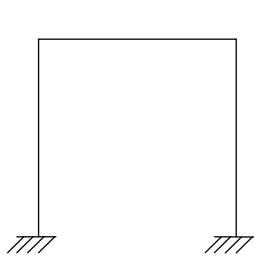

(a) No Loading

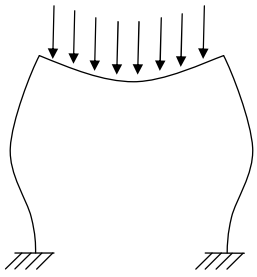

(b) Static Loading

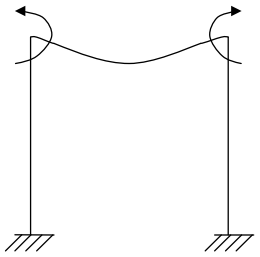

(c) 0 ≤ t≤ 200 seconds

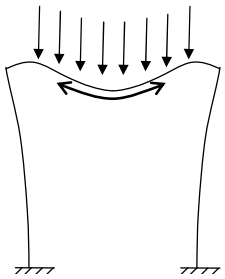

(d) 200 ≤ t≤ 450 seconds

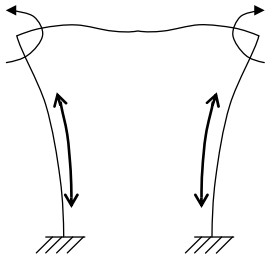

(e) 450 ≤ t≤ 3600 seconds

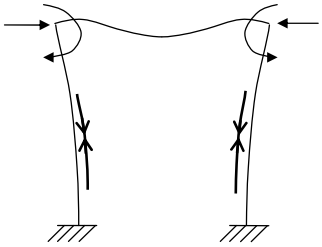

(f) 3600 ≤ t≤ 3900 seconds

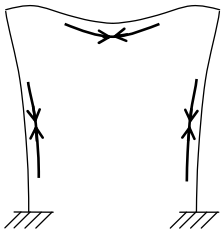

(g) 3900 ≤ t≤ 5300 seconds

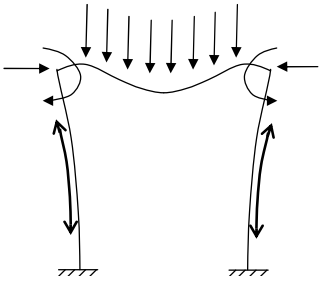

(h) 5300 ≤ t≤ 7200 seconds

Figure 4.8: Illustrations of the conceptual behaviour of the undamaged frame, subjected to the thermal loading defined in Fig. 4.5. Showing applied loads, rotational restraints and thermal expansions and contractions.

the cooling front progresses through the concrete (3900≤t≤5300 seconds) the cooling and contraction of the lower surface of the beam balances out the compressive forces applied from the columns, resulting in the relative mid-span deflection plateauing at an approximate downwards deflection of 0.00027m (0.27mm)(Fig. 4.8(g)). Further into the cooling phase (5300≤t≤7200 seconds), the hot thermal front from propagates to the opposite side of the columns. This causes the expansion of the outer surfaces and reinforcement of the columns resulting in their inward curvature and hence higher axial compressive forces are applied to the beam. These compressive forces, combined with the moment restraint at the connections cause the beam to be pushed further downwards in relation to the column tops (Fig. 4.8(h)). In addition to this, the thermal loading has propagated through to the upper surface of the beam (i.e. the compressive strut), degrading the material properties to the degree whereby the load carrying capacity of the beam is reduced.

To reinforce the idea that the behaviour is mainly dictated by the action of the columns being heated and the rotational restraint at the beam-column connections, two more analyses were carried out as follows:

(a) the removal of the static loading (Fig. 4.9) and

(b) only the beam being subjected to the heating and cooling curve (Fig. 4.10)

Removal of the static loading as shown in Fig. 4.9 illustrates that the static loading in general only affects the magnitude rather than the behavioural trend. The material degradation of the lower steel reinforcement within the beam is not exploited in this case and therefore there is no significant increase in deflection between t=180 seconds and t=420 seconds as previously shown in Fig. 4.7.

The static loading is reapplied and then the analysis is re-run with only the beam loaded thermally. It can be seen from Fig. 4.10 that the beam deflects downwards during the heating phase and contracts backwards during the cooling phase which is indicative of thermal bowing. In this case it can be said that the beam behaves more independently and the columns effectively act as spring-like end supports.

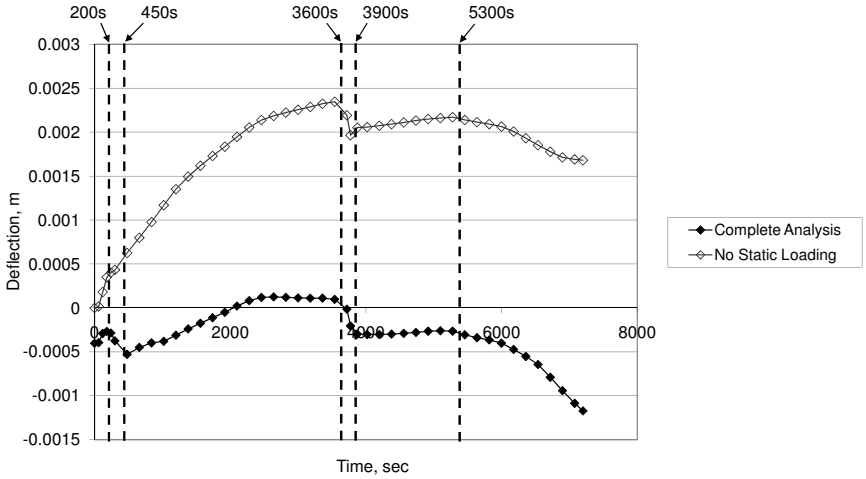

Figure 4.9: Plot showing the mid-span beam deflection of an undamaged portal frame with no mechanical vertical load applied but still subjected to the thermal loading defined in Fig. 4.5.

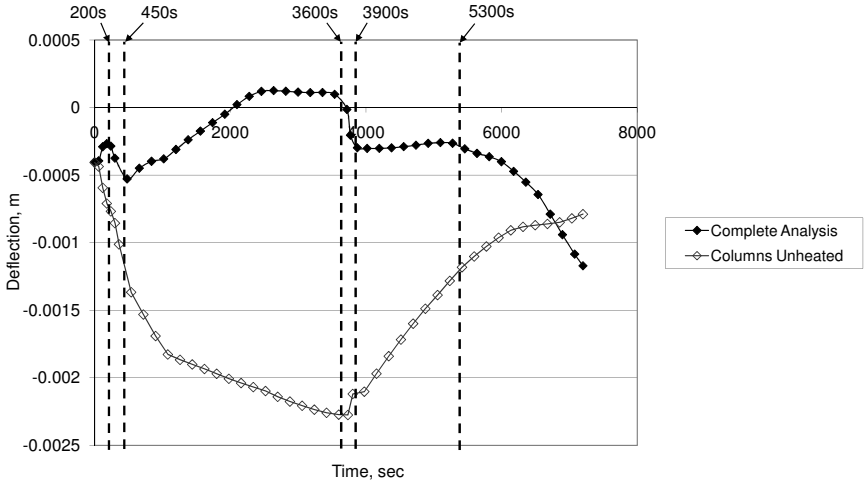

Figure 4.10: Plot showing the mid-span beam deflection of an undamaged portal frame with the columns remaining unheated but the mechanical vertical load applied and the internal surface of the beam is still subjected to the thermal loading defined in Fig. 4.5.

From the behaviour of the undamaged portal frame, it can be concluded that it is not only the thermal expansion and material degradation that is of importance; but that the stiffness of the column-beam connection also plays a major role in the overall behaviour. This behaviour has also been noted by Pankaj et al (2008) where a portal is subjected to a thermal gradient of 2.3^{o}C/cm (hottest on the interior surfaces). They show that "in spite of the temperature gradient which should cause bowing downwards in the beam, joint rotation due to the constant temperature increase causes upwards bowing".

4.3.2 Damage to the beam

This section aims to compare, describe and explain how even a small amount of damage to the concrete cover in the form of the removal of that cover, can have a significant effect on the overall behaviour of a structure. Damage such as cover removal can cause an unsymmetry to occur and localised heating of the reinforcement. For direct comparison to the undamaged state, the case whereby all the cover is removed from the internal face of the beam (B100) is first investigated as this to will be a symmetrical case and therefore the behaviour will not be complicated by horizontal storey drift.

The vertical static load applied to the frame before the thermal loading produces a very similar profile where there was an initial downwards deflection. As the majority of the cover on the lower face of the beam acts in tension (except for small regions around the connections), the loss of this cover did not significantly impact the beam or portal frame's ability to support the load at ambient temperatures. This is shown in the initial mid-span deflections in Fig. 4.11 where the mid-span deflection due to the vertical static load increased to only 0.43mm compared to 0.41mm for the undamaged state. However, as the thermal load is applied the differences between the two frames become much more apparent as the lower reinforcement is directly subjected to the temperature change of the "gas" phase (i.e. fire). When the thermal load is initially applied ($0 \leq t \leq 200$ seconds), the downwards relative mid-span deflection increases rapidly as the lower reinforcement thermally expands and its strength degrades (Fig. 4.13(c)).

However, as the model does not include creep the downwards deflections will not continue to increase within the present thermal state. The thermal load continues to be applied ($200 \leq t \leq 3600$ seconds) and, as seen with the undamaged frame, the outwards curvature of the columns cause the upwards deflection of the beam, once again to the point whereby the mid-span of beam rises above the top of the columns as seen in (Fig. 4.13(d)). The magnitude of this upwards deflection is much greater than that experienced by the undamaged frame for a combination of reasons. Firstly, as the cover has been removed the cross-section of the beam has become reduced, therefore temperatures throughout the depth are hotter than those experienced within

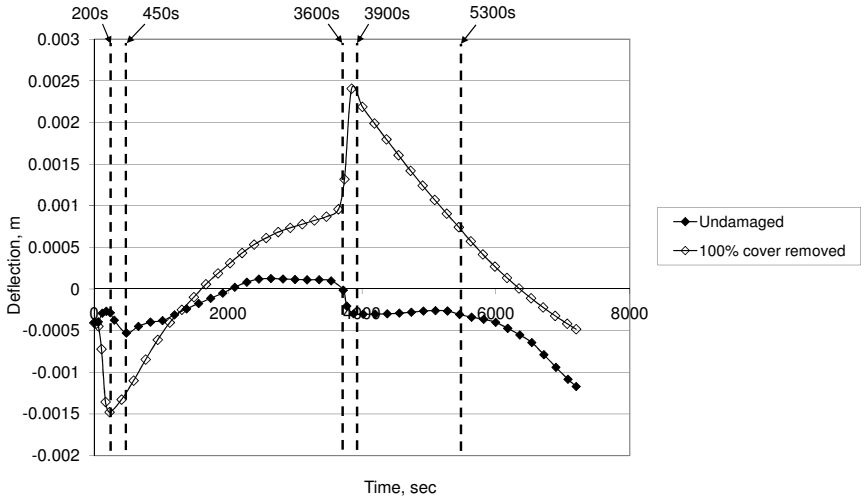

Figure 4.11: Plot showing the mid-span beam deflection of a portal frame with 100% cover removed from the heated surface of the beam subjected to the thermal loading defined in Fig. 4.5. A comparison to the mid-span beam deflection of an undamaged portal frame is made.

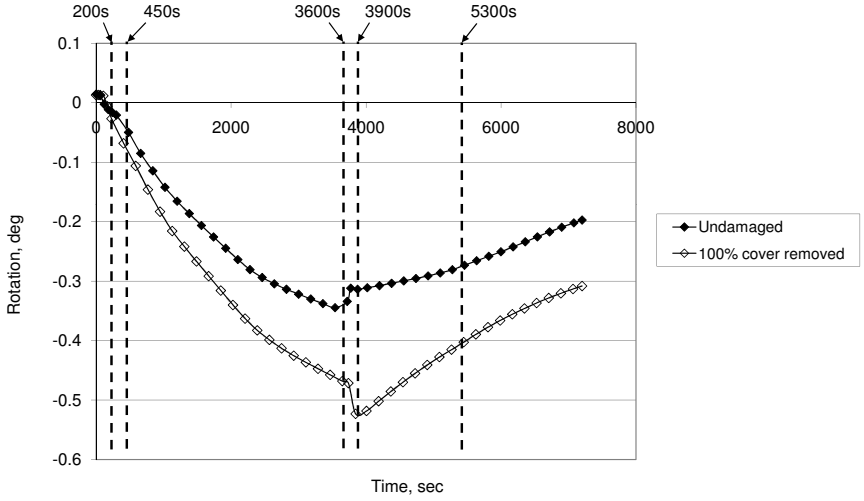

Figure 4.12: plot showing the column rotation within a portal frame with 100% cover removed from the heated surface of the beam subjected to the thermal loading defined in Fig. 4.5. A comparison to the mid-span beam deflection of an undamaged portal frame is made.

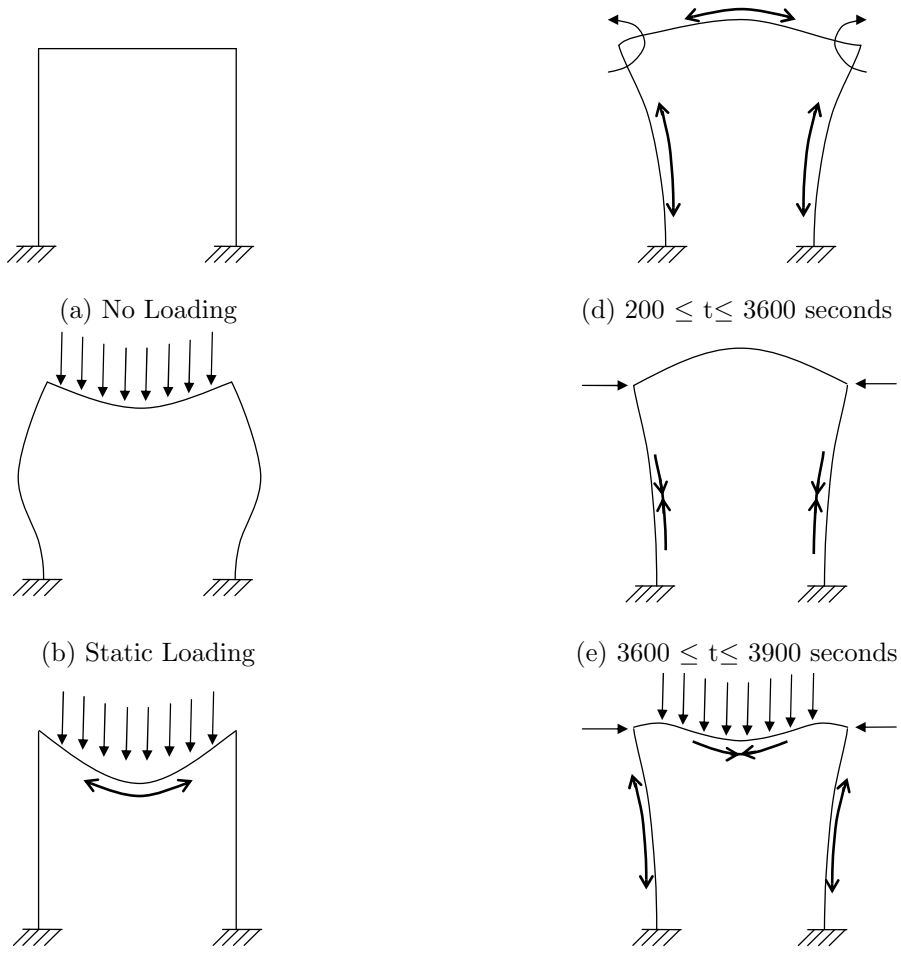

(a) No Loading

(b) Static Loading

(c) 0 ≤ t≤ 200 seconds

(d) 200 ≤ t≤ 3600 seconds

(e) 3600 ≤ t≤ 3900 seconds

(f) 3900 ≤ t≤ 5300 seconds

Figure 4.13: Illustrations of the conceptual behaviour of the frame with 100% cover removed from the heated surface of the beam, subjected to the thermal loading defined in Fig. 4.5. Showing applied loads and thermal expansions and contractions.

an undamaged frame causing more of the beam to become weaker. Secondly, as the cross-section has been reduced, this provides less restraint to the columns and allows the columns to bow more freely and as a result pull the beam upwards (Fig. 4.12).

As the frame enters the cooling phase ($3600 \leq t \leq 3900$ seconds) the relative mid-span deflection, in contrast to the behaviour of the undamaged, rapidly increases upwards (Fig. 4.11 and Fig. 4.13(e)). This rapid upward deflections occurs for a number of reasons. Firstly, the initial upwards deflection of the beam at the start of the cooling phase is sufficient enough for the cooling and contraction of the lower face of the beam to causes an upwards deflection indicative of an independently acting member. Secondly, the fact that the beam is much weaker, the cooling and contracting of the internal surfaces of the columns, together with the weaker moment restraint of the connection, compresses the beam, causing it to deflect upwards rather than downwards. As the cooling of the frame continues ($3900 \leq t \leq 7200$ seconds) the relative mid-span deflection reduces almost linearly as illustrated in Fig. 4.11. This reduction in deflection is explained by the same process described for the undamaged frame where the thermal profile reaches the outer surfaces causing loss of the carrying capacity of the beam.

The behaviour of the portal frame becomes even more complicated when the damage to the beam is unsymmetric which leads to non-uniform heating (illustrated in Fig. 4.18) and storey drift occurring in the structure. These storey drifts, measured at the mid-span of the beam, increases with the level of damage applied (B2 to B50) as shown in Fig. 4.17. This drift is a result of the unsymmetric geometry causing a change in thermal boundary and a different beam-column rotational restraint for each case. Most of the cases (B2 to B20) follow the same form of the undamaged frame with the differences being explained by the change and reduction of rotational restraint of the damaged beam-column connection. As shown in Fig. 4.15 throughout the heating phase ($0 \leq t \leq 3600$ seconds) the rotations of the left column (i.e. undamaged side) remains virtually unchanged in comparison with the rotations of the undamaged frame, whereas the rotation of the right column (i.e. damaged side) due to thermal bowing increases with damage (Fig. 4.16). Initially, as the thermal load is applied

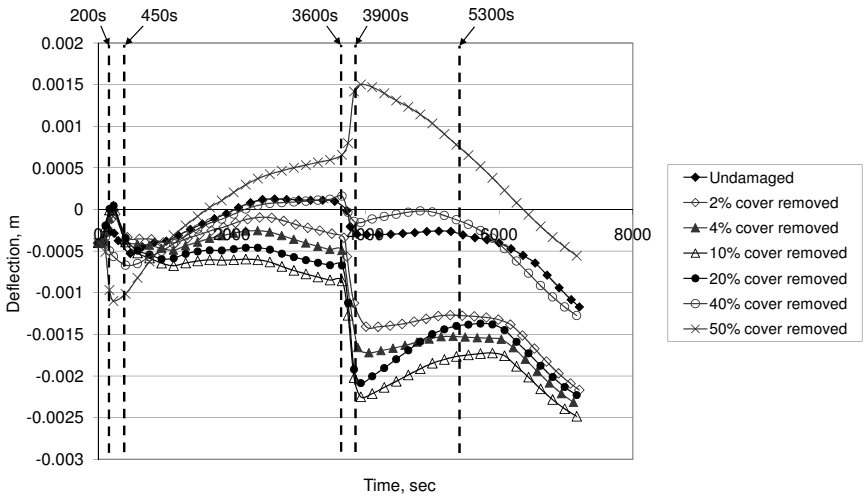

Figure 4.14: Plot showing the mid-span beam deflection of a portal frame with varying degrees of cover removed from the heated surface of the beam subjected to the thermal loading defined in Fig. 4.5.

($0 \leq t \leq 200$ seconds), the frame as a whole drifts to the left. This is directly due to the difference in rotational restraint provided by the beam-column connections, illustrated in Fig. 4.19(c). The undamaged connection is stiffer and therefore the bowing of the column on the undamaged side is able to pull the frame in that direction, while the damaged area of the beam expands and its strength degrades more rapidly. However, as the thermal load continues to be applied ($200 \leq t \leq 3600$ seconds) the lower reinforcement at the damaged region reaches its maximum temperature, and as creep is not included, the thermal expansion and strength degradation. However, this reduction in strength of the damaged area reduces the rotational stiffness of the beam-column connection allowing the column on the damaged side to rotate and bow more freely. This thermal bowing then pulls the frame, as a whole, to the right as seen in Fig. 4.17 and Fig. 4.19(d) and(e).

When the damage exceeds 20% of the length of the beam (i.e. B40 and B50), the beam behaviour begins to change. The initial behaviour ($0 \leq t \leq 200$ seconds) is more dominated by the thermal expansion and material degradation of the exposed

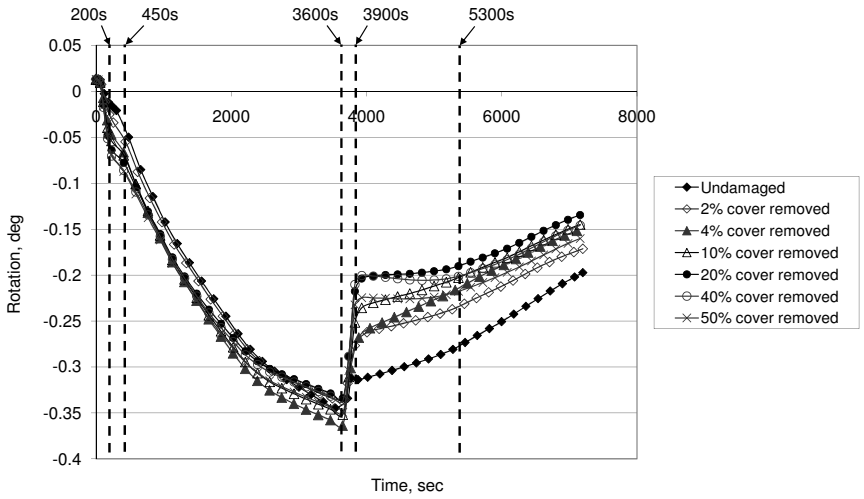

Figure 4.15: Plot showing the column rotation of damaged side within a portal frame with varying degrees of cover removed from the heated surface of the beam subjected to the thermal loading defined in Fig. 4.5.

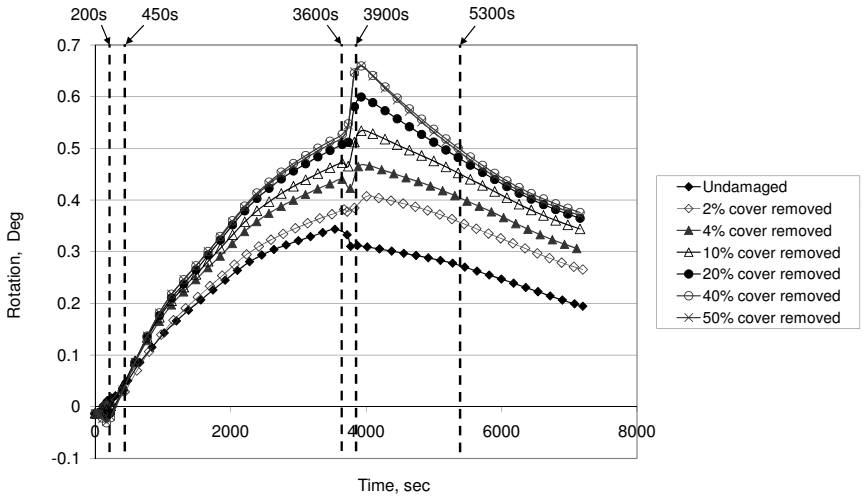

Figure 4.16: plot showing the column rotation of undamaged side within a portal frame with varying degrees of cover removed from the heated surface of the beam subjected to the thermal loading defined in Fig. 4.5.

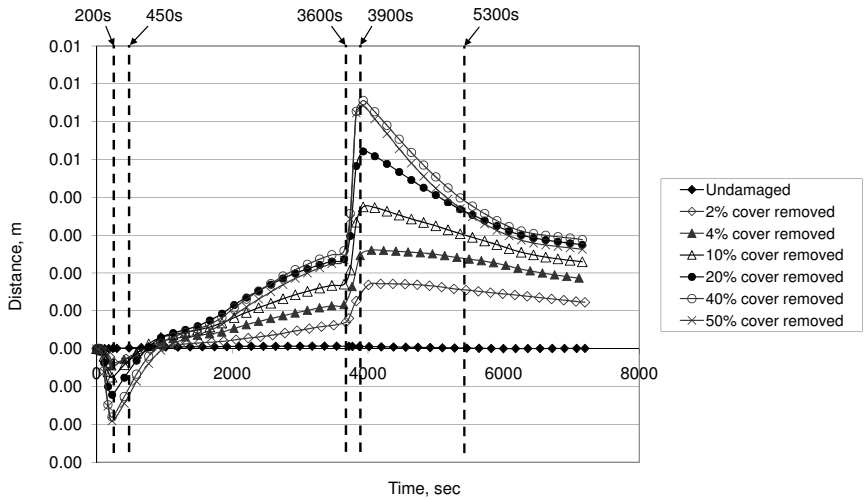

Figure 4.17: Plot showing the storey drift of a portal frame with varying degrees of cover removed from the heated surface of the beam subjected to the thermal loading defined in Fig. 4.5.

reinforcement, similar ro B100. Also in these cases, as the thermal load continues to be applied ((200≤t≤3600 seconds), the reduced beam section allows the columns to rotate more freely, pulling the beam upwards as illustrated in Fig. 4.14 to Fig. 4.16.

As the frame enters the cooling phase (3600≤t≤3900 seconds) the difference in the rotational stiffnesses of the connections once more plays a major role. Both columns cool at the same rate but as the damaged beam-column connection (right) is more flexible than the undamaged connection (left), this cooling allows the left column to effectively push the frame further, resulting in a sharp increase in the storey drift to the right as shown in Fig. 4.17. In addition to this, the frame with damages up to 20% demonstrate a sharp increase in downwards relative mid-span deflection whilst damages exceeding 50% have a sharp increase in upwards relative mid-span deflection.This change in deflection behaviour is due to a reducing beam section with the increase in damage. As the beam becomes weaker, the compressive forces applied from the cooling of the columns causes the beam to reapidly deflect one way or the other. The direction of the buckling is dictated by the relative deflection of the beam at

the end of the cooling phase. (i.e. buckles upwards above a relative mid-span deflection of 0.5mm).

As the frame continues to cool ($3900 \leq t \leq 7200$ seconds) the mid-span deflection behaviour of the frame with damages up to 40% can be explained through the behaviour of the undamaged frame; whilst the behaviour of a frame with damages exceeding 50% can be explained in the same way as the frame with all the cover removed (B100).

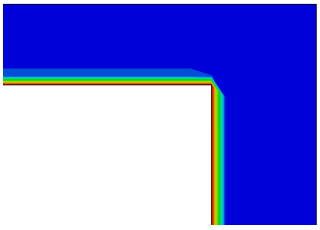

(a) Undamaged frame (300 seconds)

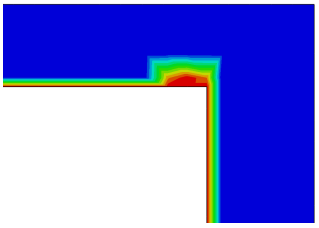

(d) Damaged frame (300 seconds)

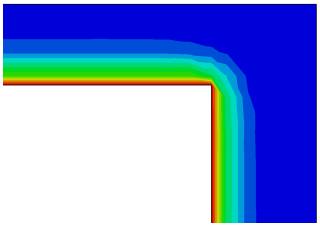

(b) Undamaged frame (3600 seconds)

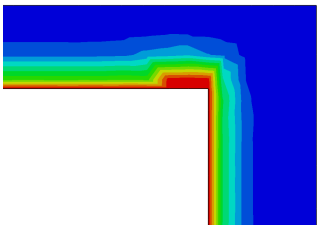

(e) Damaged frame (3600 seconds)

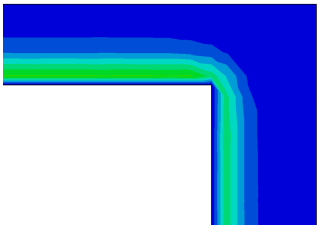

(c) Undamaged frame (3900 seconds)

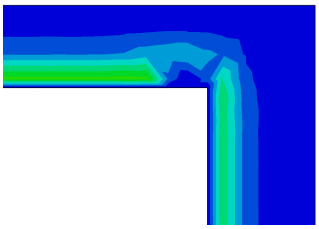

(f) Damaged frame (3900 seconds)

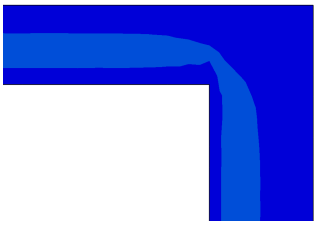

(f) Undamaged frame (7200 seconds)

(f) Damaged frame (7200 seconds)

Figure 4.18: Illustrations showing the thermal profile comparison between an undamaged frame and a frame with 4% concrete cover removed from the heated surface of the beam in correspondence with Fig. 4.6. The difference in thermal propagation can easily be seen. These are figures are for a qualitative comparison only.

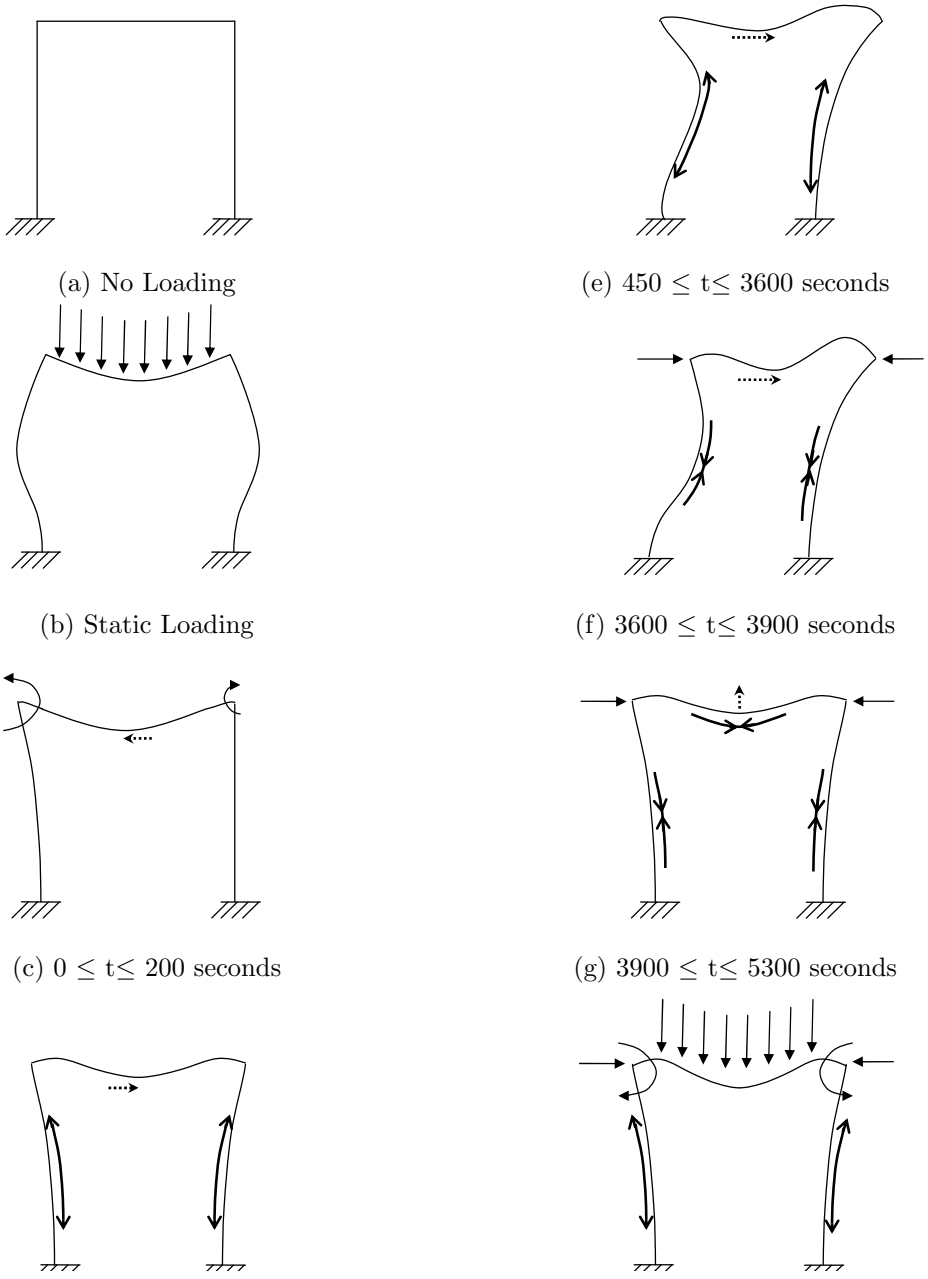

(a) No Loading

(b) Static Loading

(c) 0 ≤ t≤ 200 seconds

(d) 200 ≤ t≤ 450 seconds

(e) 450 ≤ t≤ 3600 seconds

(f) 3600 ≤ t≤ 3900 seconds

(g) 3900 ≤ t≤ 5300 seconds

(h) 5300 ≤ t≤ 7200 seconds

Figure 4.19: Illustrations of the conceptual behaviour of the frame with varying degrees of cover removed from the heated surface of the beam, subjected to the thermal loading defined in Fig. 4.5. Showing applied loads, rotational restraints and thermal expansions and contractions.

4.3.3 Damage to the column

When damage is applied to one of the columns of a simple portal frame, it produces an unsymmetric thermal boundary condition regardless of the level of damage as illustrated in Fig. 4.24. Although the relative mid-span deflection of the beam does not change a great deal for damages up to 50% of the column height (Fig. 4.20), the behaviour still differs greatly from the undamaged frame in terms of storey drift as illustrated in Fig. 4.23. Initially, as the thermal load is applied ($0 \leq t \leq 200$ seconds), the temperature of the reinforcement at the damaged region increases at a much quicker rate. This leads to the damaged column expanding at a quicker rate than the undamaged column resulting in the frame drifting left as illustrated in Fig. 4.23 and Fig. 4.25(c). However, as the thermal load continues to be applied ($200 \leq t \leq 3600$ seconds), the reduction in strenth of the exposed reinforcement (i.e. within the region of damage) weakens the column and allows the undamaged column to expand more freely as shown in Fig. 4.21 and effectively "pull" the frame over, resulting in an overall drift to the right (Fig. 4.23 and Fig. 4.25(d)).

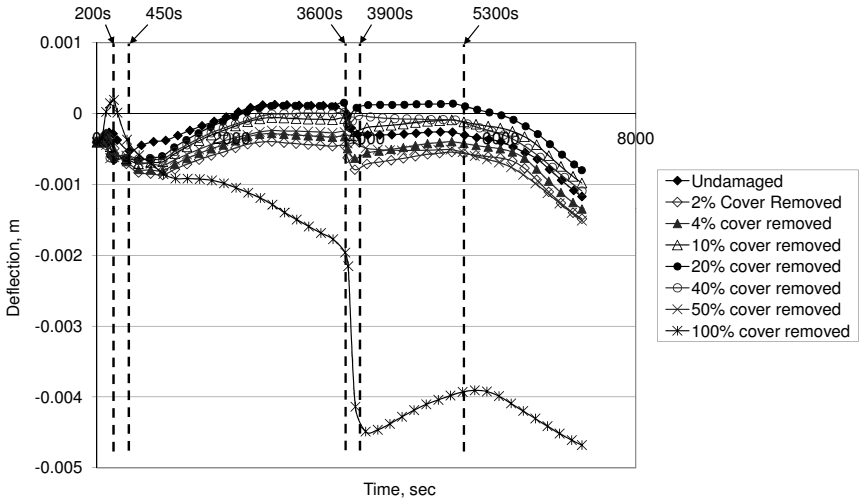

Figure 4.20: Plot showing the mid-span beam deflection of a portal frame with varying degrees of cover removed from the column, subjected to the thermal loading defined in Fig. 4.5.

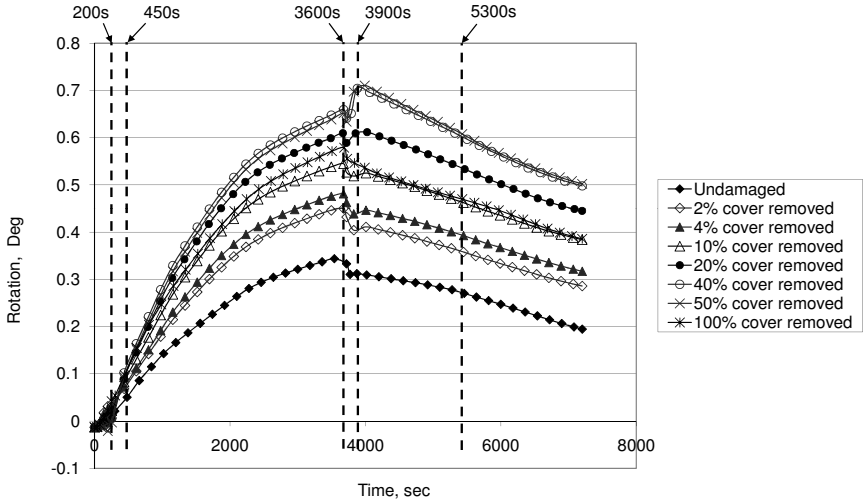

Figure 4.21: Plot showing the column rotation of undamaged side within a portal frame with varying degrees of cover removed from the column, subjected to the thermal loading defined in Fig. 4.5.

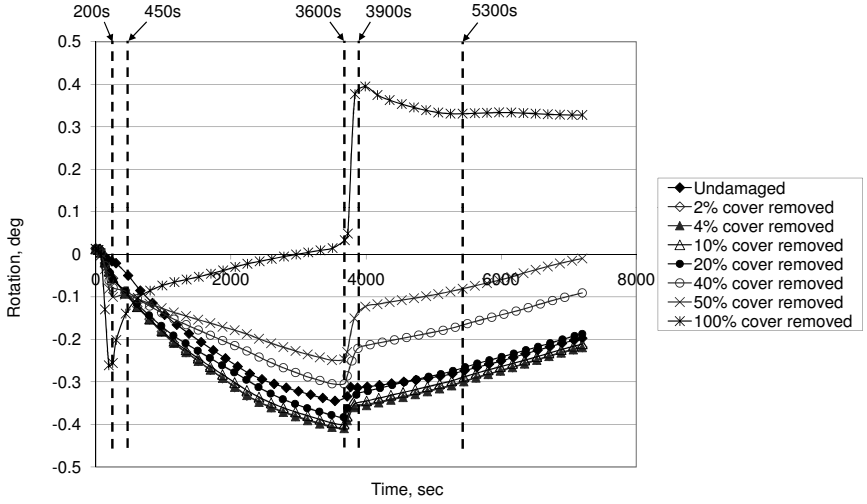

Figure 4.22: Plot showing the column rotation of damaged side within a portal frame with varying degrees of cover removed from the column, subjected to the thermal loading defined in Fig. 4.5.

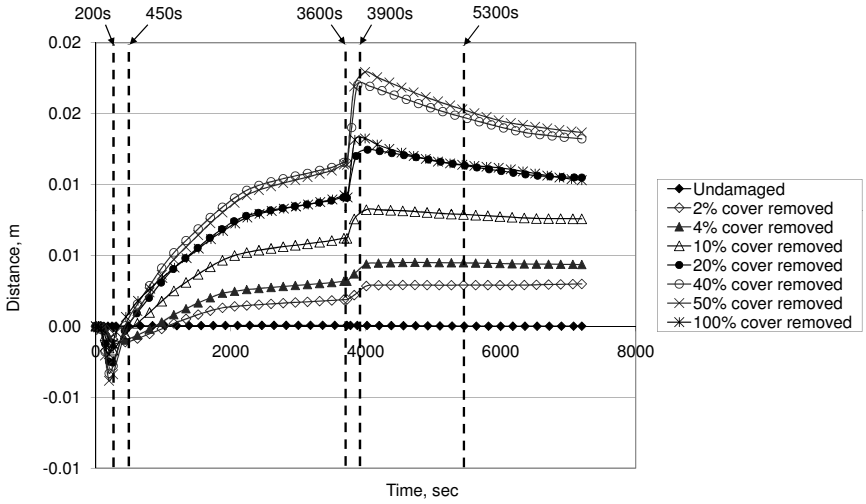

Figure 4.23: Plot showing the storey drift of a portal frame with varying degrees of cover removed from the column, subjected to the thermal loading defined in Fig. 4.5.

As the structure cools ($3600 \leq t \leq 3900$ seconds), the inner reinforcement of the damaged column rapidly contracts in comparison to the inner reinforcement of the undamaged column causing a rapid reduction in the rotation of the damaged column (Fig. 4.21) and effectively "pushes" the frame further to the right as illustrated in Fig. 4.23 and Fig. 4.25(e). Cooling then continues to occur in a similar fashion as the undamaged frame.

It should be noted that when all the cover is removed from the column, which includes causing damage to the beam-column connection, the magnitude of the relative mid-span deflection and the damaged column rotation significantly increase, hence reinforcing the conclusion that the beam-column connection plays a major role in the overall behaviour of the frame.

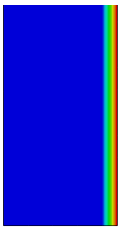

(a) Undamaged frame (300 seconds)

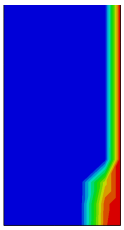

(d) Damaged frame (300 seconds)

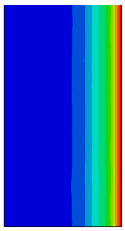

(b) Undamaged frame (300 seconds)

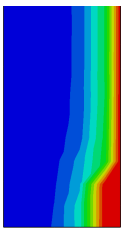

(e) Damaged frame (3600 seconds)

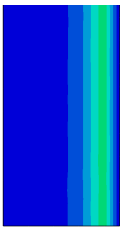

(c) Undamaged frame (300 seconds)

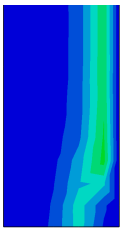

(f) Damaged frame (3900 seconds)

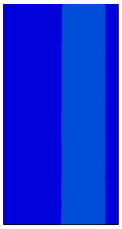

(f) Undamaged frame (300 seconds)

(f) Damaged frame (7200 seconds)

Figure 4.24: Illustrations showing the thermal profile comparison between an undamaged frame and a frame with 4% concrete cover removed from the heated surface of the column in correspondence with Fig. 4.6. The difference in thermal propagation can easily be seen. These are figures are for a qualitative comparison only.

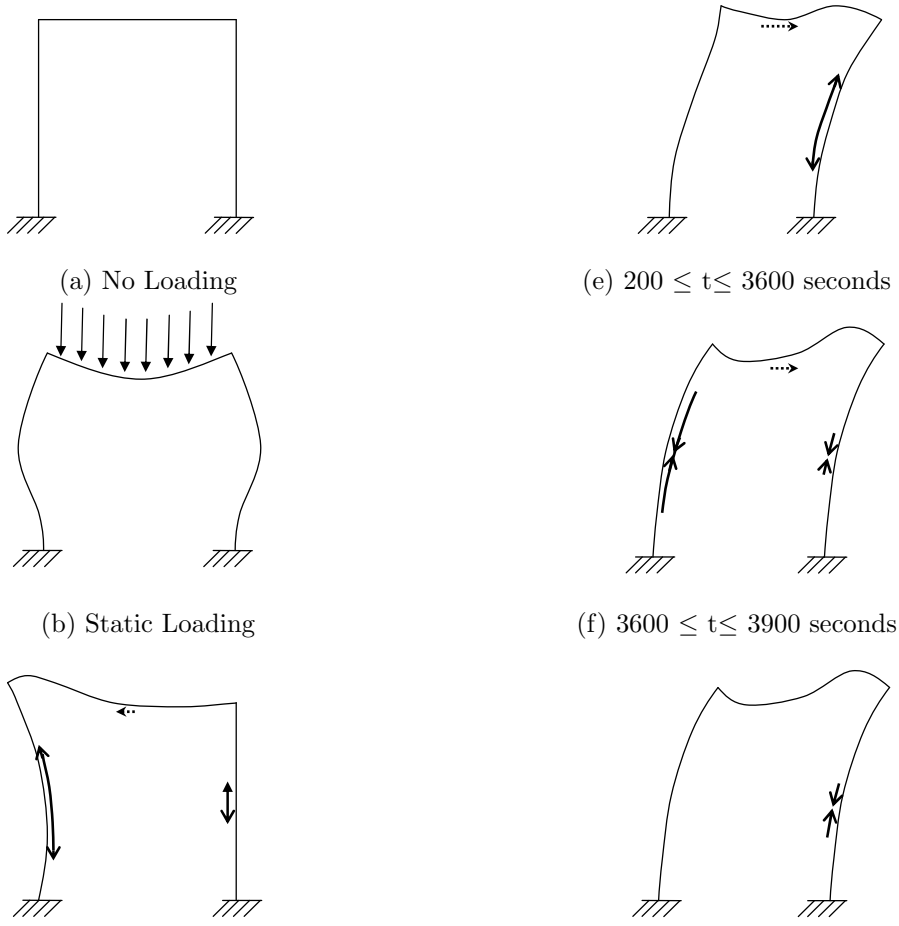

(a) No Loading

(b) Static Loading

(c) 0 ≤ t≤ 200 seconds

(e) 200 ≤ t≤ 3600 seconds

(f) 3600 ≤ t≤ 3900 seconds

(g) 3900 ≤ t≤ 7200 seconds

Figure 4.25: Illustrations of the conceptual behaviour of the frame with varying degrees of cover removed from the heated surface of the column, subjected to the thermal loading defined in Fig. 4.5. Showing applied loads and thermal expansions and contractions.

4.4 A new technique to modelling the loss of concrete cover

4.4.1 Introduction

The concrete cover provides the thermal protection to the steel reinforcement and the loss of this concrete cover can have detrimental effects on the structural behaviour when subjected to a fire load. In reality, for a scenario where the concrete cover has become removed prior to the structure being subjected to a thermal load, the location of the gas phase thermal boundary condition changes. Instead of it being located on the original surface of the intact concrete, the boundary "instantly" jumps into the concrete member which can lead to direct heating of the steel reinforcement.

When a reinforced concrete structure is subjected to an extreme mechanical event that causes excessive compressive damage to the cover it is necessary to calculate the location(s) and magnitude(s) of the damage sustained prior to the application of a thermal load. There are a couple of methods that are already employed:

(a) Manual element removal - This is a method where the user manually removes elements based on some criterion prior to analysis. This has been used for analysis of spalling, (Deeny 2010). However, this method is time consuming and can not adapt automatically throughout the analysis. In addition, this method has the potential to increase the DoF's, leading to an increase in computational run time.

(b) Element removal function - Many analysis programs include an element removal function, which can remove an element if user specified criterion is reached. This method allows the simulation to adapt automatically throughout the analysis and therefore requires less user input. However, this function is generally only available in "explicit" analyses and once again, has the potential to increase the DoF's, leading to an increase in computational run time.

It is clear that a new approach is required to simulate the loss of concrete cover for scenarios where damage is likely to occur without increasing the DoF's and computa-

tional run time. The method described below provides a new novel way of calculating the effective element removal with minimal user input and without increasing the number of DoF's. This method also allows for the simulation to adapt automatically throughout the analysis and is available for both implicit and explicit analyses.

The new approach employed involves the addition of a subroutine to the analysis. The function of this subroutine is not to remove elements but rather to alter the material properties to simulate an element's removal based on a criterion defined by the user. This is achieved by the subroutine gathering information on the state of the structure at all locations at any given time and comparing this to the user defined criterion. When the defined criterion is met, a number of material properties are altered:

(a) - the strength and stiffness of the element(s) are reduced to a very small but finite value,

(b) - the conductivity is increased to allow a thermal load to pass through the element(s) almost instantly, and

(c) - the thermal expansion is also reduced to zero.

4.4.2 Calculation of the user defined criterion for the loss of concrete cover

This section details the method required to calculate the criterion for the loss of cover to be used in conjunction with the subroutine detailed above. It should be noted that the value calculated here is not applicable for every situation and it only used to obtain a value to prove that the method works as anticipated. Therefore, to increase the accuracy of this method, further data will be required, focusing on the strains required to cause this phenomenon within a variety of concrete mixes, concrete cover depths, temperatures and including dynamic considerations.

The loss of concrete cover through mechanical means is a phenomenon that generally follows some compressive crushing of the concrete in the region. Compressive crushing generally occurs in the post yielding (or plastic) behaviour of the material and is due

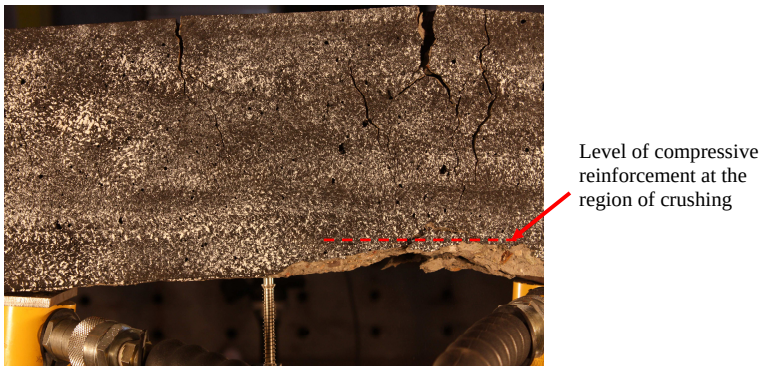

Figure 4.26: Photo: Demonstrates the location and magnitude of the loss of the compressive cover due to excessive crushing. Obtained from beams tested in Chapter 3.

to build up of excessive compressive strains. With this in mind, the criterion to be used for the loss of cover due to compression is defined in terms of the build up of plastic compressive strains. The following illustrates the method undertaken in calculating the plastic strain magnitude required to cause the loss of cover and was achieved through experimental means.

The DIC images of the beams investigated in Chapter 3 were used for the calculation of the plastic strains required to cause crushing and cover loss. However, instead of the focusing on the tensile surface within the post analysis of the images, as done in Chapter 3, the focus was changed to the compressive surface of the beams. Fig. 4.26 illustrates that compressive crushing and loss of cover occurred within the beams.

From the post analysis of the images and correlation with the load-deflection data it is possible to calculate the relationship between the load applied and the compressive strains that develop within the concrete cover. This relationship is plotted in Fig. 4.27. From this plot, the elastic range can be identified as being between the strains of zero to -0.0012, after which the concrete enters its plastic range in compression. By subtracting the elastic strain from the data, the build up of plastic strain can easily be calculated. As noted in Chapter 3, it is difficult to define points in the post yielding behaviour in

terms of load applied, therefore the calculated plastic strains are plotted against the mid-span deflection. Fig. 4.28 illustrates both load versus mid-span deflection and plastic compressive strain of the compressive surface versus mid-span deflection for the beams. From this plot it is clear that the plastic strains rapidly increase at a value of -0.00415, indicating the occurrence of the loss of cover.

In must be noted that the strains developed within this experimental set up are axial strains and therefore can be considered to be equal to the equivalent strains. As a result, for the purposes of numerical modelling, the criterion for determining the loss of cover is defined as the point at which the equivalent plastic strains exceed a value of -0.00415. However, as the criterion used to define the loss of cover within this investigation was obtained from purely mechanical testing at ambient temperatures, the accuracy of the criterion used may not be as effective throughout the thermal phase. Therefore, to increase the accuracy of this method, further experimental data would be required to determine the equivalent compressive plastic strain to cause loss of cover in a range of concrete strengths, different concrete cover depths and under increasing temperatures.

To avoid numerical instabilities, the loss of concrete is simulated to occur over a strain range of 0.0001 (i.e. at ambient, this strain range is from 0.00405 to 0.00415 in compression). As the compressive strains calculated for this method were obtained from a test done at ambient temperatures, the values were then extrapolated for higher temperatures which was achieved through a very simplistic method. At ambient, the strain at ultimate strength of the concrete was subtracted from the crushing strain which was calculated (0.00415) in order to obtain a "strain difference". This "strain difference" was then added to the strain at ultimate strength for higher temperatures in order to simplistically determine the strain at which the loss of concrete cover occurs at these higher temperatures.

To further avoid numerical localisation issues, it was assumed that when the user defined limit was reached, that the full depth of the cover was removed within the compressively damaged section. Furthermore, it should be noted that due to the nature

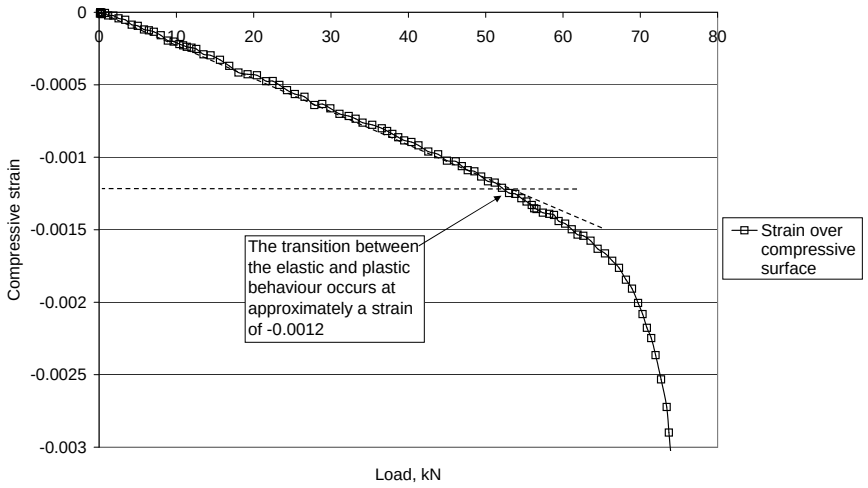

Figure 4.27: Plot illustrating the compressive strain at compressive reinforcement level versus applied load. The strains were measured within the mid-span of a beam and the beam was placed under four-point bending. Results obtained from beams tested in Chapter 3.

of the material application within a numerical model, this method can only be used within solid modelling. This is further discussed in Appendix H.

The full material input data including the subroutine can be found in Appendix I

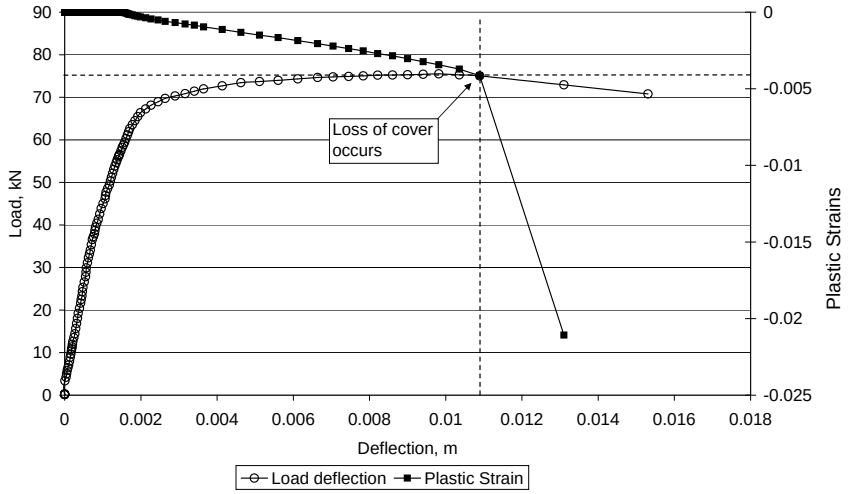

Figure 4.28: Plot showing the relationship of plastic strain build up at the compression reinforcement level versus the mid-span deflection (left axis). Plastic strains are calculated from the data in Fig. 4.27. The applied load versus mid-span deflection is also shown (right axis) to illustrate that this phenomena occurs well into the plastic region of the beam behaviour. Results obtained from beams tested in Chapter 3.

4.5 Application of the new technique for concrete cover loss

This application is to show how the use of the new technique manifests itself within a numerical simulation and what effects it has on the thermo-mechanical behaviour of a reinforced concrete frame.

4.5.1 Additional Applied Loading

In addition to the the vertical mechanical static loading and thermal loading as defined previously, the frame was subjected to a horizontal mechanical cyclic displacements at the level of the beam. This horizontal cyclic motion was applied after the vertical mechanical load but before the thermal loading with the aim to induce some compressive damage to the concrete and simulate the partial loss of cover. Further to this, and to insure the stability of the simulation, the horizontal load is applied as a deflection

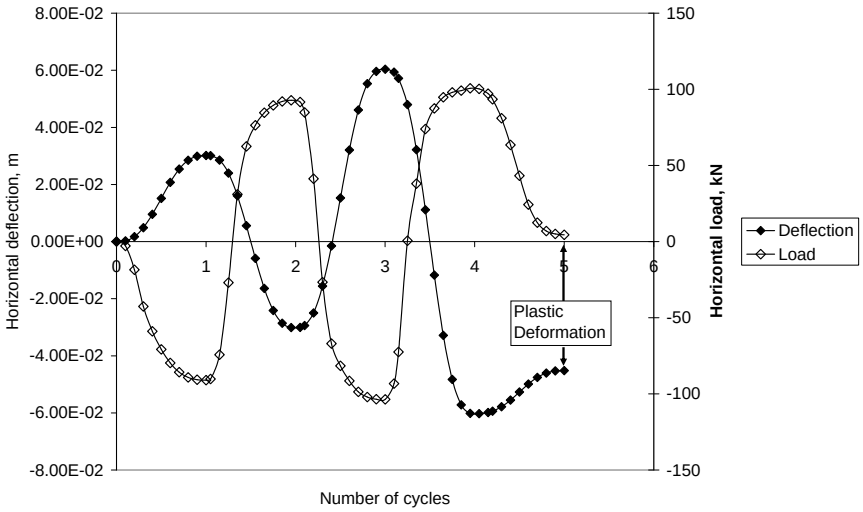

Figure 4.29: Additional horizontal loading (displacement controlled) applied to the portal frame at beam level. The load or base shear relationship is also given to demonstrate that permanent deformations that occur when load is completely removed.

controlled loading as illustrated in Fig. 4.29. It should be noted that although the load reduces to zero at the end of the cycles, due to the plastic deformations that are incurred, the horizontal deflection does not reduce to zero but instead has an initial deflection (at beam level) of approximately 0.045m.

4.5.2 Damaged scenarios using subroutine

The use of the subroutine is used to determine the loss of cover when the frame is subjected to extreme loadings. The criterion used to determine the plastic strain at which the concrete becomes crushed and removed is based on a purely mechanical test at ambient temperature. Therefore, it can not be used throughout the thermal phase with great certainty. As a result, the scenarios analysised and compared below are:

(a) an undamaged frame (i.e. no use of the subroutine), therefore the concrete remains intact throughout the full analysis,

(b) a damaged frame where the subroutine is used throughout both the mechanical

loading and thermal loading, therefore the concrete cover loss is calculated and taken account of, and

(c) a damaged frame where the subroutine is used during only the mechanical loading and not through the thermal loading, therefore the concrete cover loss is calculated and taken account of only in the mechanical loading phase.

It should be noted that scenario (b) and (c) are identical within the mechanical loading phase and only differ within the thermal phase. Therefore, there is only two mechanical loading scenarios reported upon whereas there are three thermal loading scenarios.

4.6 Results and Discussion

Fig. 4.30 shows the horizontal load-deflection relationship for both scenarios (i.e cover left intact and cover damage simulated). It can be seen that both relationships are almost identical throughout the full mechanical loading phase with a maximum load of 100kN and a final horizontal plastic displacement of -0.045m (from vertical). This shows that the use of subroutine does not affect the mechanical properties of the concrete under ambient temperatures.

As the thermal load as defined in Fig. 4.5 is applied, the differences begin to become apparent. The thermal profiles shown in Fig. 4.31 to 4.33 demonstrate how the simulation of the loss of cover affects the thermal propagation throughout the frame. When no cover loss is considered (Fig. 4.31), the thermal front propagates through the concrete an a uniform rate. However, when the loss of cover is simulated during the analysis (Fig. 4.32 and Fig. 4.33) the thermal front does not propagate through the concrete uniformly. Instead, the rate of thermal propagation through the regions of cover loss is much greater than in the regions where the concrete cover has remained intact.

It can be seen for the variations in thermal propagation, with particular reference to (Fig. 4.33(a)), that loss of cover at the end of the mechanical cyclic loading is

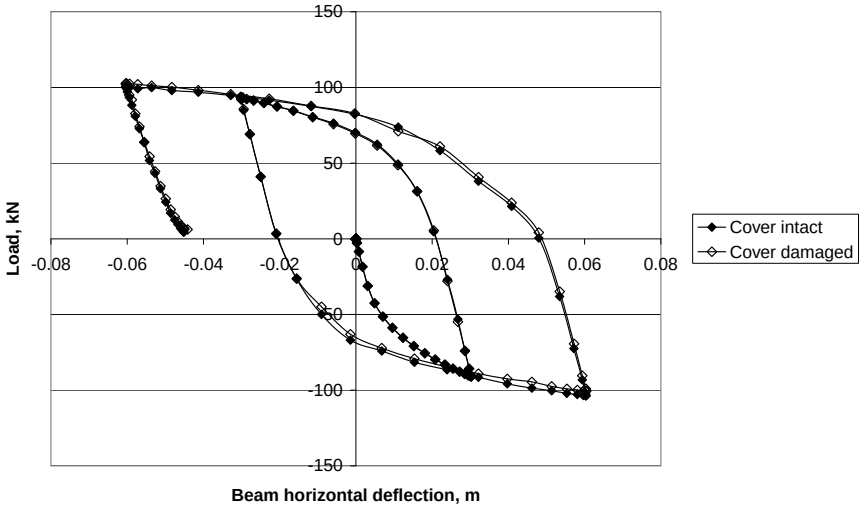

Figure 4.30: Plot showing the cyclic load-deflection relationship of the portal frame subjected to the additional horizontal loading. A comparison is made between the simulations where concrete cover is considered to remain intact and where concrete cover is considered to be susceptible to removal.

localised at the base of the right column. As the thermal load is applied, a comparison between Fig. 4.32(a) and Fig. 4.33(a) shows how the use of the subroutine can affect the structure within the thermal phase. The magnitude of cover lost from the frame obviously does not change when considering scenario iii), however, when considering scenario ii) the cover at the base of the left column becomes removed within the first five minutes of heating and continues to grow over the heating phase of the thermal load.

Again, during the cooling phase of the thermal load (i.e 3600 seconds to 7200 seconds) differences can be seen between the scenarios. When the simulation of cover loss is considered throughout the thermal loading, from Fig. 4.32(c) it can be seen that the cover on the underside of be beam at both connections becomes removed.

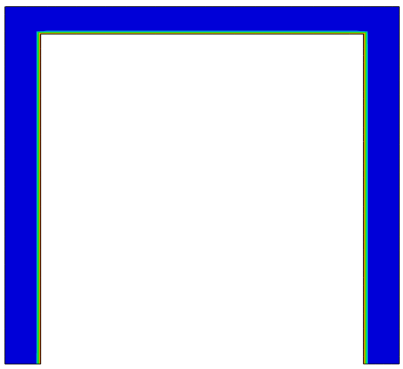

(a) Undamaged frame (300 seconds)

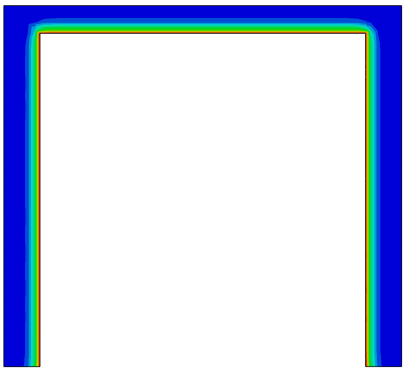

(b) Undamaged frame (3600 seconds)

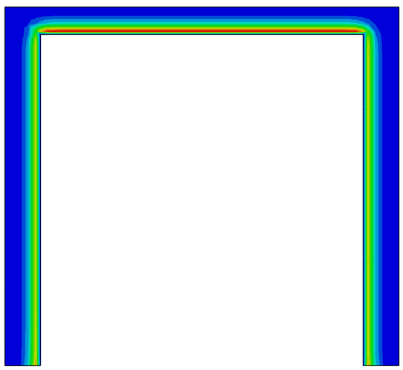

(c) Undamaged frame (3900 seconds)

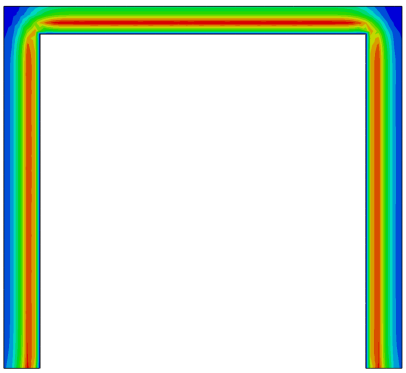

(d) Undamaged frame (7200 seconds)

Figure 4.31: Illustrations showing the thermal profiles of the frame where no cover loss is simulated. The heat transfer is uniform throughout all sections.

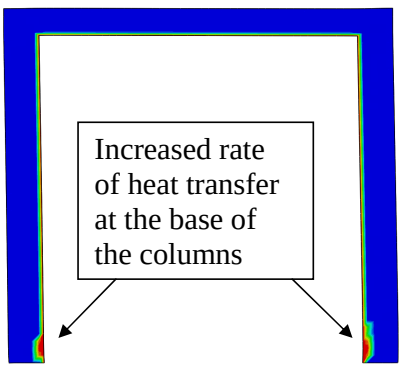

(a) Cover loss simulated throughout (300 seconds)

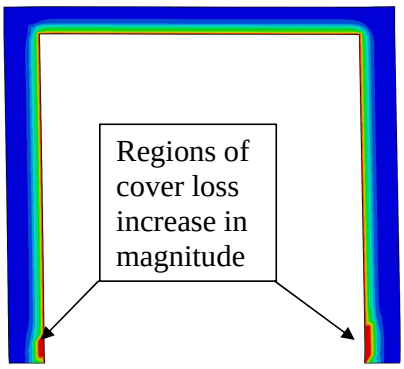

(b) Cover loss simulated throughout (3600 seconds)

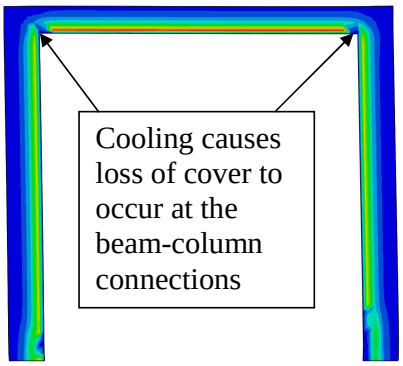

(c) Cover loss simulated throughout (3900 seconds)

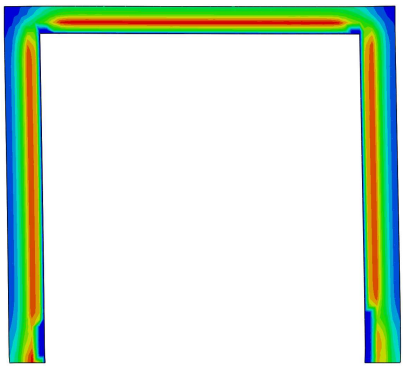

(d) Cover loss simulated throughout (7200 seconds)

Figure 4.32: Illustrations showing the thermal profiles of the frame where cover loss is simulated throughout the mechanical and thermal phases. The heat transfer is not uniform and continuously changes throughout the thermal phase.

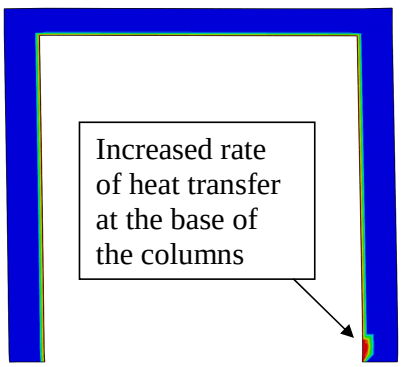

(a) Cover loss simulated in mechanical phase only (300 seconds)

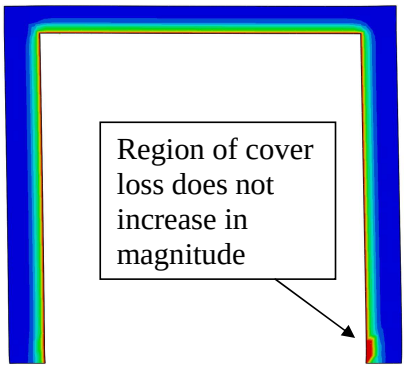

(b) Cover loss simulated in mechanical phase only (3600 seconds)

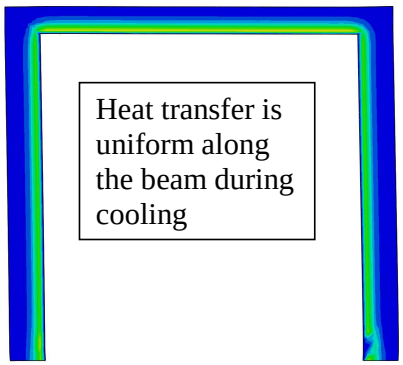

(c) Cover loss simulated in mechanical phase only (3900 seconds)

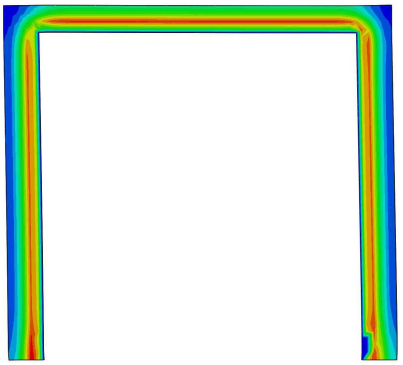

(d) Cover loss simulated in mechanical phase only (7200 seconds)

Figure 4.33: Illustrations showing the thermal profiles of the frame where cover loss is simulated throughout the mechanical phase only. The heat transfer is not uniform but remains constant throughout the thermal phase.

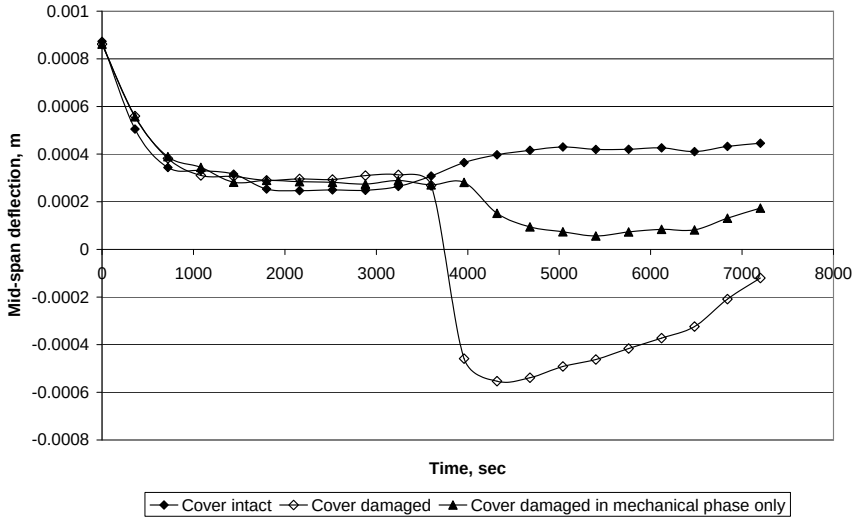

Figure 4.34: Plot showing the mid-span beam deflection of the portal frame when automatic calculation of the concrete cover loss is used, subjected to the thermal loading defined in Fig. 4.5. A comparison between the three simulation types as defined in Section 4.5.2.

Fig. 4.34 shows how the mid-span deflection of the beam reacts when subjected to the thermal load defined in Fig. 4.5 and demonstrates how modelling the loss of concrete cover significantly affects the global behaviour. It can be seen that during the heating phase of the thermal loading, there is not a significant difference in the behaviour of the beam. This is due to the "damage" being localised on the base of the columns and as a result not significantly affecting the behaviour of the beam. This has been previously explained in the section 4.3.3 of this chapter. However, as the frames enter the cooling phase, the cover loss at the beam-column connections as seen in Fig. 4.32(c) results in large variations in the behaviour of the mid-span deflection where the frame with simulated cover loss deflects rapidly downwards in comparison to the the "intact" frame.

4.7 Conclusions

This chapter numerically investigated the loss of concrete cover through mechanical means and the resulting effect on the thermo-mechanical behaviour to a subsequent thermal load. It has been shown that a small amount of cover loss can result in a large variation in thermo-mechanical response of a reinforced concrete structure. As shown in Fig. 4.20 and Fig. 4.22, the largest variation in thermo-mechanical behaviour occurs when the loss of cover is located around the beam-column connection. This is due to a reduction in rotational stiffness of the connection leading to a more flexible structure and as a result, the addition of a thermal load on the structure can cause a large variations, resulting in unpredictable behaviour.

Furthermore, the modelling of the loss of cover through the use of a user defined subroutine, which addresses the problems specified in Section 4.4.1, has been explained. The adoption of this automatic damage calculation method through the use of a subroutine is extremely beneficial and allows the user to apply a variety of mechanical loading scenarios with a subsequent variety of thermal loads without having to manually remove elements or manually alter the material properties to simulate the loss of concrete cover. This method allows the loss of concrete cover to be calculated and applied to the simulation without increasing the DoF's, resulting in a much quicker computational run time. However, as the criterion used to define the loss of cover within this investigation was obtained from purely mechanical testing at ambient temperatures, the accuracy of the criterion used may not be as effective throughout the thermal phase. Therefore, to increase the accuracy of this method, further experimental data would be required to determine the equivalent compressive plastic strain to cause loss of cover in a range of concrete strengths, different concrete cover depths and under increasing temperatures.

Chapter 5

Case Study: Global modelling of a reinforced concrete structure under multiple extreme loading

5.1 Introduction

In this chapter a case study is presented. It was set up in the form of a "blind-study' where the numerical analysis was carried out separately from any knowledge of the results of the experimental study. The study included the input and expertise from many universities and institutions from around the world, including the University of Edinburgh, Indian Institute of Technology Roorkee, Indian Institute of Science and Heriot-Watt University. The design of the test frame was a combined effort by the Indian Institute of Technology Roorkee and the University of Edinburgh. The experimental study was carried out at the Indian Institute of Technology Roorkee while the majority of the numerical studies were carried out at the University of Edinburgh.

The plan for the experimental study was comprised of a series of reinforced concrete test frames that were to be mechanically tested in a horizontal, single plane cyclic motion followed by subjection to a pool fire and the behaviour monitored and recorded.

This was done with the aim of determining the thermo-mechanical effect a thermal load has on a pre-damaged reinforced concrete frame. This was achieved by measuring and recording the thermal and structural behaviour of the frame which included applied

forces, displacements, thermal profiles throughout all the members and the gas phase temperatures.

This chapter presents the available results ascertained from the experimental study and a comparison with a number of numerical simulations of the test frame that incorporates the knowledge obtained from the previous chapters.

It should be noted that the experimental study is still ongoing, and as a result, some experimental data is not presently available. Furthermore, the data obtained from the experimental aspect of the study, due to unforeseen circumstances, has been limited to the cyclic load deflection relationship in the horizontal direction within the mechanical phase, maximum vertical mid-slab deflection obtained within the heating phase of the thermal load, some thermal profiles of some sections and photographic evidence after completion of the test. As a result the validation of the numerical model is limited to the parameters stated above.

5.1.1 Objective

The main objective of this study was to examine the behaviour of a full scale damaged reinforced concrete frame under fire conditions and to determine whether it was possible to numerically model this behaviour within reasonable accuracy and efficiency. This main objective can be broken down into smaller, more defined objectives. A comparison between the measured and the calculated results of the following was made;

(a) "horizontal load deflection relationship" of the frame when subjected to a horizontal loading at upper slab level,

(b) locations and magnitude of damage in the form of loss of cover,

(c) thermal profile through the beams and slab and,

(d) behaviour in terms of mid-slab deflection and storey drift when subjected to the thermal load.

Table 5.1: Loading cases to be performed for the investigation into the thermo-mechanical response of a full scale reinforced concrete frame.

Case	Simulated seismic load	Fire load	Experimentally completed	Numerically simulated
1	Displacement beyond peak lateral force	900^oC - 1000^oC for 1 hour	Yes	Yes
2	None	900^oC - 1000^oC for 1 hour	No	Yes

However, as stated above the level of validation is limited due to unforseen curcumstances.

5.1.2 Scope

The experimental plan comprised of a number of identical reinforced concrete frames as detailed in Fig. 5.1 to Fig. 5.4 subjected to quasi-static cyclic and thermal loading as shown in Table 5.1. Both the applied mechanical and thermal loading are further explained and described in Section 5.2.2. However, it should be noted that, as the experimental study is still ongoing, not all the cases have been experimentally completed.

The design of the reinforced concrete frame, the loads and deflections applied and the locations of the instrumentation were all determined by a collaborative effort between the Indian Institute of Technology Roorkee and the University of Edinburgh.

5.2 Experimental project design

This section presents a detailed description of the final design of the built test frame. The loading scenarios and magnitudes for both the mechanical and thermal phases are discussed as well as the type and placement of the instrumentation used.

5.2.1 Frame details

The reinforced concrete structure and test frame were designed to the following details and dimensions and are illustrated in Fig. 5.1 to Fig. 5.4.

Dimensions of the building:-

A four storey (G+3) reinforced concrete building of plan dimensions 9m by 12m, located in seismic zone IV on medium soil was considered (Standard 2002). Building element details were as follows:

(i) Column: 300 x 300mm

(ii) Beam: 230 x 230mm

(iii) Slab: 120mm thick.

General:-

Other related data were designed as follows:

(i) Grade of concrete: - M30 (i.e. ambient compressive strength of 30MPa)

(ii) Grade of steel : - Fe415 (i.e. ambient yield strength of 415MPa)

(iii) Floor finish: - 1 kN/m^2

(iv) Live/ imposed load: - 2kN/m^2

(v) Density of concrete: - 25kN/m^2 (assumed)

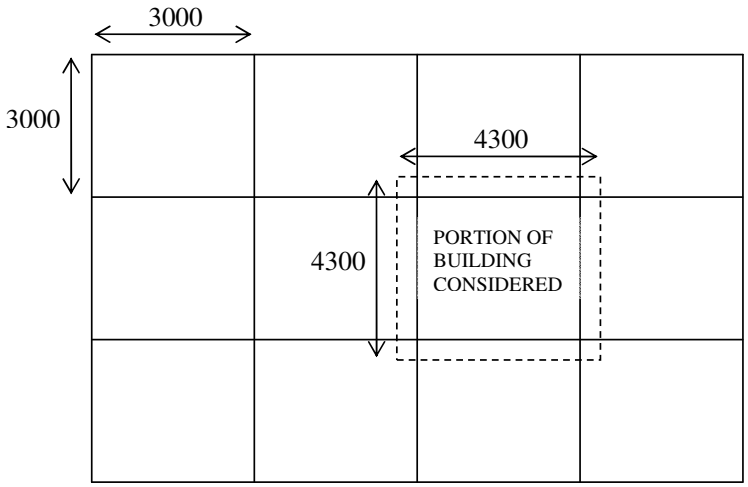

Plan of Building

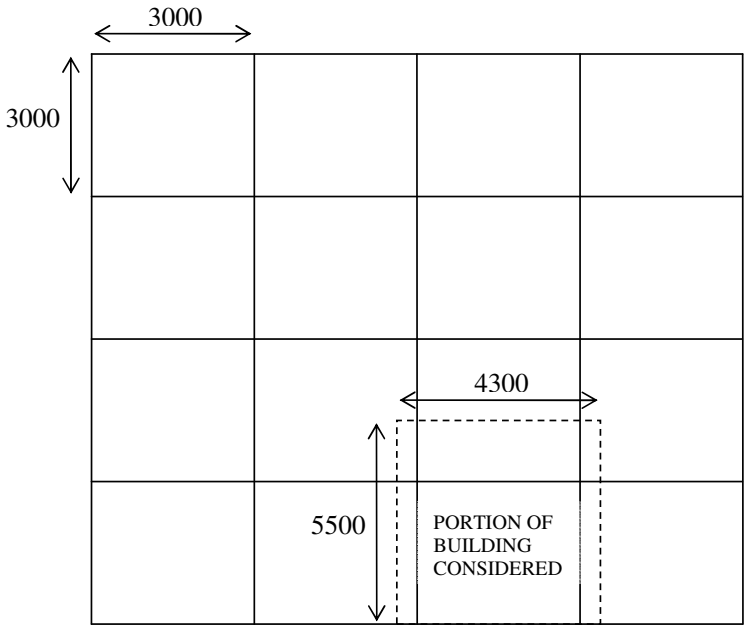

Elevation of Building

Figure 5.1: General layout of the full building used for the experimental and numerical analysis for the investigation into the thermo-mechanical response of a full scale reinforced concrete frame. The plan and elevation is given with a bordered segment illustrating the portion of the building to be analysed.

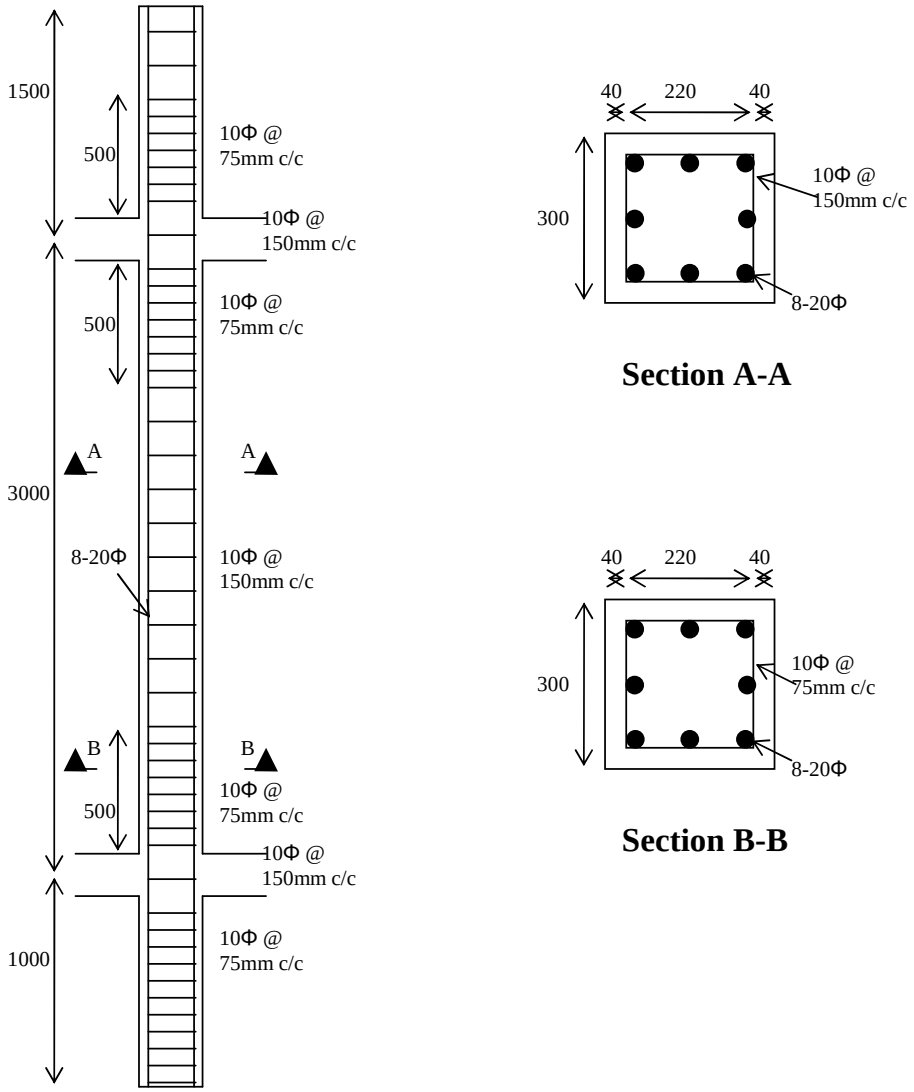

Figure 5.2: Geometrical details of the concrete column and column reinforcement of the test frame used for the experimental and numerical analysis for the investigation into the thermo-mechanical response of a full scale reinforced concrete frame.

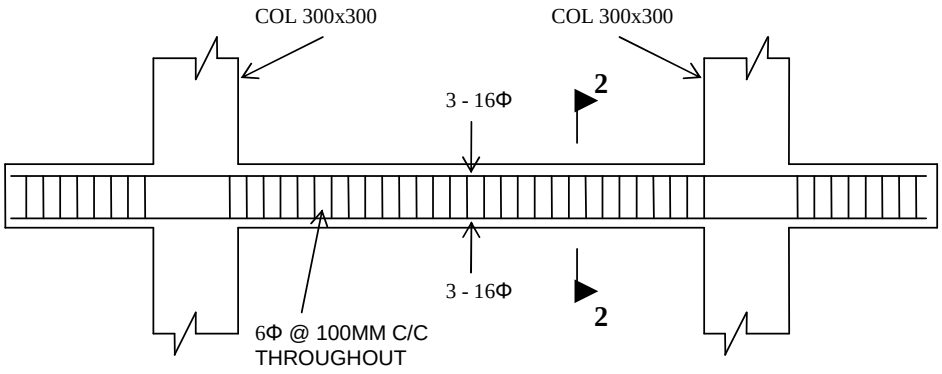

L – Section of Beam (230 x 230)

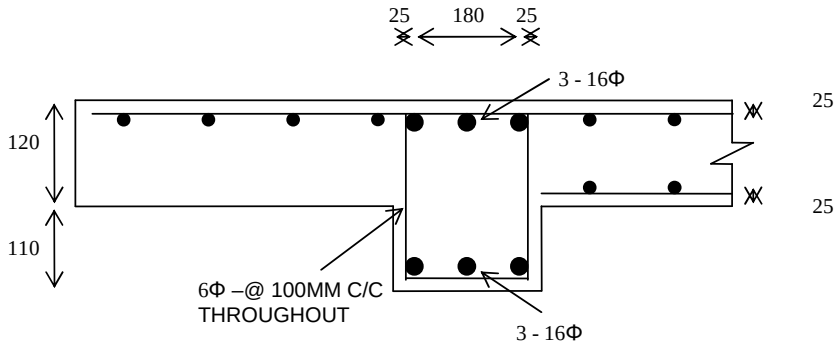

Section 2-2

Figure 5.3: Geometrical details of the concrete beam and beam reinforcement of the test frame used for the experimental and numerical analysis for the investigation into the thermo-mechanical response of a full scale reinforced concrete frame.

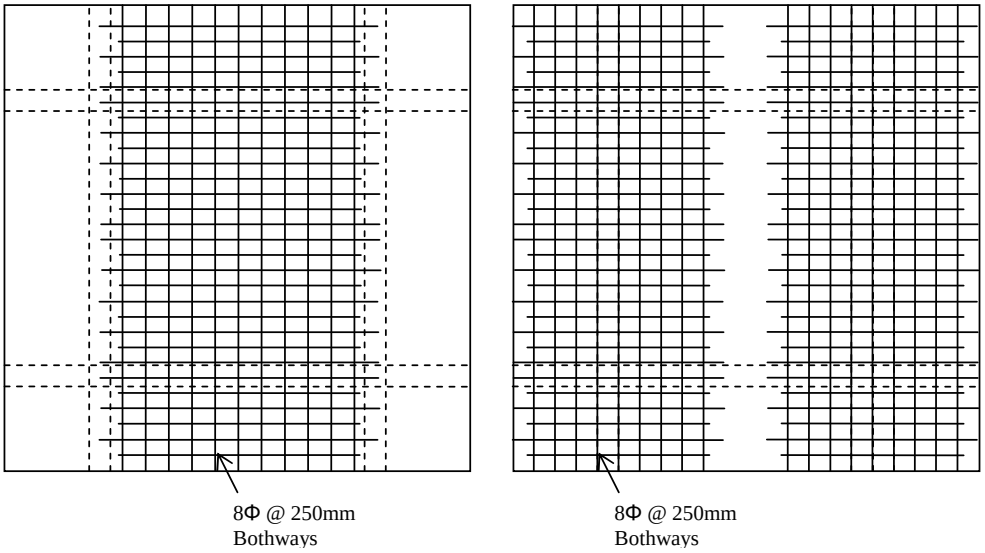

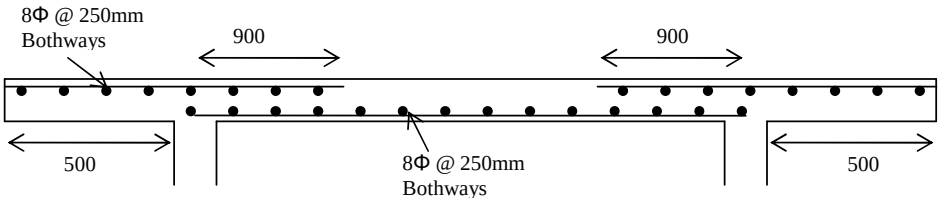

Section through slab

Figure 5.4: Geometrical details of the concrete slab and slab reinforcement of the test frame used for the experimental and numerical analysis for the investigation into the thermo-mechanical response of a full scale reinforced concrete frame.

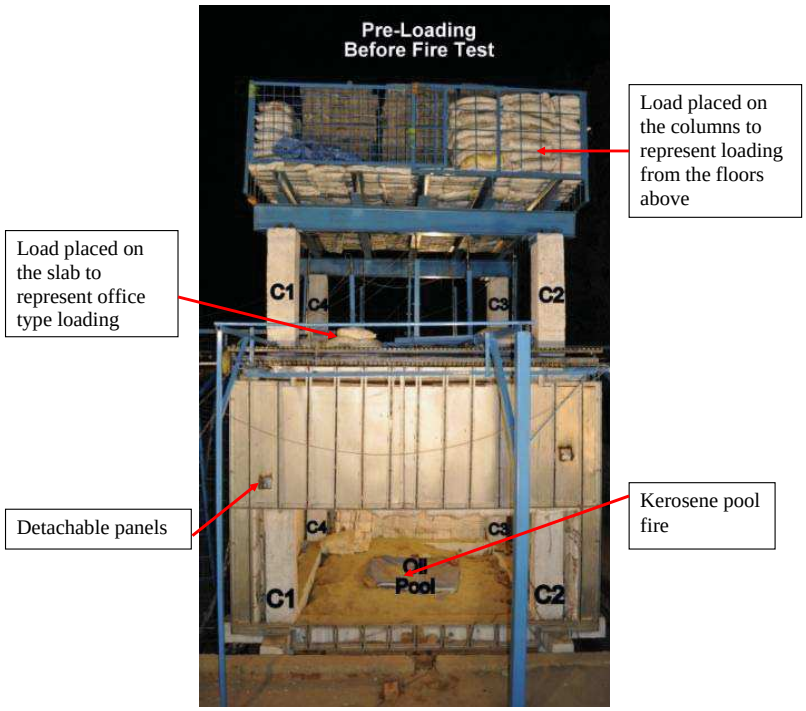

Figure 5.5: Photo: Illustrates the placement og the vertical loading arrangement, detachable panels and the kerosene pool fire. This photo has been obtained from the Indian Institute of Technology Roorkee.

5.2.2 Applied loading

The frame was subjected to a multitude of loads. The first being the vertically applied static loading placed on the slab and on the column tops to represent the typical loads in an office building and simulate the loads from the floors above respectively. These loads were placed in the form of uniformly distributed sand bags as shown in Fig. 5.5. The load applied to the slab was 3kN/m^2 while the load applied to the column tops was 2143kN/m^2. Full calculation of these loadings can be found in Appendix J.

In addition to the vertical mechanical loading, the frame was subjected to a horizontal mechanical cyclic loading at the level of the slab. This horizontal cyclic motion was applied after the vertical mechanical load but before the thermal loading with the aim to induce some damage to the concrete test frame. This horizontal loading was

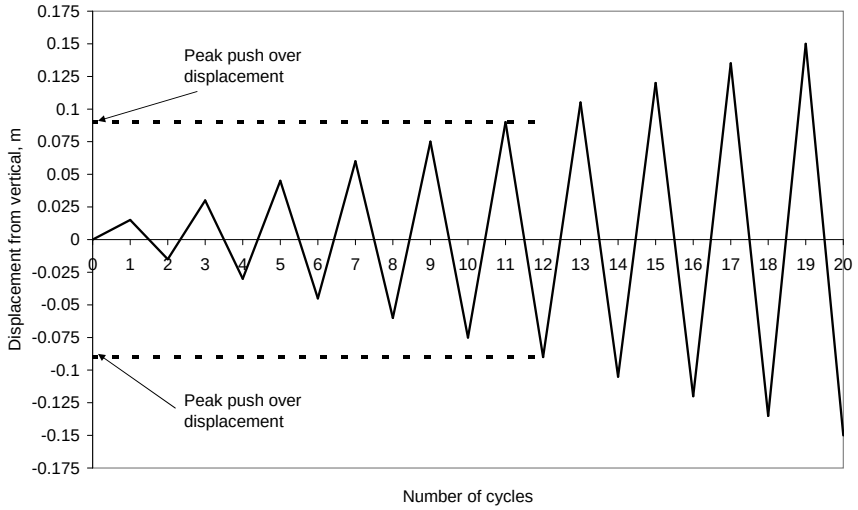

Figure 5.6: Plot showing the experimental horizontal displacement cycle pattern. Illustrated is the peak push over displacement that was applied to the frame and further explained in Section 5.4.1.

applied using displacement controlled parameters as defined in Fig. 5.6. The displacement to peak lateral load was calculated through a push over analysis using ABAQUS, which is described later in Section 5.4.1. After the specified maximum displacement was achieved, the horizontal load was then completely removed and the frame was allowed to settle before the sides of the frame were covered using easily attachable/detachable panels and the pool fire ignited (see Fig. 5.5).

The epicentre of the pool fire was situated at the center of the four columns and at the height of the lower beam. The chosen configuration, which is studied in greater detail in the section below, was designed to achieve flashover within 5 minutes of ignition, reaching gas temperatures of 900^{o}C to 1000^{o}C and to last for 1 hour before cooling naturally.

5.2.3 Pre-testing experimental pool fire study

To ensure that the pool fire could provide the necessary temperatures, the initial rate of increase and be able to remain at the maximum temperature for the duration of an

hour, the fuel mixture and flow rate needs to be calculated. This process was calculated by Dr. Jose Torero from the University of Edinburgh and is discussed below.

The main aim of this pre-testing experimental pool fire study was to determine the best configuration to maintain temperatures within the compartment at an average of 900^{o}C to 1000^{o}C for a period of 1 hour and to reach a steady state as fast as possible. It was decided that a 1m x 1m kerosene pool fire was to be used. This would allow very rapid flame spread over its surface and flashover to be reached in less than 5 minutes.

To reduce the time to flashover it is important to allow rapid accumulation of smoke, and thus it was better to make the ventilation opening as low as possible as to allow the smoke to be accumulated and heat up the structure rapidly leading to flashover. Therefore, the fire was continuously fed by the 1m x 1m pool fire and a 1m high ventilation opening that spanned the length of one side of the structure (i.e. 3m). To maintain post flashover and the required temperatures, a burning rate of 0.177kg/m^{2}s was required which in turn required a flow rate of 1.43x10^{-4}m^3/s.

The gas temperatures within the compartment were measured using thermocouples placed at different heights (i.e. 0.2m, 0.9m, 1.6m and 2.9m from the level of the pool fire). Fig. 5.7 illustrates the temperature profile achieved within the compartment. It can be seen that the temperature rose very rapidly within the first 3 minutes before stabilising at approximately 900^{o}C. As the experiment continued (beyond 10 minutes), the temperatures increased slightly and re-stabilise at approximately 950^{o}C.

In summary, the configuration described above provided the experiment with;

(a) A fire that rapidly reached flashover and its approximate maximum temperature within 5 minutes, and

(b) A fire where temperatures of 900^{o}C to 1000^{o}C were sustained for the required period of time.

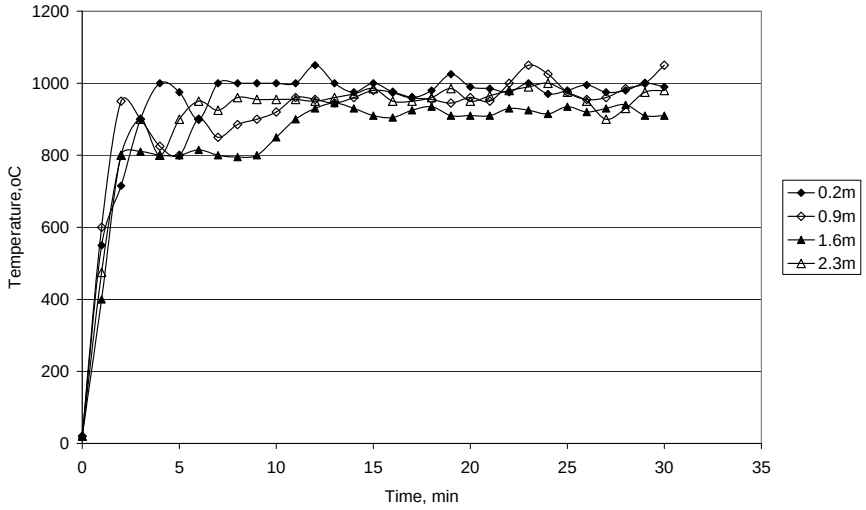

Figure 5.7: Plot showing the gas temperature profiles of the pre-testing experimental pool fire study. Temperatures were taken at heights of 0.2m, 0.9m, 1.6m and 2.3m within the compartment.

5.2.4 Instrumentation

As the behaviour of the frame and the surrounding conditions is extremely complicated, the frame was therefore heavily instrumented with LVDT's (linear variable differential transformer), stain gauges, thermocouples throughout the concrete members and within the compartment and thermal flux meters. Full details of their locations is given in Fig. 5.8 to Fig. 5.9. In addition to this, the loading jack used was able to provide an output of the load and displacement that was applied to the frame.

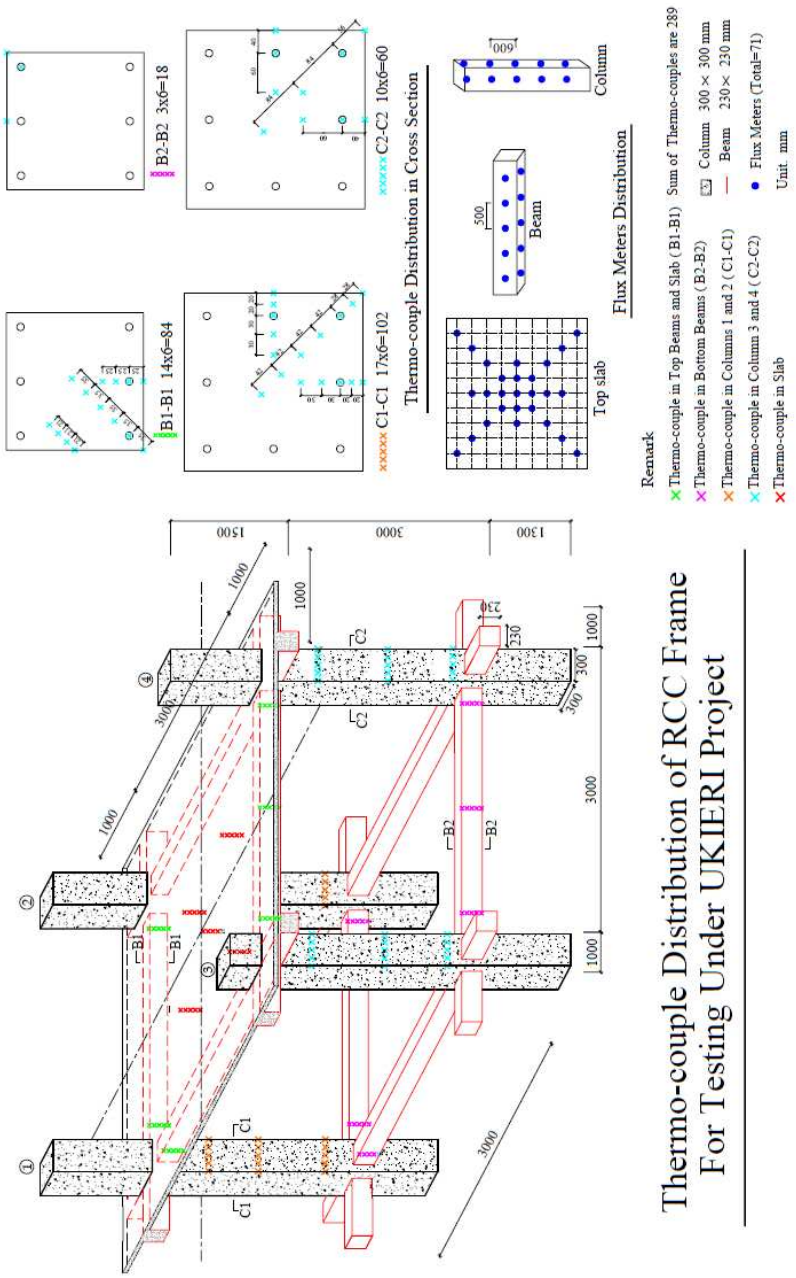

Figure 5.8: Schematic of the placement of the thermocouples embedded in the concrete test frame. Drawn and provided by the University of Edinburgh.

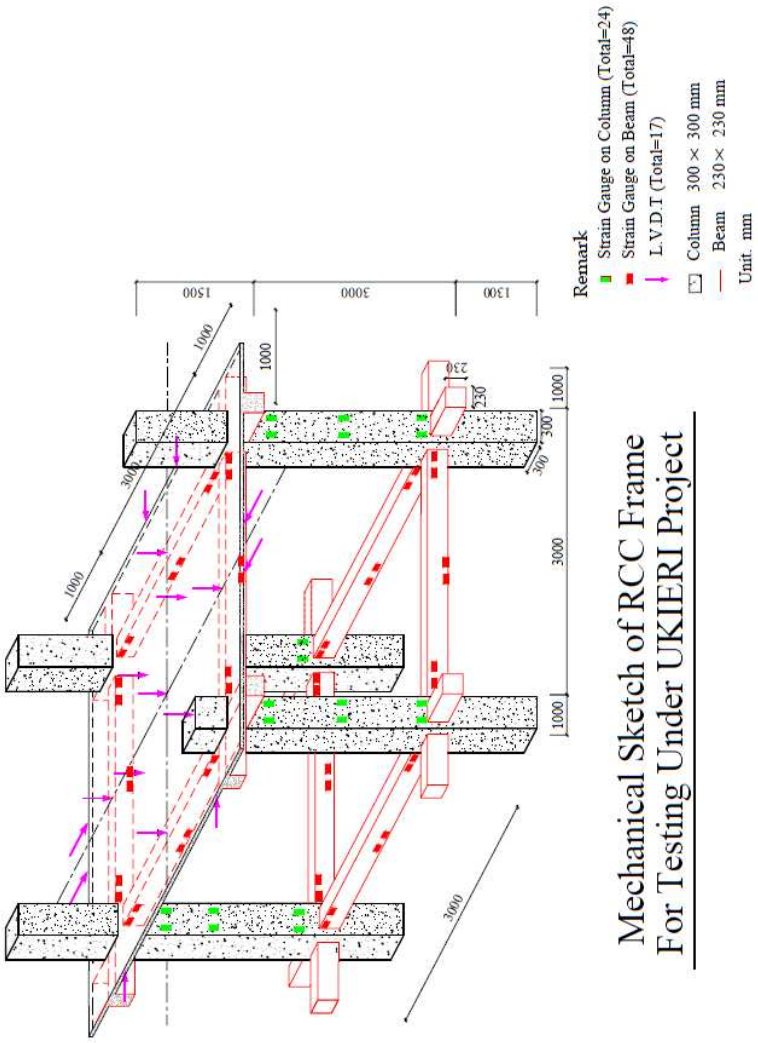

Figure 5.9: Schematic of the placement of the displacement and strain gauges around the test frame. Drawn and provided by the University of Edinburgh.

5.3 Computational modelling of test frame

This section outlines the details of the numerical model of the experimental frame. The loading scenarios and magnitudes for both the mechanical and thermal phases are discussed as well as the material properties and model types. Similar to Chapter 4, the numerical results reported upon in this chapter were created and analysed using the computer modelling software, ABAQUS.

5.3.1 Model description

In this chapter many numerical models were built to perform a variety of analyses and to simulate a variety of applied mechanical and thermal loadings.

The numerical structure used to determine the behaviour of the reinforced concrete structure was, unless otherwise stated, modelled to simulate the geometry, materials and loading applied in the experimental frame detailed above. However, small alterations were made to simplify the problem and reduce the analysis time. These simplifications can clearly be seen in Fig. 5.10 and included:

(a) the columns stopped at the level of the slab to reduce the number of elements to be calculated, and

(b) symmetry was utilised to simplify the problem and reduce the analysis time by half.

To simulate the behaviour of the reinforced concrete structure for a push over analysis and a full cyclic loading along with the thermo-mechanical behaviour required the model to be carried out in three dimensions. It also required the material properties to include a full plasticity and thermal behaviour for both the concrete and steel. As in Chapter 4, the concrete was modelled using solid elements with reduced integration and the steel was modelled using truss (1D) elements.

The foundations of the portal frame (i.e. the base of the columns) are considered to be completely fixed in both translation and rotation whilst the rest of the frame is

free to deflect and rotate.

5.3.2 Material properties

The ambient material properties for the numerical modelling in this chapter were dictated by the material properties of the corresponding experiment. Both concrete and steel material properties were also assumed to be isotropic, non-linear, temperature dependent and take into account stiffness degradation that will occur through excessive loading. See Chapter 2 and Appendix I for full details. At ambient temperature the steel reinforcement has a yield stress of 415MPa and a Young's modulus of 200x10^{3}MPa and was assumed to be be perfectly elastic-plastic. As the temperature increases the strength reduction occurred in accordance with Eurocode 2 Part 1-2 (2004).

At ambient temperature the maximum stress (f'$_c$) of the concrete is 30MPa at a strain of 0.25% after which it linearly reduces to zero at a strain of 1.0%. Again as the temperature increases the strength reduction occurred in accordance with Eurocode 2 (2004). In addition to these material properties, to simulate the loss of any concrete cover as a result of excessive plastic strains, the automated method as described in Chapter 4 was utilised. Once again, it must be noted that this alteration to the material properties was only applied to the concrete cover and did not continue on into the core of the member as the core was assumed to be held in place by the confinement of the reinforcement cage.

5.3.3 Applied loading

In addition to gravity, the vertical mechanical loads (supplied by the sand bags in the experimental setup) were applied to the slab and column tops as uniformly distributed pressures which continued throughout the full mechanical and thermal analyses.

The horizontal cyclic mechanical loading was applied as a displacement controlled boundary condition placed upon the ends of the slab. Although the magnitude of each of the cyclic motions matched that specified in Fig. 5.6, the path taken for reasons of numerical stability is given in Fig. 5.11. The reduced rate of change of displacement

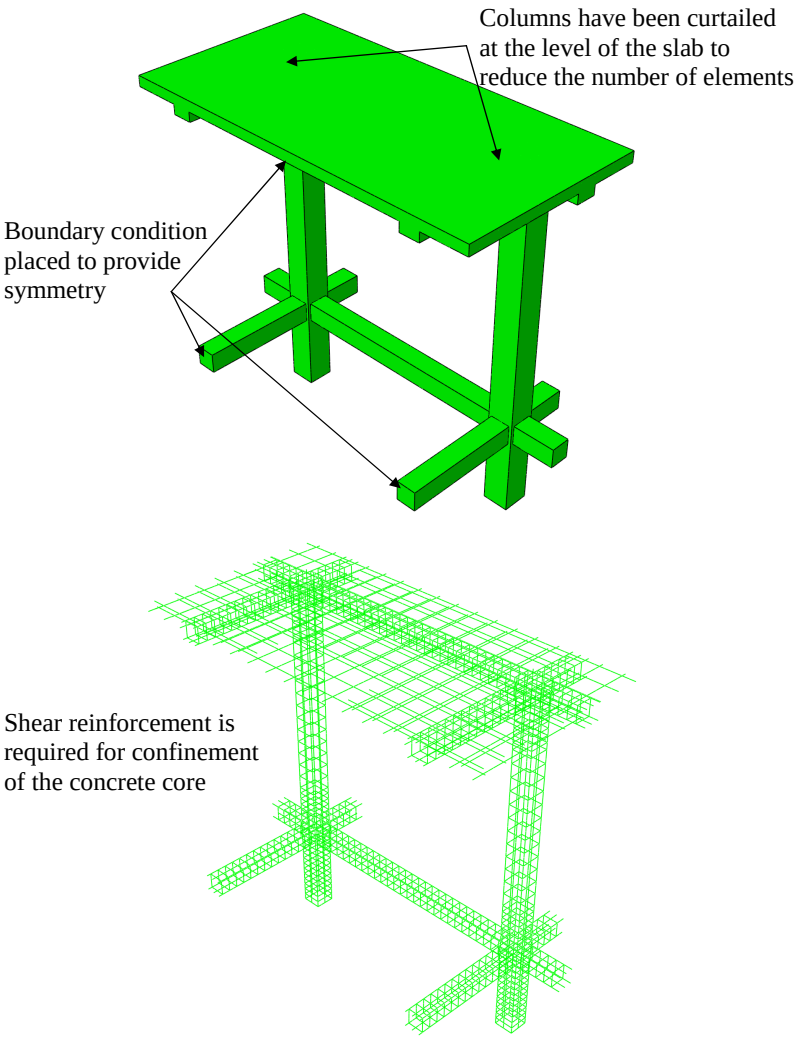

Figure 5.10: Illustration of the numerical model used. Showing how symmetry was implemented, that the columns were curtailed at the level of the slab and that shear reinforcement is included to provide confinement to the concrete core. The steel reinforcement is constrained within the concrete in all DoF's.

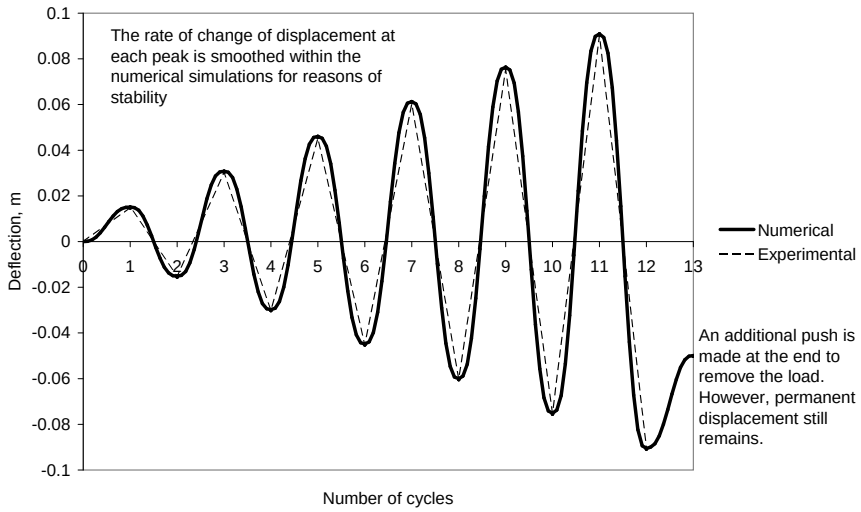

Figure 5.11: Plot showing the number of cycles placed on the frame and their corresponding horizontal slab displacements to be used in numerical simulation. This is graphically compared to the experimental deflection routine with particular reference made to the locations of changing direction. It must be noted that an additional displacement is made to remove the applied load. However, the permanent displacement still remains.

at the locations where the frame was changing direction reduced any dynamic effects and allowed the numerical simulation to become more stable.

The surface temperatures of the concrete frame were calculated based on the gas temperatures obtained from the pool fire study previously described. The specified gas temperature used for this analysis was simplified to be homogeneous within the compartment and to linearly increase from ambient (20^oC) to the maximum temperature of 950^oC in 5 minutes. This maximum temperature remained constant for the remainder of an hour, after which it reduced back to ambient for a further hour (Fig. 5.12). This thermal load was applied to the test frame by convective and radiative heat transfer. The convective mechanism used a convection heat transfer coefficient (h_f) of $25kW/m^2$ which is a typical value for structural fire applications. For radiation purposes, the concrete was assumed to act as a black body with an emissivity of 1 (i.e. an idealised body that perfectly absorbs all electromagnetic wavelengths). This assumption was made on the basis that, as the smoke generated by the pool fire becomes trapped within the

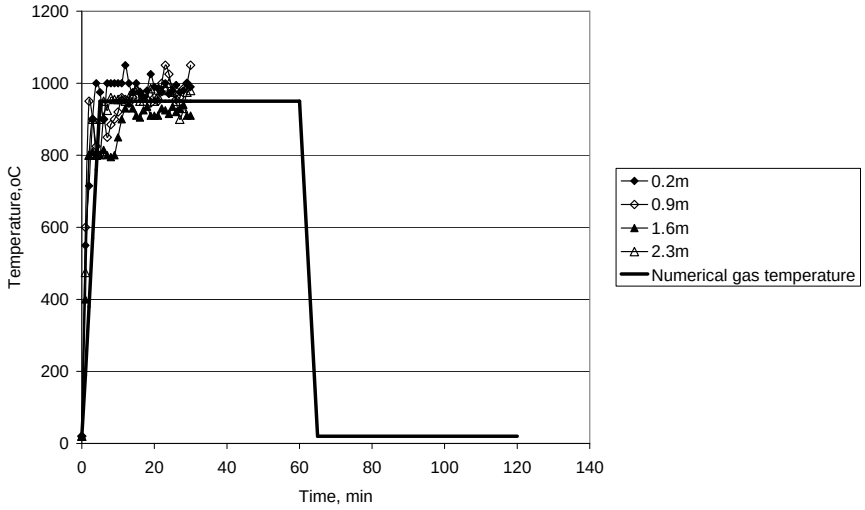

Figure 5.12: Plot showing the gas temperature profile comparison between the experimental and numerical simulation. The numerical gas temperatures rose to the maximum temperature of 950^{o}C within 5 minutes and remained for the remainder of an hour before returning to ambient within 5 minutes.

boundary of the structure and begins to coat the surfaces, the structure will begin to act more and more like a black body.

5.3.3.1 Calculation of surface temperatures

The frame was subjected to a load produced by a kerosene pool fire as detailed in Section 5.2.2. The gas phase temperatures for the numerical analysis were as detailed in Fig. 5.12 and from these gas temperatures, the surface temperatures of the concrete were calculated. Multiple points of the frame were used to calculate an average surface temperature which included measuring temperatures around the heated region of the column mid-heights, the beam mid-spans and the slab mid-span and quarter spans.

When averaged over time, the surface temperature was calculated to be as shown in Fig. 5.13. This showed that the surface temperature did not increase as rapidly as the gas temperatures and, with a maximum temperature of 926^{o}C, did not reach the maximum achieved by the gas (950^{o}C). Furthermore, during the cooling phase, the

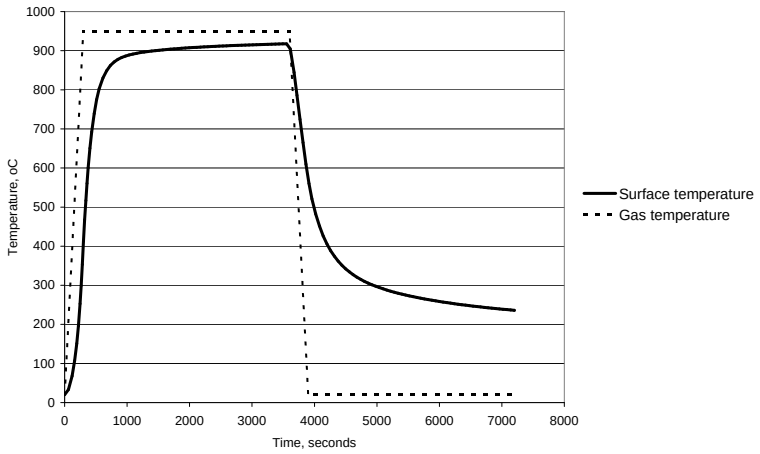

Figure 5.13: Plot illustrating the calculated surface temperature of the frame. The gas phase temperatures are also give as a comparison.

concrete surface also reduced in temperature less rapidly and after a period of one hour of cooling, the surface cooled to approximately 236^{o}C.

5.4 Results and discussion

5.4.1 Push over analysis

A push over analysis, is one where a frame or column is loaded continuously until failure in one direction (horizontal) while the load and deflection is recorded. The purpose for performing this push over analysis was to provide the Indian Institute of Technology Roorkee (i.e. where the experimental programme is being performed) with guildlines of the load deflection relationship so that the appropriate equipment could be obtained to provide the required loading and stroke length. In addition to this, the push over analysis was performed to make sure that the numerical simulation was performing as expected.

In this section, a push over analysis was performed using the finite element software ABAQUS and the model illustrated in Fig. 5.10. The aim was to provide an indication of the peak load that the test frame could support and the corresponding horizontal

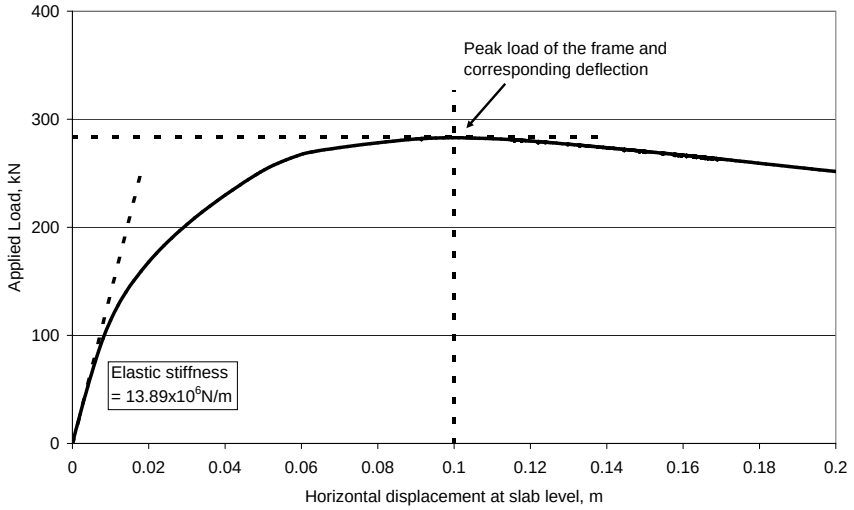

Figure 5.14: Plot showing the load deflection relationship of the test frame in a push over analysis. The maximum load and corresponding horizontal deflection is illustrated. In addition, the initial elastic stiffness of the frame is shown which is used for a comparison with hand calculations.

slab displacement. The frame detailed in Fig. 5.10 was fixed at the column bases and the slab was then pushed with a horizontal displacement of 0.2m. The load applied (or base shear) was then correlated to the horizontal displacement of the slab and plotted in Fig. 5.14.

From Fig. 5.14 it can be seen that the stiffness of the frame within the elastic range was 13.89x10^6N/m while the maximum load reached was approximately 285kN with a corresponding horizontal displacement of 0.1m.

To provide a quick validation to the load deflection behaviour detailed in Fig. 5.14, some simple hand calculations (below) were performed and compared to the stiffness of the frame within the elastic range to determine whether the numerical model was performing as expected.

Three assumptions were made to provide a simplified frame as shown in Fig. 5.15. First, the assumption that the frame consisted of an infinitely stiff beam, second, that the base of the columns were completely fixed and thirdly, that the beam column connection is infinitely stiff. Also, as the members under investigation were reinforced

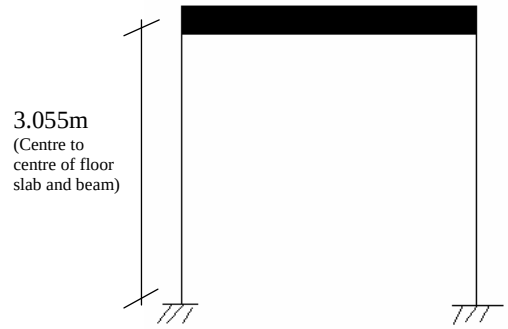

Figure 5.15: Simplified test frame arrangement for use in the hand calculations of the elastic stiffness.

concrete, the combined elastic modulus (E_T) must be calculated.

$$E_T I_T = E_s I_s + E_c I_c \tag{5.1}$$

$$I_s = (2\text{x}(\frac{\pi(0.04)^4}{4})) + (6\text{x}(\frac{\phi(0.04)^4}{4}) + (\pi(0.01)^2(0.11)^2) = 1.57\text{x}10^{-8}\text{m}^4 \tag{5.2}$$

$$I_c = \frac{0.3\text{x}0.3^3}{12} = 6.75\text{x}10^{-8}\text{m}^4 \tag{5.3}$$

$$E_T I_T = ((2.1\text{x}10^{11})\text{x}(1.57\text{x}10^{-8})) + ((1.79\text{x}10^{10})\text{x}(6.75\text{x}10^{-8})) \tag{5.4}$$

$$E_T I_T = 16.89\text{x}10^{6}\text{Nm}^2 \tag{5.5}$$

The stiffness of this structure could then be obtained through the following calculations.

$$K = \frac{12E_T I}{L^3} + \frac{12E_T I}{L^3} \tag{5.6}$$

$$K = 2.(\frac{12\text{x}16.89\text{x}10^{6}}{3.055^3}) \tag{5.7}$$

$$K = 14.21\text{x}10^{6}\text{N/m} \tag{5.8}$$

where “K” is the stiffness and “I” is the second moment of area.

It can be seen that the stiffness calculated through simple hand calculations and that obtained from the numerical analysis, are in close agreement (i.e. only a 4.8% difference). This would suggest that the numerical analysis is performing as expected and, as a result, the frame and the material properties can be used for further analyses.

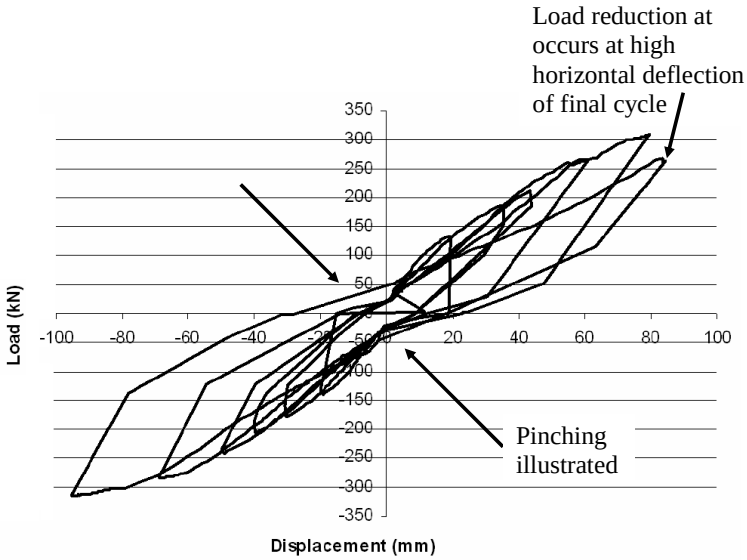

Figure 5.16: Plot showing the experimental load deflection relationship. Illustrating the pinching behaviour.

5.4.2 Experimental mechanical loading of the test frame

In this section, the experimental results for the mechanical horizontal cyclic loading of the test frame are presented. The horizontal deflection was placed upon the frame as illustrated in Fig. 5.6 which produced a load deflection relationship as shown in Fig. 5.16. From this relationship it can be seen that behaviour is roughly symmetrical and the maximum load sustained was approximately ±315kN at a horizontal deflection of ±0.08m from the vertical position. In addition to this the load deflection relationship clear demonstrated "pinching" behaviour which is indicated on the plot.

On the last cycle it should be noted that the maximum load applied to produce the required deflection reduced to 267kN and was only deflected to 0.085m rather than the prescribed 0.09m.

5.4.3 Numerical mechanical loading of the test frame

Fig. 5.17 and Fig. 5.18 illustrates the load deflection relationship obtained from the numerical simulations of the frame subjected to the horizontal loading.

(a) - Fig. 5.17 shows the behaviour of a "traditional" simulation where detailed numerical behaviour was modelled but it was assumed that the concrete cover remained present and intact throughout the analysis, whereas

(b) - Fig. 5.18, in addition to the detailed numerical behaviour, it also included the use of the subroutine as described in Chapter 4 which enabled the direct simulating of the loss of concrete cover.

It should be noted that during the simulations, the "step" time was greatly reduced in comparison to the actual time taken to perform the experiment. This resulted in the data obtained from the simulations oscillating slightly due to dynamic effects. However, these dynamic effects were small enough to be considered negligible.

From both plots, it can clearly be seen that the maximum load sustained throughout both analyses were very similar at ±350kN for the traditional simulation and ±330kN when directly simulating the loss of concrete cover. This was very similar to the maximum load obtained from the experimental data which had a maximum of ±315kN and occurred at approximately the same horizontal slab deflection.

In comparison between Fig. 5.17 and Fig. 5.18 there was a noticeable difference in the applied load at the maximum horizontal deflections (±0.09m). When modelling the structure traditionally, the maximum applied load on the final cycle remained approximately equal to the maximum calculated at the horizontal deflection of (±0.08m). However, when directly simulating the loss of concrete cover, the load applied to produce the required displacement on the final cycle reduced to ±270kN. This reduction in load on the final cycle was also observed from the experimental data (see Fig. 5.16).

The reason for this difference in behaviour can be explained by the way the concrete material behaves in compression when simulating the concrete cover loss. Within the

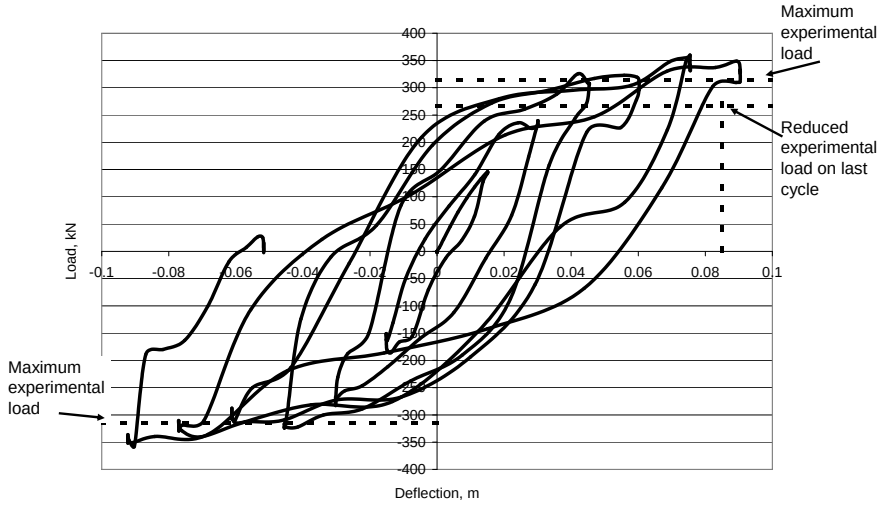

Figure 5.17: Plot showing the numerical load deflection relationship from the cyclic loading where the concrete cover was assumed to remain present throughout the analysis. The maximum load was similar to that from the experimental data but no load reduction was seen on the final cycle and no pinching behaviour was observed.

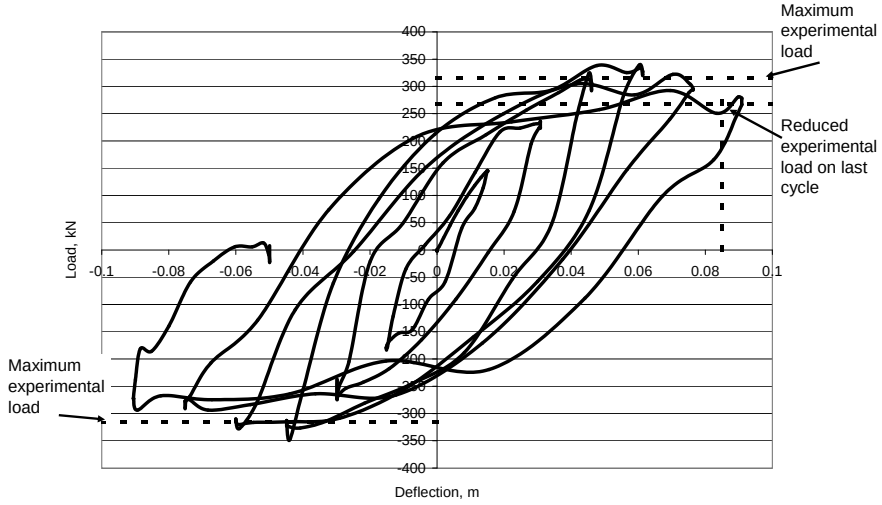

Figure 5.18: Plot showing the numerical load deflection relationship from the cyclic loading where the loss of the concrete cover is directly simulated. The maximum load was similar to that from the experimental data and a reduction was seen on the final cycle but no pinching behaviour was observed.

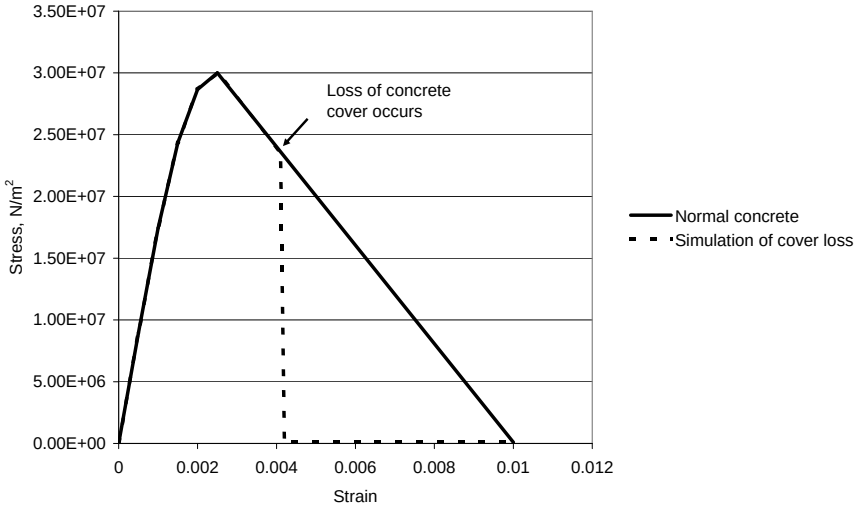

Figure 5.19: Plot illustrating the difference in compression behaviour of the concrete core to the concrete cover. The concrete cover looses strength much more rapidly as an indication that the cover has been lost, and as a result, looses all strength.

traditional simulation, the compressive behaviour of the concrete included softening as shown in Fig. 5.19 where the stress linearly decreases from ultimate stress state to zero at at strain of 1%. On the other hand, when directly simulating the loss of concrete cover, the reduction in compressive strength was much more rapid once the criterion to signify the loss of concrete cover was reached. In this case, the concrete cover looses all compressive stength at a strain of 0.42% (i.e. plastic strain of 0.415%).

Finally, when comparing the experimental results to the numerical simulations it was clear that no pinching occurred within the simulations whereas this phenomenon was a feature of the experimental load deflection relationship (see Fig. 5.16). Contrary to the previous research, as stated in Chapter 2, the pinching phenomenon can be explained in terms of crack formation and closure. This behaviour was not captured within the numerical simulations as the code was unable to capture discrete cracking.

As the frame was horizontally loaded beyond its yielding point and into its plastic region, cracks formed on the tensile face as illustrated in Fig. 5.20(a). After reaching its maximum deflection, the frame was unloaded and returned with an altered elastic

stiffness due to the damage sustained. At this time, there was no load on the frame but the frame has undergone a permanent deformation (Y) as seen in Fig. 5.20(b) and as a result the tensile cracks have not yet closed. The frame was then loaded in the opposite direction to the point where the tensile cracks closed and the frame was in its upright position once again, shown in Fig. 5.20(c). After this the load was continued to be applied, displacing the frame in the opposite direction. At this time, the tensile cracks had fully closed and as a result the elastic stiffness in this direction reverts back to the original stiffness, hence causing the pinching phenomenon as recorded in the experimental data.

This geometrical property of concrete was not captured during numerical simulations, therefore, the pinching phenomenon was not captured. Furthermore, due to the lack of modelling of the pinching behaviour, the horizontal permanent deformations sustained within the simulations (approximately 50mm) were much greater than those recorded during the experiment (approximately 20mm).

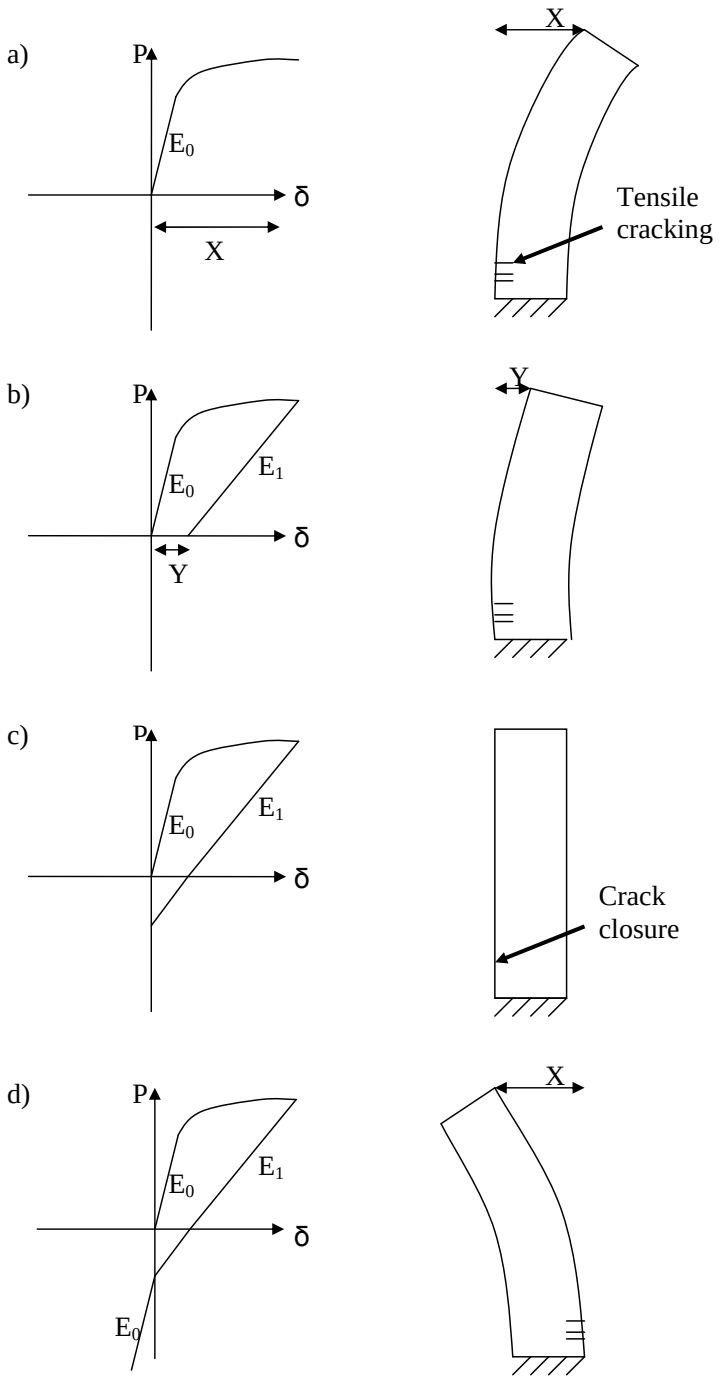

Figure 5.20: Illustrations of how crack formation and closure affects the load deflection relationship of a reinforced concrete member under cyclic loading and causes pinching behaviour.

5.4.4 Thermal loading of the test frame and determining the thermo-mechanical response

In this section the numerical results for the thermo-mechanical response of the frame is presented and are compared to the data obtained from the experimental setup. As the experimental investigation is still ongoing, only partial data was available. The numerical results discussed in this section are for a variety of simulations that, in addition to the permanent gravity and the vertical static loading, were subjected to:

(a) a purely thermal load when the concrete cover is assumed to remained present (i.e. the traditional method),

(b) a purely thermal load when directly simulating the loss of concrete cover,

(c) a cyclic mechanical load followed by a thermal load when the concrete cover is assumed to remained present (i.e. the traditional method),

(d) a cyclic mechanical load followed by a thermal load when directly simulating the loss of concrete cover through both load cases, and

(e) a cyclic mechanical load followed by a thermal load when directly simulating the loss of concrete cover through mechanical load case only.

The reason for the different simulations where the loss of cover is simulated within different phases is described more clearly in Chapter 4 where the automated damage model is used.

Due to the long descriptions of each of the scenarios, from this point onwards through this chapter, the data on the plots will be labelled “Simulation-a” through “Simulation-e” to represent the simulations above. Furthermore, it must be noted that all simulations included the vertical static mechanical loading.

5.4.4.1 Simulation applying the thermal loading only

First, a comparison between Simulation-a and Simulation-b was made, where the frames were subjected to gravity, static vertical loads and the thermal load. The experimen-

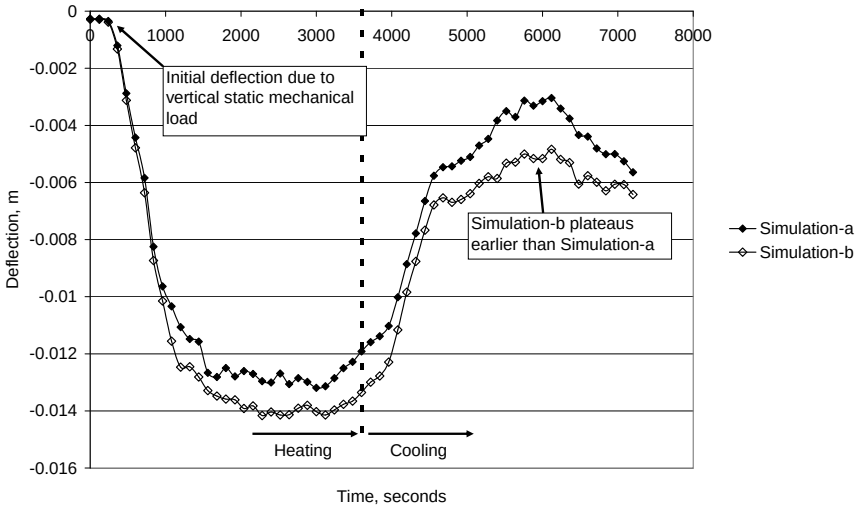

Figure 5.21: Plot showing the mid-slab vertical deflection for Simulation-a and Simulation-b. The initial vertical deflection produced by the static mechanical load is illustrated.

tal investigation into this scenario has not been completed as detailed in Table 5.1, therefore, this section presents the numerical results only.

Fig. 5.21 illustrates the relative mid-slab deflection of both the frames subjected to the same thermal load. It can be seen that both the frames had an initial deflection of 0.28mm (downwards) due to the vertically applied mechanical load. This was what was expected as normal loading should not cause crushing and the loss of concrete cover due to the build up of plastic strains.

As the thermal load was applied to the frames, thermal expansion of the inner surfaces and material degradation of the tensile reinforcement caused the general downwards deflection of the slab. Approximately 1000 seconds into the analysis the deflections of the two simulations begin to diverge from eachother. This is due to the concrete cover starting to become removed around the beam-column connections. Although the cover loss within the heating phase is quite small (see Fig. 5.22(a)) the lost through the build up of plastic stains is located around the beam-column connection. This change can be seen in Fig. 5.23 where the temperature of the reinforcement around

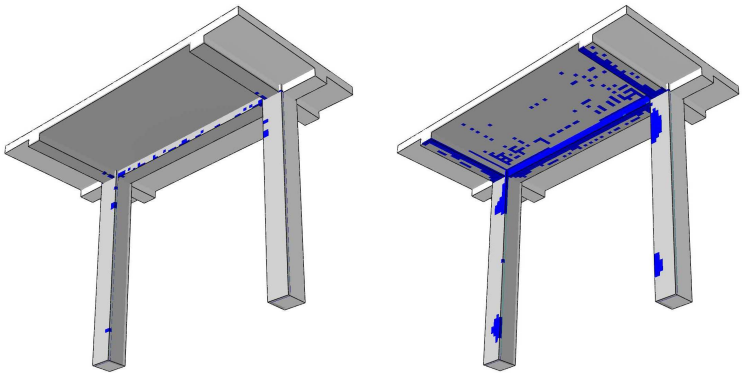

(a) State at 3600 seconds (b) State at 7200 seconds

Figure 5.22: Illustrations of the cover loss throughout the analysis. The blue highlighted regions are considered to be lost. (a) shows the state of the frame after the heating phase and (b) shows the state of the frame after the cooling phase. It is clear that much more cover is lost within the cooling phase rather than the heating phase due to a build up of compressive plastic strains. However, these strains are not localised around the beam-column connection.

the connections in Simulation-b begins to rise more quickly than in Simulation-a. This small loss from the connections leads to localised heading of the steel reinforcement and as a result simulation-b experiences larger downwards mid-slab deflections.

As the thermal load was removed and the gas temperatures reduced, the inner surfaces of the frame began to cool and contract. This contraction caused the upwards deflection of the slab as shown in Fig. 5.21. In addition to that, the columns began to rotate back due to the cooling of their inner surfaces. This rotation, in turn, placed axial compressive forces on the slab and at approximately 4500 seconds, the deflection of the slab once again began to plateau. Within this cooling phase, it was noted that much more concrete cover was lost on the beams and columns due to the thermal contraction and axial force placed upon the beams by the column rotations (see Fig. 5.22(b)).

Firstly, it should be noted that in Simulation-b the exposed steel around the connections will cool at a quicker rate and as further cover is lost, this effect is amplified. Secondly, as the cover became lost from the columns, the axial compressive forces produced by the cooling and contracting of their inner surfaces increased, and as a result,

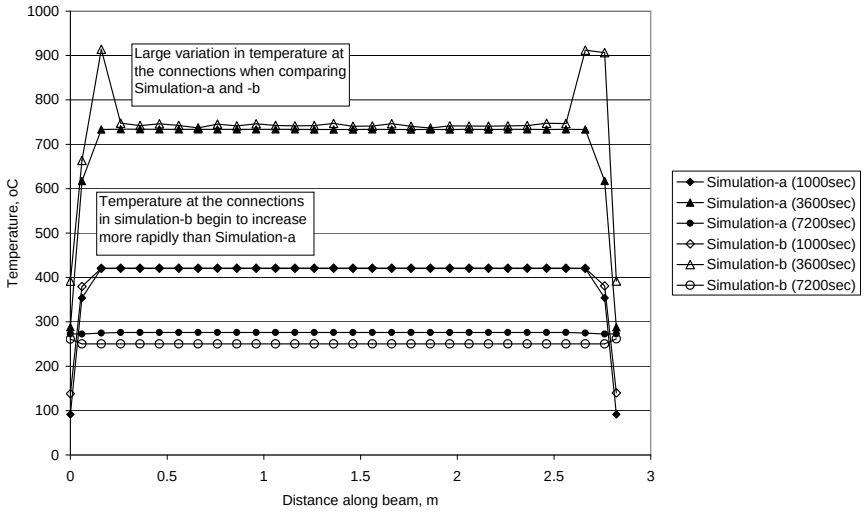

Figure 5.23: Plot showing the temperature profiles along the steel reinforcement of the beams at key times for Simulation-a and Simulation-b.

provided a greater restriction to the upwards deflection of the slab as shown in Fig. 5.21. As concluded in Chapter 4, it is the cover loss around the beam column connection that has the greatest effect on the overall thermo-mechanical behaviour of a reinforced concrete structure. Therefore, once again, the distribution of cover loss has been shown to be extremely important in the overall thermo-mechanical behaviour of a reinforced concrete structure and provides the reasoning behind the general form of Fig. 5.21.

Finally, at the end of the cooling phase, the vertical relative mid-slab deflection within both simulations was approximately 6mm (downwards), with Simulation-b having only a slightly larger downwards deflection in comparison to Simulation-a. Furthermore, it should be noted that as the frames' geometry and the thermal load were both symmetrical, there was no significant storey drift recorded.

5.4.4.2 Simulation applying horizontal cyclic mechanical loading and thermal loading

This section presents the numerical results from Simulation-c to Simulation-e with comparisons to Simulation-a, Simulation-b and the experimental results. First, a note on the observations from the experimental test is stated. These experimental observations have been relayed by the Indian Institute of Technology Roorkee.

Experimental observations

The fire test was performed for the planned duration of one hour. The temperature-time curve of the experimental gas phase is as defined in Fig. 5.24. A comparison between Fig. 5.24 and Fig. 5.12 shows that flashover was attained within 8-10 minutes. However, the temperatures achieved during the experimental test were higher that those achieved during the pre-testing pool fire study. The extremely high gas phase temperatures of 1200^oC to 1400^oC recorded at 0.09m and 0.16m from the pool surface is a result of the thermocouples being in direct contact with the flame. However, the other temperature points also show temperatures higher than those achieved in the pre-test pool fire study. Maximum surface temperatures that were recorded at the mid-span of the beam was 972^oC and at the mid-height of the column was 1002^oC, both of which exceed the assumed homogeneous surface temperature of 925^oC as detailed previously. This will inherently increase the temperatures within the structure, reducing its strength and therefore may lead to larger deflections.

It should be noted that the sound of concrete spalling from the roof slab could be heard clearly after 5 minutes of initial ignition, continuing for another 15 minutes. Later, the spalling of concrete was observed in beams and columns as well. A detailed visual inspection of the frame was undertaken the next day after the frame had cooled down. Considerable damage was noticed in the slab in terms of spalling of concrete and resultant exposure of reinforcement. The beams and columns suffered considerable spalling on exposed surfaces but only at a few locations; however widespread cracks could be clearly marked in these elements. This damage is shown in Fig. 5.25 and

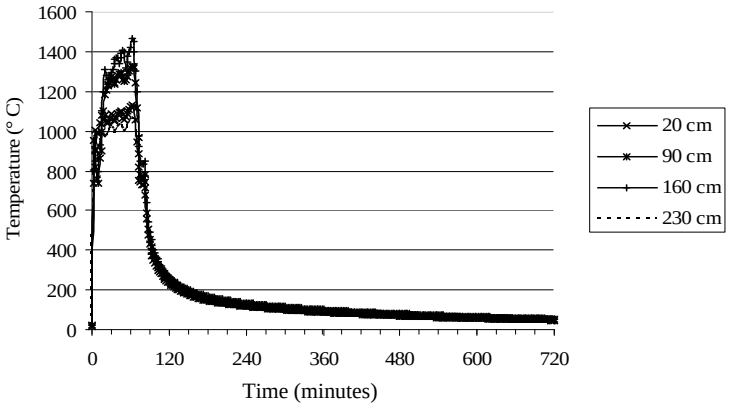

Figure 5.24: Illustration of the temperature-time curve achieved during the experimental test.

Fig. 5.26. The frame was able to withstand the one hour fire exposure without losing structural integrity in terms of complete collapse.

Temperatures through the depth of the beams and slab were recorded. Fig. 5.27 shows the vertical temperature variation through the center of the beam section at the mid-span. This plot illustrates high temperatures near the surface which then decrease rapidly into the section as expected with concrete. As seen in Fig. 5.26 the cover loss was limtied to the corner of the beam while the flat surfaces remained farily intact.

On the other hand, the thermal profile throughout the slab as illustrated in Fig. 5.28 shows that the temperature of the gas phase is allowed to penetrate through the depth of the slab due the extensive spalling illustrated in Fig. 5.26. The large variation at the depth of 60mm onwards at the times of 40 and 50 minutes may be down to flame contact or erroneous thermocouple sensors.

Unfortunately, due to unforseen curcumstances most of the experimental deflection data is unavailable. However, a maximum fire induced vertical displacement of 36mm was recorded in the roof slab.

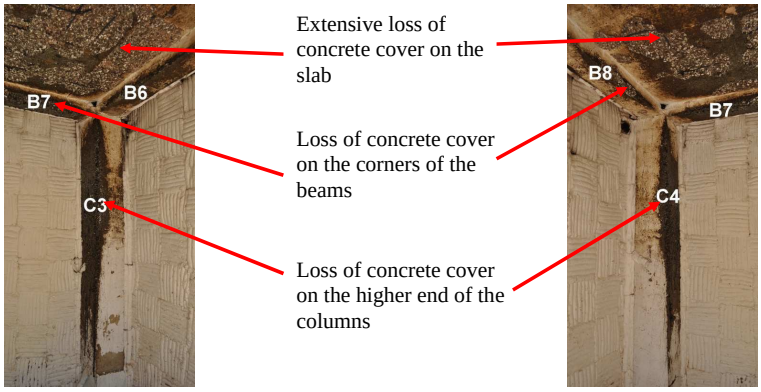

Figure 5.25: Photo: illustrating the damage that has occured on the beams and columns at the end of the testing.

Figure 5.26: Photo: illustrating the damage that has occured on the slab at the end of the testing.

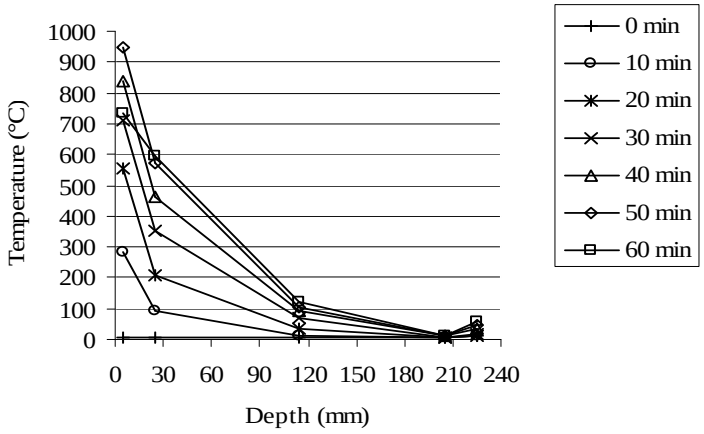

Figure 5.27: Plot illustrating the temperatures achieved at the mid-span of the beam at different times. These temperatures are measured on the vertical centerline of the seaction.

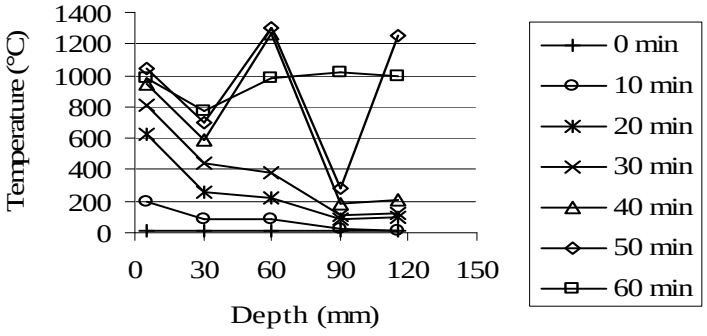

Figure 5.28: Plot illustrating the temperatures achieved at the slab at different times. These temperatures are measured at the mid-span and away from the opening.

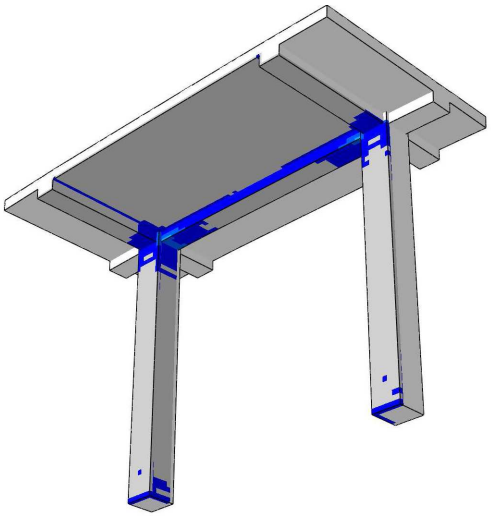

Figure 5.29: Illustration of the initial concrete cover loss induced by the horizontal cyclic mechanical loading, prior to the application of the thermal loading. The blue highlighted regions are considered to be lost.

Numerical comparison

The addition of the horizontal mechanical cyclic loading to the frame increased the magnitude and locations of the compressive plastic strains produced prior to any thermal loading. In terms of Simulation-c these compressive plastic strains did not result in loss of concrete cover, whereas for Simulation-d and Simulation-e, the build up of compressive plastic strains, induced by the cyclic motion, caused a great deal of concrete cover loss around the beam-column connections. This initial cover loss can be seen in Fig. 5.29.

As a result of the initial loss of concrete cover around the beam-column connection, the temperature of the steel reinforcement within those regions, increased rapidly with the application of the thermal load as shown in Fig. 5.30. From this plot, it was clear that the temperature of the reinforcement within the connections for Simulation-d and Simulation-e was much hotter and was similar to the surface temperature calculated previously while the temperatures of the traditional simulations (Simulation-a and Simulation-c) and Simulation-b (where little damage occurred at the connections)

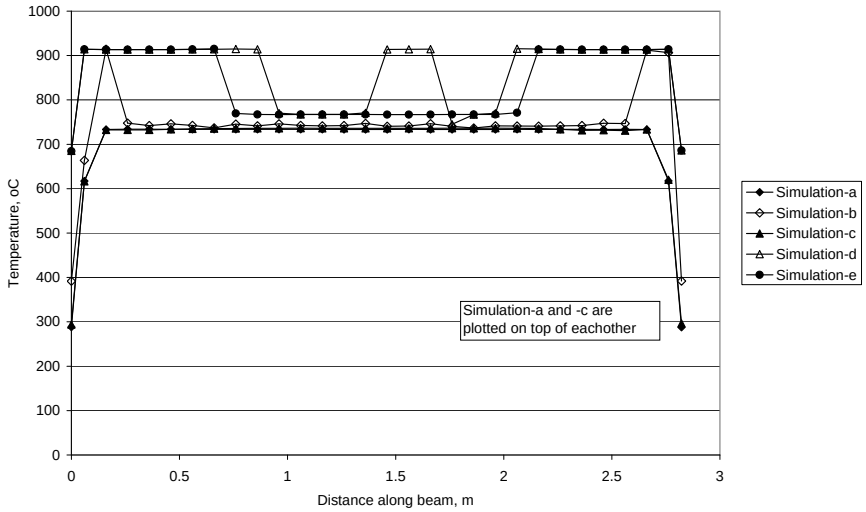

Figure 5.30: Plot showing the temperature profiles along the steel reinforcement for all Simulations at the end of the heating phase (i.e. 3600 seconds).

were significantly cooler around the connections.

Simulation-d did not continue to calculate the loss in concrete cover throughout the thermal phase of the test, and as a result, the loss of cover was fixed to the state shown in Fig. 5.29. On the other hand, Simulation-e did continue to perform this calculation throughout the thermal phase as shown in Fig. 5.31. In a comparison between these illustrations it can clearly be seen that the loss of concrete cover continues and similarly to Fig. 5.22 there was significant loss within the cooling phase.

However, it should be noted that contrary to the experimental observations, there was little cover loss simulated within the slab while most of the cover loss was located on the beams and columns. This additional cover loss as observed in the experimental setup, was due to thermal spalling which had not been directly simulated in the numerical investigation.

The location of cover loss simulated in comparison to Fig. 5.25 and Fig. 5.26 is quite accutate on the beams and columns. However, the lack of simulated cover loss on the underside of the slab illustrated that the subroutine, in its current state, is unable to simulate the phenomenon of explosive thermal spalling which was observed

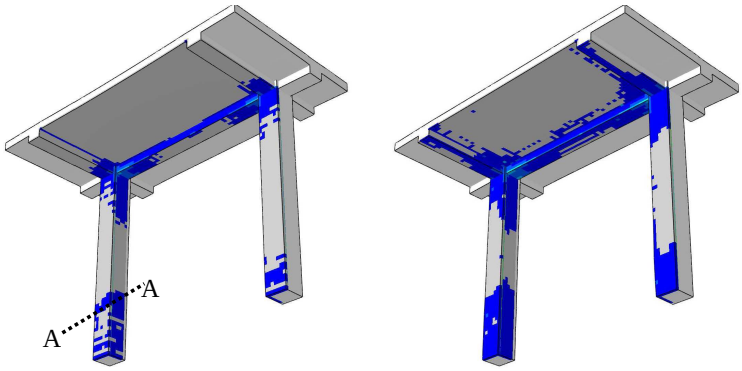

(a) State at 3600 seconds (b) State at 7200 seconds

Thermal profiles of column at Section A-A

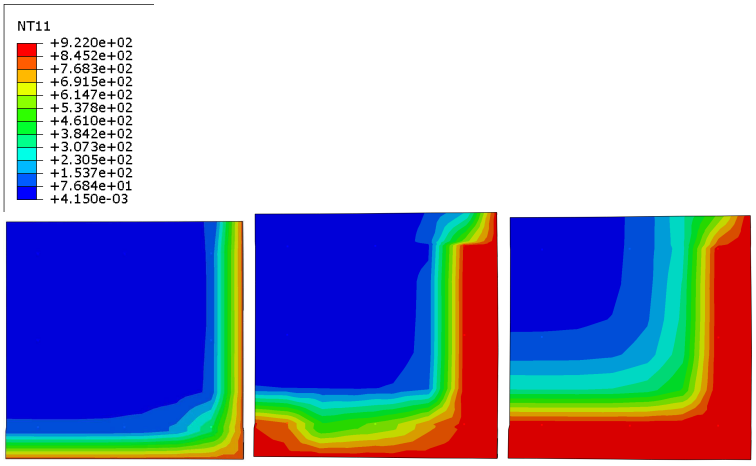

(c) 600 seconds (d) 1200 seconds (e) 3600 seconds

Figure 5.31: Illustration of the concrete cover loss calculated throughout the thermal loading in addition to that induced by the horizontal cyclic mechanical loading. The blue highlighted regions are considered to be lost. (a) shows the state of the frame after the heating phase and (b) shows the state of the frame after the cooling phase. Also, temperature profiles are provided showing the temperature at (c) 10 minutes, (d) 20 minutes and (e) 60 minutes.

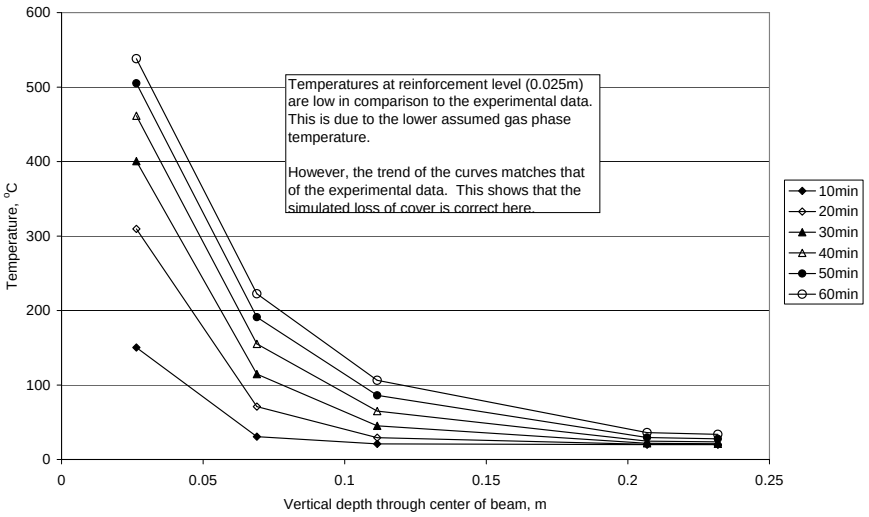

Figure 5.32: Plot illustrating the temperatures simulated at the mid-span of the beam at different times. These temperatures are measured on the vertical centerline of the seaction.

during the experiments. Furthermore, the cover loss within the experiment may not be complete to expose the reinforcement as assumed with the numerical simulations. These factors will cause of difference to occur in the thermo-mechanical behaviour of the frame as discussed below.

From a comparison between Fig. 5.32 to Fig. 5.32 it can be seen that the temperature variation simulated through the beam section is relatively similar to those experienced during the experiment (see Fig. 5.27). However, the magnitude of this variation is lower within the simulation which is expected when considering the lower assumed gas and surface temperatures. A comparison of the thermal profiles throughout the slab illustrates the lack of simulated cover loss. The simulated temperatures in Fig. 5.33 match quite well to the experimental data upto 30 minutes of heating where the reinforcement level reaches approximately 400^oC. At this point the temperature of the reinforcement within the experimenal data increases much more rapidly than simulated due to the occurance of thermal spalling.

The concrete cover loss as described and as modelled in Simulation-d and Simulation-e did not only allowed the gas temperatures to directly affect the steel reinforcement

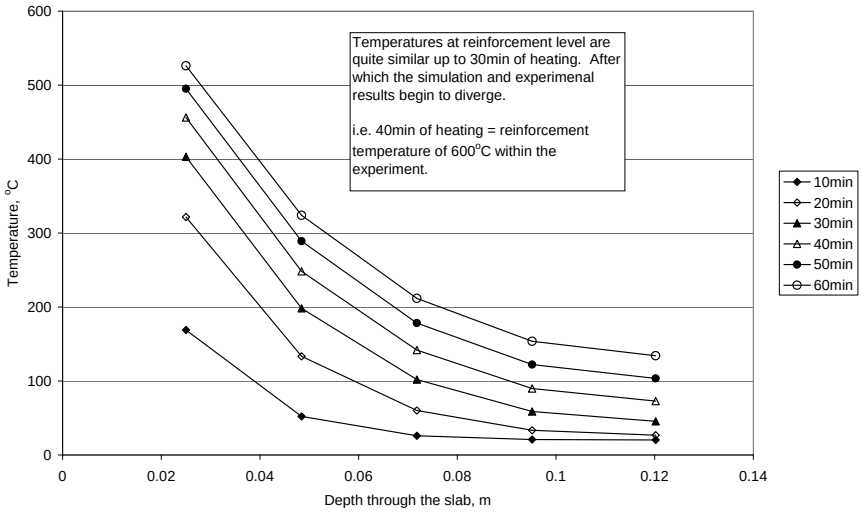

Figure 5.33: Plot illustrating the temperatures simulated at the slab at different times. These temperatures are measured at the mid-span and away from the opening.

but also reduced the rotational stiffness of the connection (also illustrated in Chapter 4. From Fig. 5.34 it is clear that simulation of the loss of concrete cover led to a significant variation in the thermo-mechanical behaviour of the frame when subjected to a thermal load.

A comparison between Simulation-c, Simulation-d and Simulation-e shows that, in the presence of a thermal load, the loss of concrete cover within the region of the connections led to increased rate and magnitude of downward deflection of the slab, as shown in Fig. 5.34. The maximum mid-slab deflection was calculated to be 29mm (zeroed at the start of the thermal phase), a 36% increase in the maximum mid-slab deflection when compared to Simulation-c.

However, the maximum deflection calculated by Simulation-e still did not match the mid-slab deflection of 36mm which was recorded during the experimental investigation. This was due to a number of factors. Firstly, the surface temperatures recorded during the experimental investigation were higher than those calculated for the numerical simulations. Secondly, the fact that thermal spalling was not accounted for in the numerical simulations while this phenomenon and the subsequent reveling of

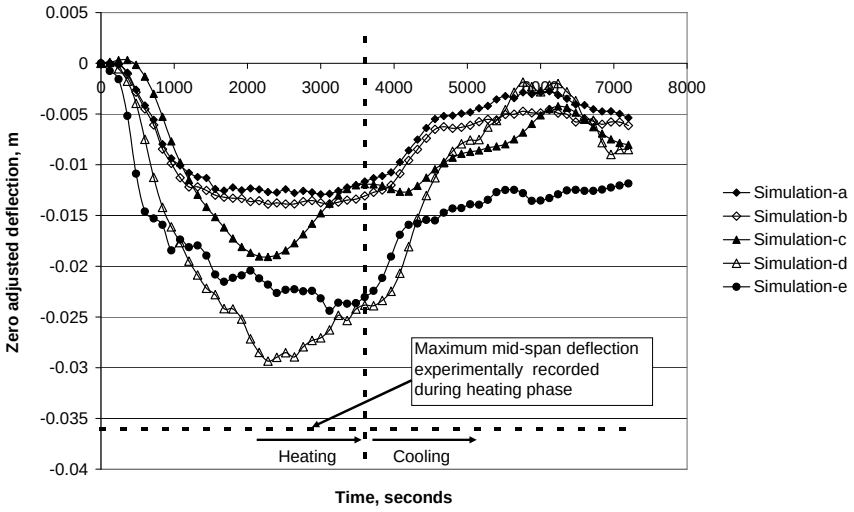

Figure 5.34: Plot showing the mid-slab vertical deflection for all simulations. The maximum mid-slab vertical deflection recorded during the experimental investigation is also shown illustrated.

the slab reinforcement was observed within the experimental investigation. The hotter temperatures and the greater level of cover loss within the slab could account for this discrepancy.

Finally, as illustrated in Fig. 5.35, all simulations show a gradual and overall drift throughout the thermal phase that caused the frame to become more upright with the greatest drift occurring in the frames with simulated concrete cover loss.

5.5 Conclusions

In this chapter a numerical simulation of an experimental test frame subjected to extreme mechanical and thermal loading has been presented and compared. As the experimental programme is still ongoing,some results were not fully avilable from the experimental source and as a result, limited comparison was made.

The numerical simulation of the mechanical cyclic loading of the frame proved to be in very good agreement with the results obtained from the experimental setup. The

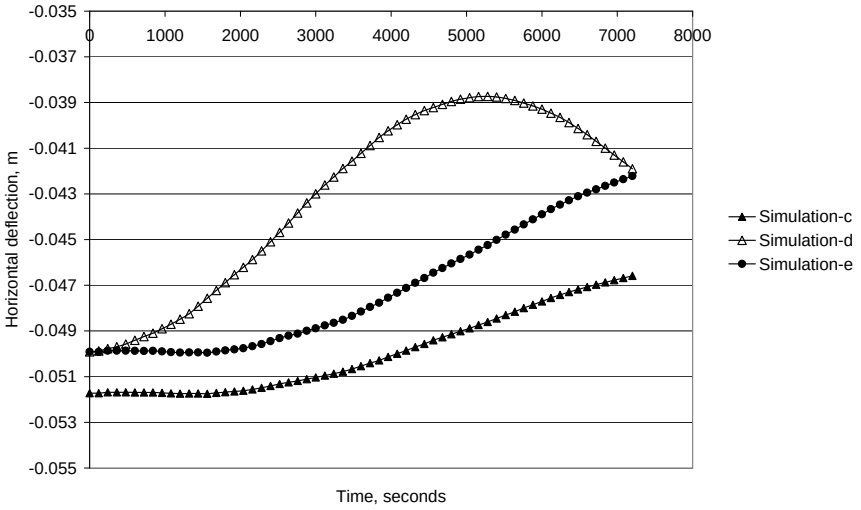

Figure 5.35: Plot showing the frame drift (at slab height) throughout the thermal loading for Simulation-c, Simulation-d and Simulation-e.

maximum load achieved within the simulations was within approximately 10% of the experimental maximum for traditional simulations, and within 5% of the experimental maximum when directly considering the loss of concrete cover as a result of excessive compressive plastic strains. Furthermore, when considering the loss of concrete cover, the load required to achieve the maximum subjected deflections reduced which was also observed within the the experimenal data. This behaviour was not observed during the traditional simulation and therefore, it can be concluded that the simulation of reinforced concrete frames subjected to excessive mechanical loads must include the loss of concrete cover to achieve a better determination of the actual behaviour.

The adoption of an automatic damage calculation method through the use of the subroutine as detailed in Chapter 4 allowed the simulation of concrete cover loss due to a build up of excessive compressive plastic strains. Once again, as illustrated in Chapter 4, loss of concrete cover around the beam column connection causes large variations due to increased thermal propagation and a reduction in rotational stiffness leading to a more flexible structure. However, it was difficult to accurately replicate all mechanisms which caused the cover loss. For instance, lack of simulated spalling from the heated

side of the slab and the assumption that all the cover depth becomes removed are factors that led to the discrepancy between the simulations and experimental data. Therefore, it must be concluded that although simulation of the loss of cover is required, more experimental data is needed into this area to obtain suitable values for the subroutine's criterion which has the potential to incorporate pore pressures to simulate spalling due to increasing tensile stresses and pore water pressure.

It has been shown that it is possible to effectively simulate the some of the mechanical mechanisms such as cover loss from a build up of compressive plastic strains. However, further research is required to improve the accuracy of this method and to incorporate a method to simulate thermal spalling.

Once again the analyses performed in this chapter have shown that the integrity of the thermal resistance (i.e. concrete cover) around the beam column connections is extremely infulential for the thermo-mechanical behaviour. Therefore, it is necessary to enhance the integrity of the concrete cover within these regions to insure that the building reacts in a predictable manner.

Chapter 6

Fibre implementation for improved concrete cohesion

6.1 Introduction

Through the experimental and numerical studies performed and reported upon in this thesis, it is clear that a method is required to enhance the stability and integrity of the concrete cover with the main aim of preventing the loss of cover under sequential extreme mechanical and thermal loading scenarios; hence maintaining the designed fire resistance for the member and structure.

Although crushing of the concrete is a result of excessive compressive strains, the loss of cover is a function of the cohesion of the concrete following the phenomenon of crushing (i.e. the connectivity of the cover to the rest of the body of the member). Therefore, to enhance the stability and integrity of the concrete cover, it is necessary to increase the cohesion of the concrete. To achieve this, a variety of fibres (micro synthetic, macro synthetic and steel) were added to the concrete mix (detailed in the materials below). Beams of the different mixes were cast and placed under four point bending until crushing of the compressive surface occurred and the level of cover loss documented. The compressive surfaces were then heated via radiant heat panels and in addition to the cover loss, the thermal propagation through the different beams was documented to determine whether the thermal resistance was retained.

The use of embedded fibres has been previously used increase the ductility of a

specimen under ambient temperatures and to reduce thermal spalling of an intact specimen. However, if the specimen has undergone excessive compressive stresses and strains to result in crushing, it is unclear if the use of fibres will then reduce the probability of the loss of this crushed concrete if subjected to a thermal load.

The experiments detailed in this chapter are designed to establish:

(a) if the use of fibres increase and retain the the cohesion of compressively crushed concrete throughout a thermal load, and

(b) which fibre type is the most effective.

6.2 Previous work

Fibre reinforced concrete members are members which contain randomly dispersed and randomly orientated fibres throughout with the aim of producing a more cohesive mix.

Fibre reinforced concrete is used primarily due to its increased durability, toughness, crack resistance and tensile properties (Buchanan 2001). These properties are advantageous by reducing the cracking and increasing the stability and integrity of the concrete in the post-yielding behaviour. This is achieved by the fibres absorbing the strain energy and reducing the rate of crack growth (Zollo 1997), resulting in a composite material that is both strong and ductile.

In fire applications, fibres are also used to reduce or stop spalling from occurring. There has been a lot of research into the field of spalling prevention with the use of fibres (Khoury 2000, 2008, Sideris et al. 2009). There are two main mechanisms which are attributed to this behaviour. The first is the increased tensile strength provided by the fibres which provides a better mechanism to act against the high thermal gradients that are produced within a concrete member subjected to an extreme thermal load. The second is that as the temperatures increase, the fibres expand forming micro cracks within the concrete which provides paths to allow the increasing vapour pressure, produced by the increasing temperatures, to escape (Khoury 2008). Following on from the second mechanism and referring to synthetic fibres, as the temperatures increase

further, these synthetic fibres will melt, resulting in the producing of air voids within the concrete. Once again, these provide an escape for an increasing vapour pressure.

6.3 Experimental Methods and Materials

6.3.1 Apparatus

Concrete beams with different fibrous content as detailed in Table 6.1 were loaded in four point bending to deflection levels that exceeded the elastic capacity of the concrete and caused crushing of the compressive surface. The beams were then unloaded and the compressive surface heated via radiant heat panels and the thermal profiles produced within the beams recorded by embedded thermocouples.

Studying the mechanical and thermal behaviour of the beams enabled it to be determined whether the addition of fibres enhanced the cohesion of the compressive side of the beam and hence retain its fire resistance. In addition to this it can be determined which type of fibre provides the most effective means of cohesion throughout both mechanical and thermal loading. The details of the testing arrangements are shown in Fig. 6.1 to Fig. 6.5 and the individual test details listed in Table 6.1.

The beam design was based on the design used in Chapter 3 with only minor differences. The beams were doubly reinforced with 10mm diameter steel bars and had a span of 870mm and cross-sectional dimensions of 90x140mm. Concrete cover was a uniform 20mm on all sides.

Beams 1 to 4 as detailed in Table 6.1 were thermally loaded only. This was to determine the thermal propagation through an undamaged specimen along with ascertaining whether the addition of fibres into the mix caused a change in the global thermal properties.

The pure non-fibrous beams (beam 5 and 6) were loaded vertically downwards as shown in Fig. 6.1 and the load-deflection relationship was recorded. The mid-span deflection applied to the beams is of the magnitude that produces strains in the compressive side that exceed the crushing strain of the concrete. As a result the

Table 6.1: Load cases to be performed for the investigation into fibre implementation for improved concrete cohesion.

Beam	Thermo-couples	Loading Phase	Heating Phase	Description
1	√	-	√	Pure non-fibrous concrete beam subjected to thermal loading only
2	√	-	√	Concrete beam mixed with micro fibres subjected to thermal loading only
3	√	-	√	Concrete beam mixed with macro fibres subjected to thermal loading only
4	√	-	√	Concrete beam mixed with steel fibres subjected to thermal loading only
5	√	√	√	Pure non-fibrous concrete beam loaded incrementally to determine flexural crushing deflection and subsequently heated to determine the effect on thermal propagation.
6	√	√	√	Repeat of beam five.
7	√	√	√	Concrete beam mixed with micro fibres loaded incrementally to set flexural crushing deflection and subsequently heated to determine the effect on thermal propagation.
8	√	√	√	Repeat of beam seven.
9	√	√	√	Concrete beam mixed with macro fibres loaded incrementally to set flexural crushing deflection and subsequently heated to determine the effect on thermal propagation.
10	√	√	√	Repeat of beam nine.
11	√	√	√	Concrete beam mixed with steel fibres loaded incrementally to set flexural crushing deflection and subsequently heated to determine the effect on thermal propagation.
12	√	√	√	Repeat of beam eleven.

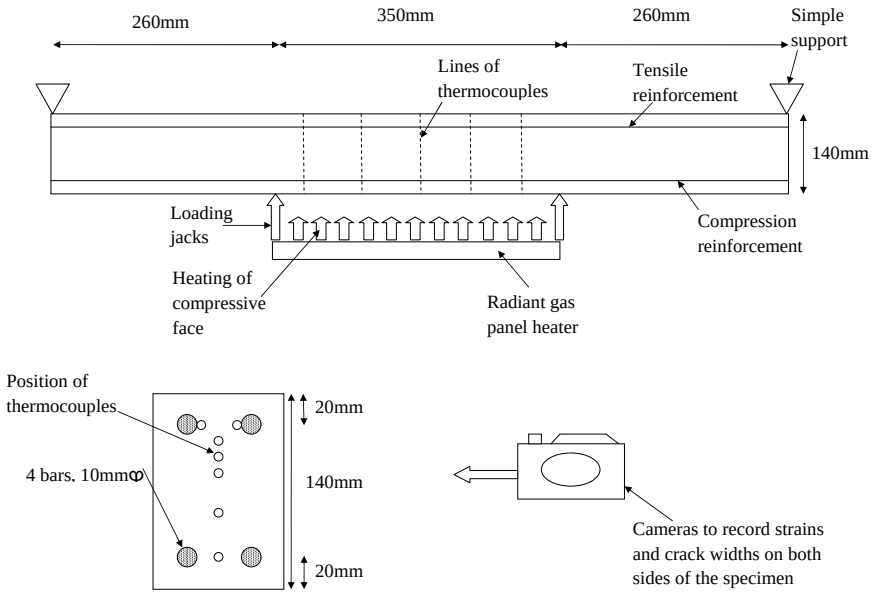

Figure 6.1: Experimental set-up for the investigation into fibre implementation for improved concrete cohesion. Showing a side-view of a beam, a typical section and general locations of the thermocouples.

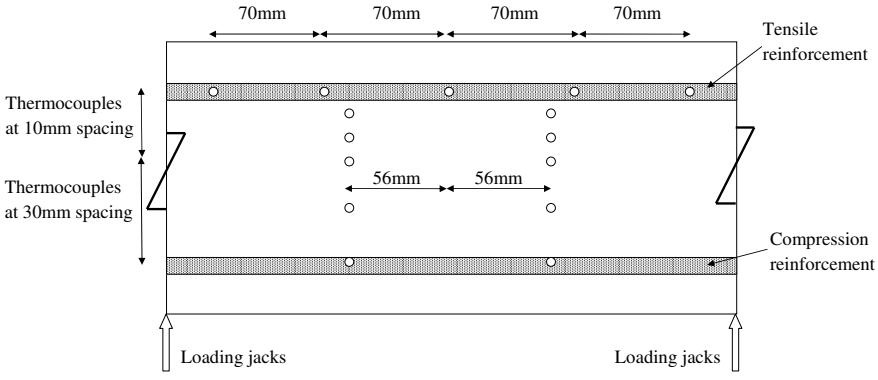

Figure 6.2: Thermocouple locations embedded within the beams at the mid-span for the investigation into fibre implementation for improved concrete cohesion.

compressive side of the concrete will undergo crushing, possibly leading to the removal of the crushed concrete cover. The applied deflection and crushing deflection and strains are all reported upon in section 6.4.

The deflection required to cause crushing in the non-fibrous beams (beams 5 and 6) was then applied to the fibrous beams (beams 7 to 12). This was to determine whether the addition of fibres into the mix contributed significantly to the cohesion of the concrete hence avoiding loss of cover through a damaging mechanical event.

The arrangement shown in Fig. 6.1 allowed for a suitable length of mid-span of the beam to be placed under pure bending, which theoretically causes a uniform compressive strain along this length for a given depth. The orientation of loading allowed any crushed regions to be removed more freely through the action of gravity.

After the required deflection had been obtained by mechanical loading, the beams were unloaded completely before the thermal load was applied to the damaged compressive face of the beams from above via a propane gas fueled radiant panel (Fig. 6.5). The radiant heat panel was adjusted to provide a thermal load of 46kW/m^2 $\pm$5kW/m^2. The aim was to apply this thermal load for an hour and then to allow it to cool naturally for one hour. However, due to the failure of the panels in some of the test cases at 30 minutes, a true comparison can only be made up to this time. Therefore, the results published will be for the first 30 minutes of heating and will not include the cooling phase. Fire-board insulation was provided on the sides of the beams to ensure that 1-D heat transfer was achieved (Fig. 6.5).

Loads were recorded and verified using two different methods. The first method was via the dial that was supplied with the loading rig. The second method used carefully placed strain gauges on the steel loading cross member (Fig. 6.3) which had been calibrated prior to testing. The deflections of the beams were calculated using a deflection gauge placed at the mid-span of the beam and secured to the loading rig. The load and deflection data was recorded in real time at 2s intervals while high resolution digital photographs were taken of both sides of the beam between the loading points at 10s intervals, which were then post-processed to determine the strain field development

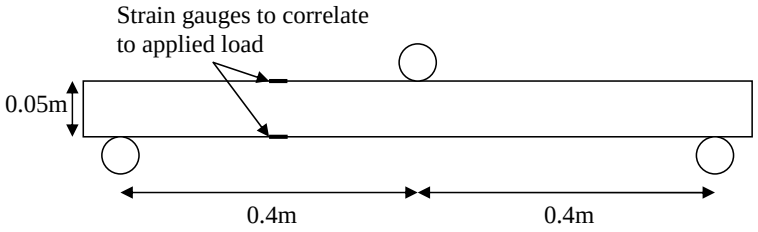

Figure 6.3: Manufactured cross member used in loading of the beams. This cross member is also fitted with strain gauges to calculating the applied load.

within the beam cross-section. The digital image correlation (DIC) method used is discussed in a Appendix E.

Temperatures in the beams were recorded through the use of a number of thermocouples, the locations of which are shown in Fig. 6.1 and Fig. 6.2. K-Type thermocouples were used throughout which have a tolerance of $\pm 1.5\,^{\circ}\mathrm{C}$. The fire resistance of a reinforced concrete section is based on the cover's ability to insulate the steel reinforcement, therefore the longitudinal compression reinforcement was instrumented with thermocouples along its length at the mid-depth of the reinforcement. Also, thermocouples were placed throughout the depth to record the propagation deeper into the section. All these details and other aspects of the experiments are shown in Fig. 6.1 to Fig. 6.5.

To ensure that the thermocouples would not be displaced by settling concrete, the thermocouples on the compression reinforcement were tied using steel tying wire and the thermocouples that were set through the depth were placed in the concrete beams after casting but while the concrete was still wet. The placement of thermocouples post casting was quite a crude process. Nonetheless, as shown in chapter 3, this method was found to be accurate to within a 5% accuracy and can be clearly determined, through the profile of the thermal data, whether individual thermocouples had been misplaced. Furthermore, the thermocouples were not placed within the concrete cover

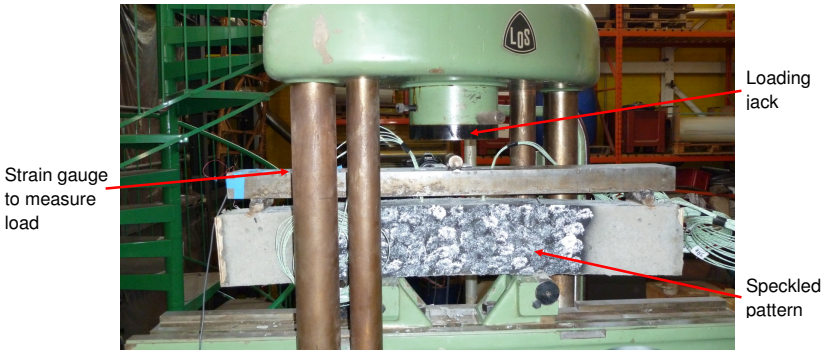

Figure 6.4: Photo: The loading set-up used to produce crushing of the compressive surface. The speckled area (black and white pattern) used for strain measurements is also shown as well as the load cell used to calculate the load applied.

Figure 6.5: Photo: Thermal set-up of the test, showing the orientation of the radiant heat panels and beams. The insulation used to provide the system with one dimensional heat transfer is also shown.

Table 6.2: Concrete mixing ratios for the investigation into fibre implementation for improved concrete cohesion.

Cement (kg/m^3)	Coarse Agg. (kg/m^3)	Fine Agg. (kg/m^3)	Water (kg/m^3)
454	1130	635	138

on the compression side to avoid any interference with the cover loss and to keep the thermocouples protected.

During the thermal loading of the beams, the beams were placed at a distance of 120mm from the surface of the radiant heat panels and the whole arrangement was tilted at an angle of 10^o. This was to ensure that the convective processes were taken removed or significantly reduced from the set-up in favour of a purely radiative heat flux. A feasibility study was carried out to measure the heat fluxes and their uniformity over the total area of the panel. This study is reported in Appendix F.

6.3.2 Materials - concrete components

Portland-fly ash cement conforming to BS EN 197-1:2000 (BSI 2000a) with a percentage fly ash of 5% to 7% was used throughout the experimenal programme. The chemical composition of this cement is detailed in Table 6.3.

The course aggregate was uncrushed and had a nominal diameter of 10mm. The fine aggregate was also uncrushed and was characterised as 80% passing a 600μmm sieve. The design ratios of cement, course aggregate, fine aggregrate and water are shown in Table 6.2. The beams were cast two at a time to make sure the same mix was used for both beams of each of the mix types. Full design details are reported in Appendix A.

A slump test was carried out to assess the workability of the wet concrete. This was performed in accordance with BS EN 12350-2:2009 (BSI 2009). The slump of the concrete mix for all mixes ranged between 40mm to 60mm.

Table 6.3: Chemical composition of the portland fly-ash (% by weight).

Compound	% weight
CaO	40.9
SiO_2	33.2
Al_2O_3	6.3
Fe_2O_3	4.1
SO_3	1.6
Na_2O	0.1
K_2O	1.2
Insoluble	21.6

6.3.3 Materials - fibres

It was difficult to choose the dosage to use for each fibre type for this type of application. Therefore, as a starting point, the dosage of the fine synthetic fibres was defined in terms of the recommendations set out by Eurocode 2 (2004) that states to prevent spalling within high strength concrete a fine synthetic fibre dosage of 2kg/m^3 should be specified. From this, the dosages for the other fibre types (coarse synthetic and steel) were calculated using the following method.

Ideally during post yielding of a fibre reinforced specimen, the fibres will pull out of the concrete resulting in a slower plastic deformation rather than a quick brittle rupture failure of the fibres. This is dependent upon the bond between the fibre and the concrete, therefore, when calculating the dosage of the coarse synthetic and steel fibres the ratio of curved surfaced area(λ), effective diameter(ϕ_e) and anchorage length(Ψ) was utilised ($\lambda.\phi_e/\Psi$). Due to the material difference between synthetic and steel, the steel fibre dosage was also scaled by the difference in density. The calculation and summary of the fibre dosages can be found in Table. 6.4

It should also be noted that the water absorption of the synthetic fibres was also taken into account within the mix designs, the details of which can be found in Appendix B.

Table 6.4: Calculation and summary of fibre dosages for the investigation into fibre implementation for improved concrete cohesion.

	Density, kg/m^3	Diameter, m	Width, m	Length, m	Depth, m
Micro Synthetic fibres	900	3.2e$^-$5	-	-	-
Macro Synthetic fibres	900	-	0.0014	0.04	0.00011
Steel fibres	7850	0.001	-	-	0.05

	ϕ_e, m	λ, m^2	$\lambda.\phi_e/\Psi$, m^2	Dosage, kg/m^3	Density Scaled Dosage, kg/m^3
Micro Synthetic fibres	3.2e$^-$5	8.04e$^-$10	7.4e$^-$1	2	-
Macro Synthetic fibres	4.43e$^-$4	1.54e$^-$7	7.4e$^-$1	3.06	-
Steel fibres	0.001	2.21e$^-$6	7.4e$^-$1	204	23.4

6.3.4 Concrete Properties

All specimens (i.e. cubes and cylinders) and beams 5 to 12 were mechanically tested 28 days after casting to determine the mechanical properties such as density, compressive strength and tensile strength. The compressive and tensile strength of the concrete was carried out conforming to BS EN 12390-3:2002 (BSI 2002) and BS EN 12390-6:2000 (BSI 2000b) respectively. The compressive strength, tensile strength and density are shown in Table 6.5. These show that the tensile strength of the concrete ranges from approximately 7.6% to 9% of the compressive strength. A more indepth analysis of how the addition of fibres affects the mechanical properties is given in the results section.

The beams are then allowed to cure for a further 28 days (56 days total) to allow the moisture content to drop further before performing the thermal tests.

Table 6.5: Concrete compression and tension properties for the investigation into fibre implementation for improved concrete cohesion.

Beam type		Density (kg/m^3)	Compressive Cube strength (N/mm^2)	Split cylinder tensile strength (N/mm^2)
Non-fibrous	Average	2371	44.2	3.4
	Maximum	2435	58.0	4.3
	Minimum	2288	31.7	2.6
Micro Synthetic	Average	2365	43.2	3.3
	Maximum	2440	58.6	4
	Minimum	2274	30.4	2.8
Macro Synthetic	Average	2358	38.0	3.4
	Maximum	2428	51.7	4.1
	Minimum	2281	27.7	2.4
Steel	Average	2381	39.7	3.9
	Maximum	2447	53.7	4.7
	Minimum	2297	30.2	2.9

6.4 Experimental Results

6.4.1 Crushing strain and cover removal

The initial aim of this experimental investigation as stated in the introduction, is to determine the effectiveness of different types of fibres to increase the cohesion of a concrete specimen or reinforced concrete member under post yielding loading conditions.

From Table. 6.5 it can be seen that all fibrous specimens reach their maximum stress state at a slightly lower compressive load than that of the non-fibrous specimens. However, while the non-fibrous specimens break apart and are unable to take any further load beyond their ultimate load, fibrous specimens held their shape to some extent and were able to continue to take some load beyond their ultimate load, although at a lower capacity. This effect was due to the "bridging" effect of the fibres as illustrated in Fig. 6.6 where the crushed member was held together by the fibres. Although the maximum tensile strength is not significantly increased, once again the fibrous specimens failed in a more ductile manner and hence were able to continue to take further loading at a reduced capacity.

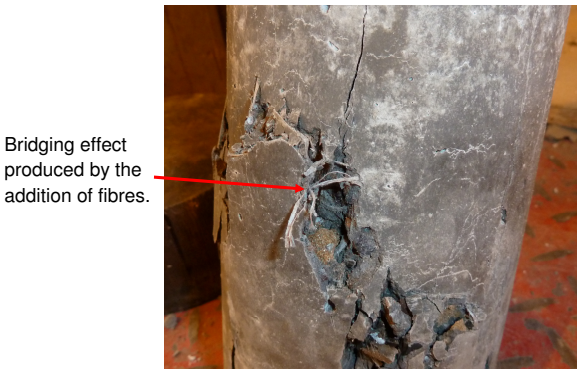

Figure 6.6: Photo: Crushed cylinder specimen of a mix with macro synthetic fibres. Illustrating the bridging effect of the fibres within the post yielding behaviour.

To determine when crushing of the compressive surface occurs, the pure non-fibrous beams (beams 5 and 6 in Table. 6.1) were loaded while their load-deflection behaviour and strain fields recorded. The load-deflection relationship was measured and recorded in real time whereas the strain fields were calculated in post experimental analysis with the use of Digital Image Correlation (DIC) software as described in Appendix E. As a result the damage level was defined in terms of its load-deflection relationship (Fig. 6.7). As previously discussed in Chapter 3, it is difficult to define a point (i.e crushing) within the post yielding behaviour of a member as it requires little to no further loading for an increase in mid-span deflections, therefore throughout the experimental program the damage level was defined in terms of the mid-span deflection.

Fig. 6.7 shows the load deflection behaviour of the pure non-fibrous beams 5 and 6 subjected to a mechanical load. As seen from Table 6.6 the elastic stiffness of the beams are very similar hence indicating that the overall dimensions and the layout of the reinforcement are also very similar. However, it can be seen that there was a notable difference in the post yielding behaviour. Beam 5 (first loaded) reached a maximum load of 86kN at a deflection of 11mm, whereas beam 6 (second loaded) reached a maximum load of 105.5kN at a deflection of 14.5mm. This difference can be explained through the way the compressive side acted in this post yielding region.

Beam 5 (first loaded) was loaded to its maximum where the compressive surface suddenly crushed in a localised region, reducing the load carrying capacity of the beam

Table 6.6: Comparison of the elastic stiffness of the beams for the investigation into fibre implementation for improved concrete cohesion.

Beam type	Stiffness, kN/m^2	% error
Non-fibrous	9.29x10^6	N/A
Micro synthetic	9.64x10^6	3.70
Macro synthetic	9.35x10^6	0.37
Steel	9.69x10^6	4.20

and, as a result, the load required to provide the same deflection also suddenly reduced (see Fig. 6.7). Although the compressive cover has crushed, it has not become removed from the beam at this load/deflection, therefore the beam was loaded further, increasing the mid-span deflection. Through the analysis of Fig. 6.9, Fig. 6.8 and Fig. 6.10 it can be shown that the location of the localised crushing to be situated to the left of the mid-span and this region of crushed concrete finally became removed from the beam at an approximate deflection of 17mm. With the aim to ensure the tests are repeatable, the beam continued to be loaded to a maximum mid-span deflection of 20mm whereby it was then fully unloaded and a plastic deflection of 11.6mm was observed (see Fig. 6.7).

Beam 6 (second loaded) has a similar pre-yielding behaviour as illustrated in Fig. 6.7. However, as the beam yields the load required to cause increased mid-span deflections continued to increase relative to beam 5. Although crushing of the compressive surface occurred, it was observed that there was no sudden decrease in load as occurred with beam 5. This was because crushing of the surface was more widespread and did not completely localise in one region and, in addition, no significant cover loss was observed throughout the complete mechanical loading cycle. Once again, the plastic deformation of the beam after unloading was approximately 11.2mm (i.e. similar to beam 5).

The maximum deflection applied to the beams was 20mm, therefore the subsequent fibrous beams (beams 7 to 12) were all loaded to the same maximum deflection of 20mm. Fig. 6.11 to Fig. 6.13 illustrates the average load deflection curves for each fibrous beam type with the inclusion of error bars to show the spread of data. The

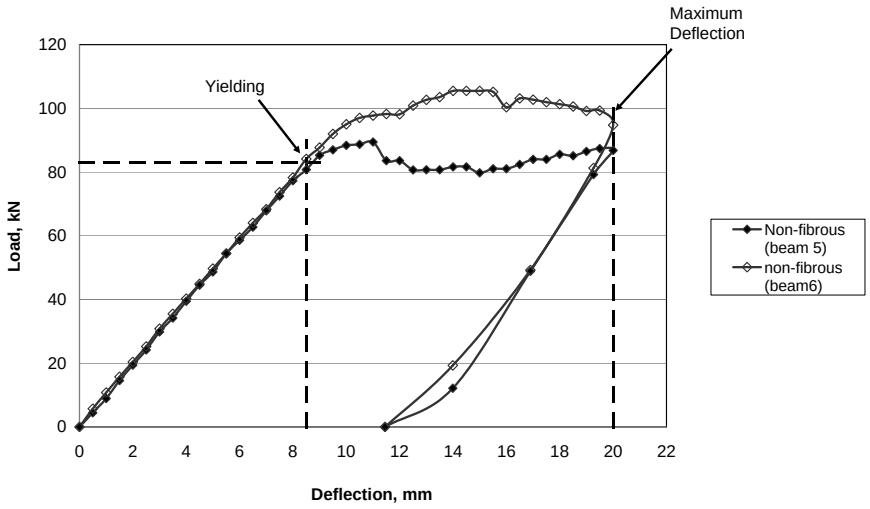

Figure 6.7: Plot showing the load deflection relationship of the non-fibrous beams.

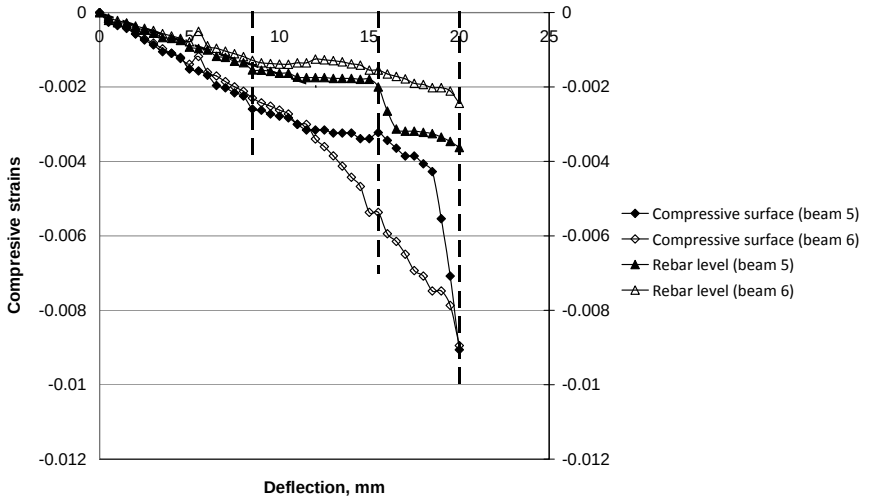

Figure 6.8: Plot showing the compressive strains produced within the non-fibrous beams.

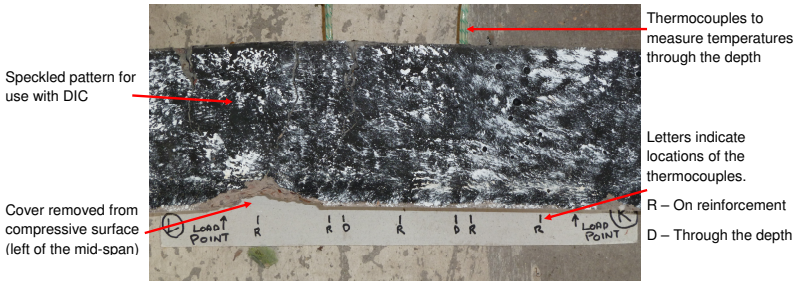

Figure 6.9: Photo: Illustrating the loss of cover in beam 5. This loss of cover occurred during mechanical loading and occurred at a location of -140mm from the mid-span.

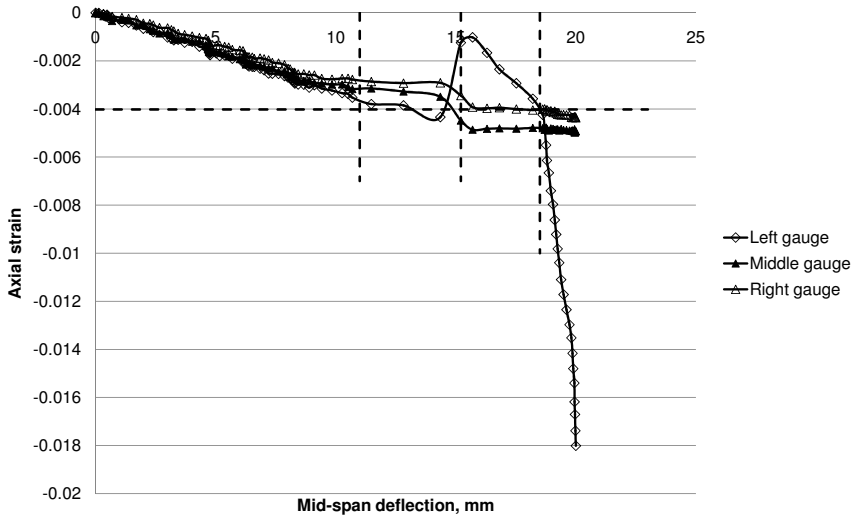

Figure 6.10: Plot showing the compressive strain pattern over the compressive surface with the highest strains recorded on the left gauge (i.e. crushed region).

fact that the spread of data was significantly reduced throughout the entire behaviour when compared to that of the non-fibrous beams indicated that the addition of fibres increased the homogeneity of the mix and, as a result, allowed the tests to be more repeatable and reliable.

Fig. 6.14 plots the average load deflection relationship of the fibrous beams against beams 5 and 6. It can be seen that the addition of fibres, of any type, does not significantly affect the pre-yielding behaviour ($\leq$8.5mm) of the beam as all beams had a similar stiffness (Table 6.6). However, the post yielding behaviour of all the fibrous beams indicated a lower initial yielding load but they still retained the capacity to support a notable increase in load. This is shown in that the final load applied to reach the maximum mid-span deflection was similar to that of a non-fibrous beam (see Fig. 6.14).

The addition of fibres resulted in a more homogeneous mix and therefore crushing of the concrete was more uniform along the compressive surface as indicated by the gradual increase in strain with deflection in Fig. 6.15. Although crushing of the compressive surface occurred on all fibrous beams there was little to no loss of cover, hence the thermal insulation provided to the steel reinforcement was still supplied at the beginning of the thermal phase.

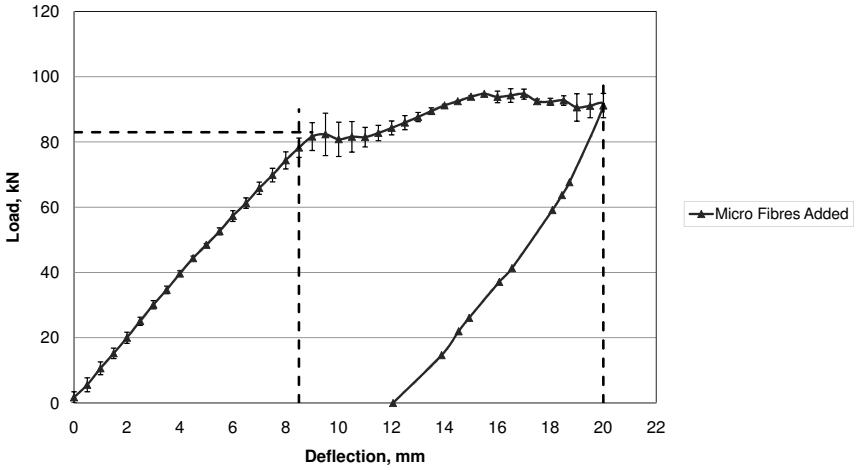

Figure 6.11: Plot showing the load deflection relationship for micro synthetic fibrous beams. Error bars are added to illustrate the reduced spread of the data in comparison to the non-fibrous beams.

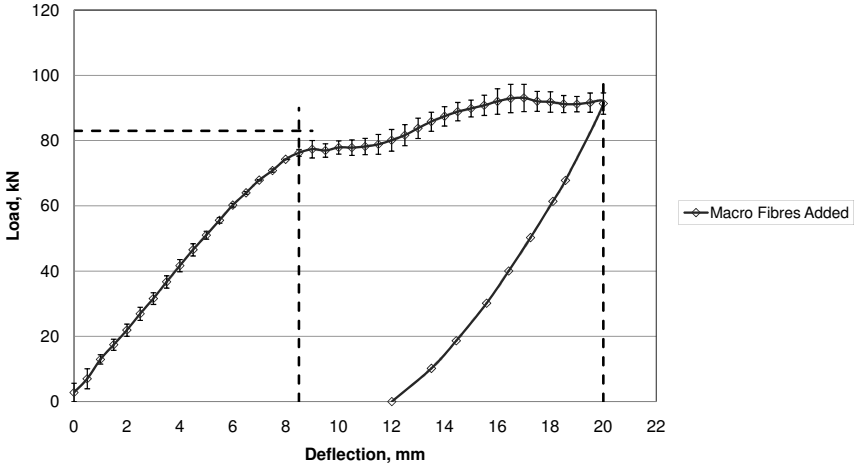

Figure 6.12: plot showing the load deflection relationship for macro synthetic fibrous beams. Error bars are added to illustrate the reduced spread of the data in comparison to the non-fibrous beams.

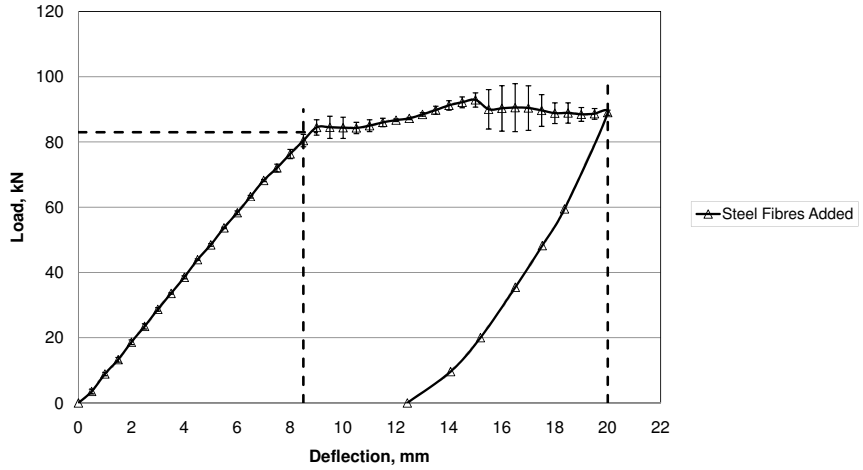

Figure 6.13: Plot showing the load deflection relationship for steel fibrous beams. Error bars are added to illustrate the reduced spread of the data in comparison to the non-fibrous beams.

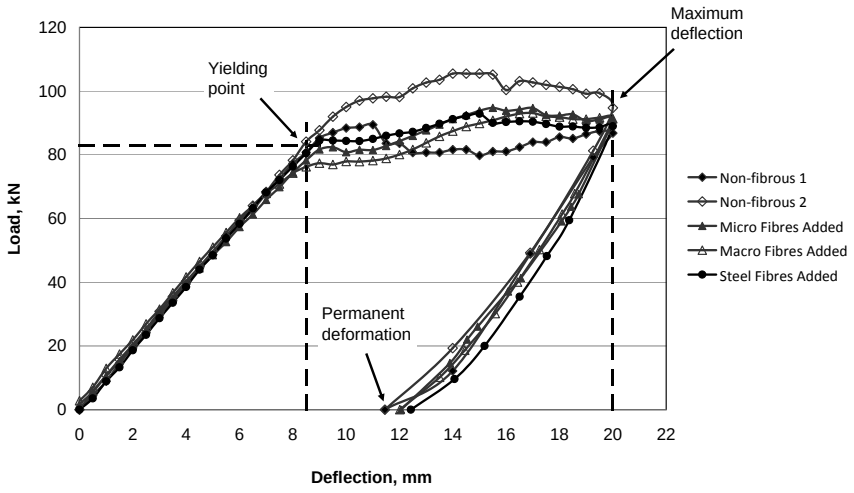

Figure 6.14: Plot showing the load deflection relationship comparison for a non-fibrous and fibrous beams. This graphically illustrates that the elastic stiffness of the beams do not vary greatly.

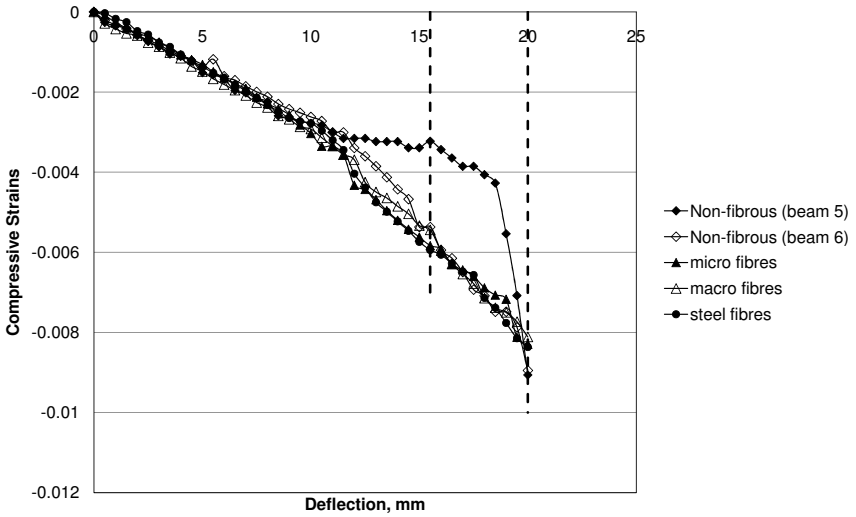

Figure 6.15: Plot showing a comparison of the compressive strains produced within non-fibrous and fibrous beams.

6.4.2 Thermal profile comparison

Initially it must be determined whether the addition of fibres has any significant effect on the thermal propagation through the reinforced concrete beams. This was done by subjecting each type of beam to the same thermal load as defined in Section 6.3.1 and comparing the thermal profiles obtained. It can be seen from Fig. 6.16 that there was no significant difference in the thermal profiles obtained regardless of fibre content (up to the dosages defined in Section 6.3.3).

As the fibre content does not significantly affect the thermal propagation through an undamaged or intact concrete member, the following results and comparisons will be carried out for the thermal variation along the length of the compression reinforcement within the heated zone. This was done as the reinforcement is the location of particular interest for the fire resistance of a member.

Fig. 6.17 illustrates the thermal profile along the compression reinforcement for beam 5 (i.e. the non-fibrous beam where the cover had been removed through the action of mechanical loading). This quite clearly showed that thermocouples situated

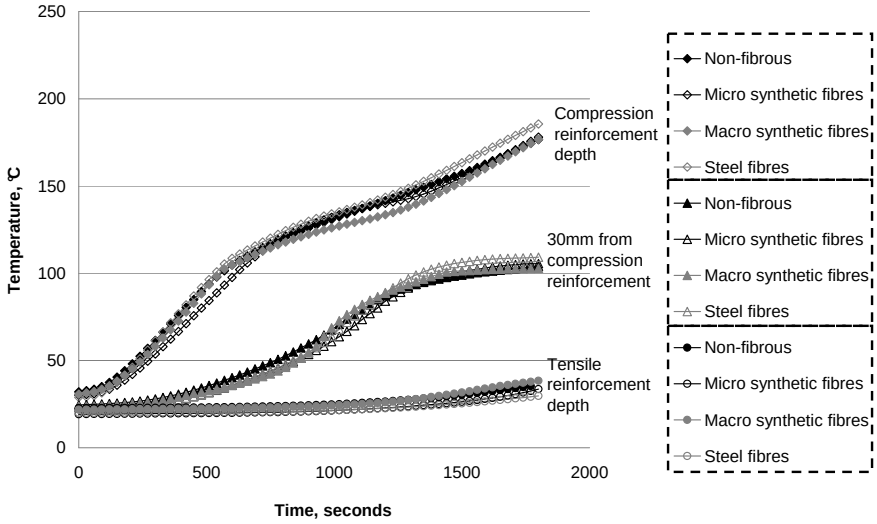

Figure 6.16: Plot of the thermal profiles produced within the thermal control specimens (see Table 6.1. Illustrating that the addition of fibres does not significantly affect the thermal propagation through a section.

in the region of the decreased cover (Fig. 6.9) recorded temperatures that, from time zero, rose much more quickly, reaching temperatures in the region of 215^{o}C to 230^{o}C in comparison to 180^{o}C which was achieved in the regions where the cover remained. This clearly coincides with the fact that the less cover provided, the higher the temperatures at the reinforcement.

When beam 6 (i.e. non-fibrous beam where crushing occurred but with no loss of cover during the mechanical loading) was subjected to the same thermal load the temperature profile along the compression reinforcement could initially be said to be increasing uniformly. However, at approximately 1170 seconds (19.5 minutes) into the heating phase, a portion of the compressive cover became removed from the beam (see Fig. 6.18). As a result and as shown in Fig. 6.19, there was a distinct and significant increase in the rate of heating of the reinforcement in the region where the cover became removed.

This demonstrated that even if the cover remained attached after a mechanically extreme loading, it became more susceptible to removal through subsequent thermal

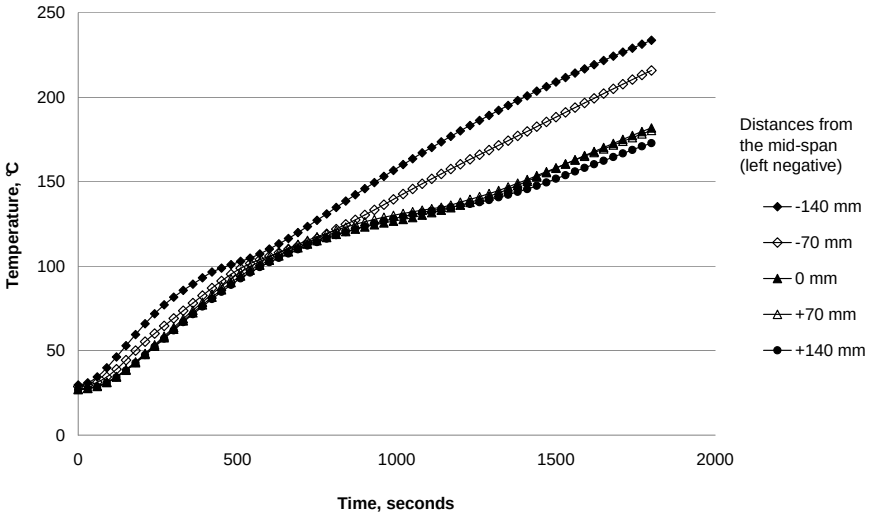

Figure 6.17: Plot of the thermal profile along the compression reinforcement of beam 5 (loss of cover occurred during mechanical loading). Illustrating the increased temperatures where the loss of cover occurred.

actions. It is clear that a method is required to prevent this loss of cover even if the specimen is damaged prior to a thermal load.

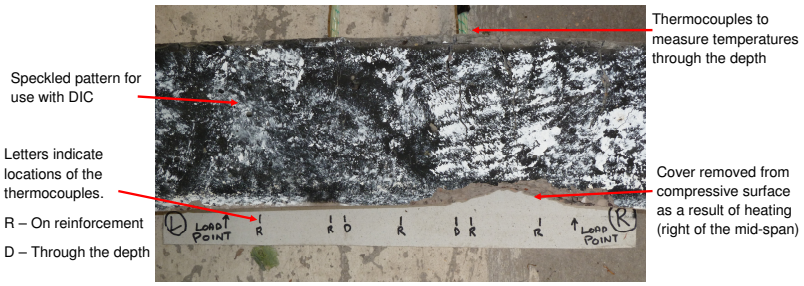

Figure 6.18: Photo: Illustrating the loss of cover in beam 6 (cover lost during thermal loading)

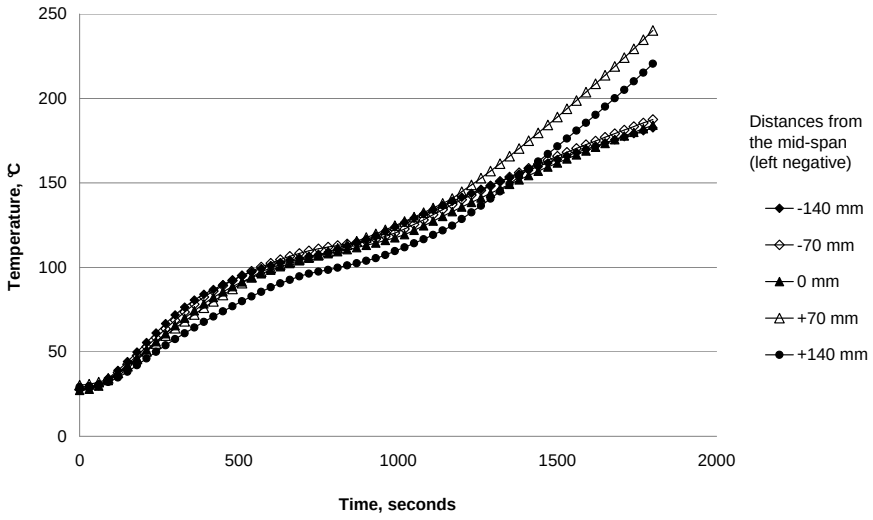

Figure 6.19: Plot of the thermal profile along the compression reinforcement of beam 5 (loss of cover occurred during mechanical loading). Illustrating the increased rate of heating at 1170 seconds where the loss of cover occurred.

The images in Fig. 6.20 to Fig. 6.22 show the state of the various fibrous beams after the mechanical loading and before the thermal loading has been applied. It can be seen that for all fibrous beams, the majority of the compressive cover remained intact and attached to the main body. However, it was clear that the different fibres used provide different degrees of effectiveness in preventing the loss of cover.

The micro synthetic fibre mix provided the best resistance to the loss of cover. This is due to the uniform dispersion of the fibres throughout the mix, making it more homogeneous, leading to the compressive stresses being spread more evenly over the surface rather than localising in a region of weakness. The fine interlacing of the fibres within the concrete also means that the fibres creates a "web" that provides a mechanism of anchoring the concrete cover to the core of the member, therefore preventing the loss of cover.

The macro synthetic fibres also made the concrete mix more homogeneous, and so, such like the micro synthetic fibres, the compressive stresses were spread more evenly over the surface rather than localising in a region of weakness. The macro synthetic fibres were also longer than the micro counterpart, therefore providing a better anchorage length into the core of the beam. However, due to the dispersing of the macro synthetic fibres, the spacing between each fibre is greater, leading to small areas of the concrete that will remain unaffected by the fibres and consequently are susceptible to removal through the action of mechanical load (see Fig. 6.21).

The steel fibre mix did not perform as well under mechanical loading as either of the synthetic fibre types. Although the steel fibres, like the synthetic fibres, made the mix more homogeneous, the reduction in performance is due to the combination of the spacing between the fibres (see above) and the relative increase in stiffness of the steel fibres. As compressive stresses were induced in the concrete cover, the steel fibres were more resistant to bending than the synthetic fibres. Therefore, the steel fibres have a tendency to displace as a whole body rather than bend to accommodate the compression. As a result, this whole body movement of the fibres will cause the concrete to become weaker and more susceptible to removal.

Figure 6.20: Photo: Beam of mix with micro synthetic fibres after mechanical and thermal loading. Shows a small amount of compression damage but no loss of concrete cover is sustained.

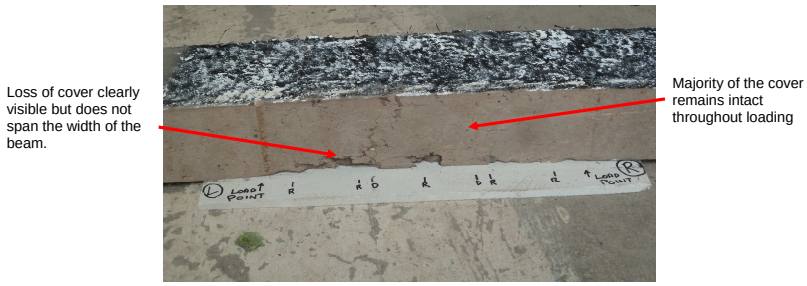

Figure 6.21: Photo: Beam of mix with macro synthetic fibres after mechanical and thermal loading. Shows some compression damage and only a little amount of concrete cover loss is sustained.

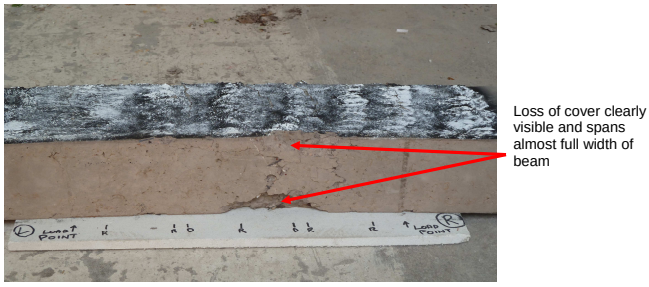

Figure 6.22: Photo: Beam of mix with steel fibres after mechanical and thermal loading. Clearly shows compression damage and loss of concrete cover is sustained but not as much as with non-fibrous beams.

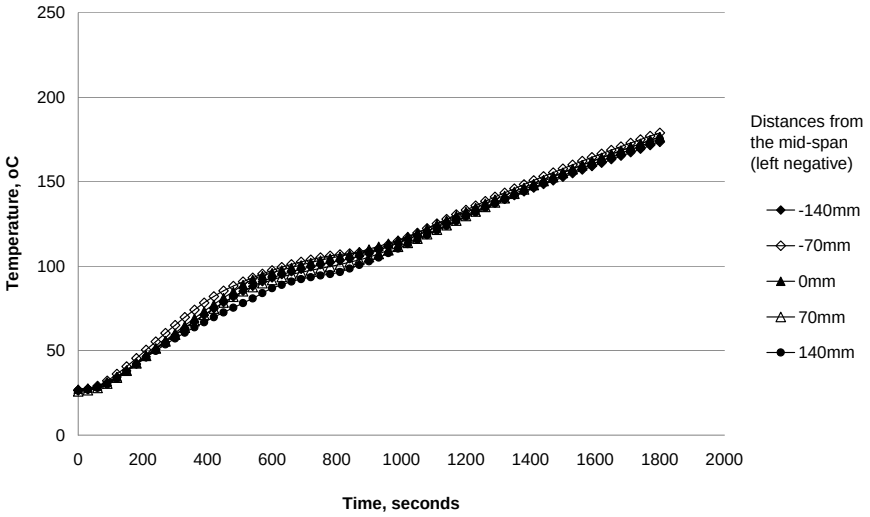

Figure 6.23: Plot of the thermal profile of the beams of mix with micro synthetic fibres. Illustrating that the thermal resistance is sustained.

Fig. 6.23 to Fig. 6.25 plot the thermal profiles along the compression reinforcement for the various fibrous beams. It can clearly be seen that all the fibrous members maintained a good thermal resistance throughout the thermal loading where the profiles closely resembled the profile of the thermal controls. The temperatures within the concrete cover were greater than 180^oC. At these temperatures the steel fibres will remain broadly unaffected whereas the synthetic fibres (with a melting point of 160^oC) melt. However, none of the fibrous members exhibited further loss of cover as a result of the thermal loading which can be attributed to a couple of mechanisms. Firstly, the region of crushed concrete will exhibit an increase in air voids that will allow for the escape of increasing vapour pressure as the temperatures increase. Secondly, as the fibres provided a more homogeneous mix, no localised region of weakness occurred and as a result enabled the concrete to maintain a greater proportion of its tensile strength and aggregate interlock after mechanical loading. It is this relative increase in maintained tensile strength, aggregate interlock and porosity that aided the concrete member to retain the concrete cover and hence retain the thermal resistance.

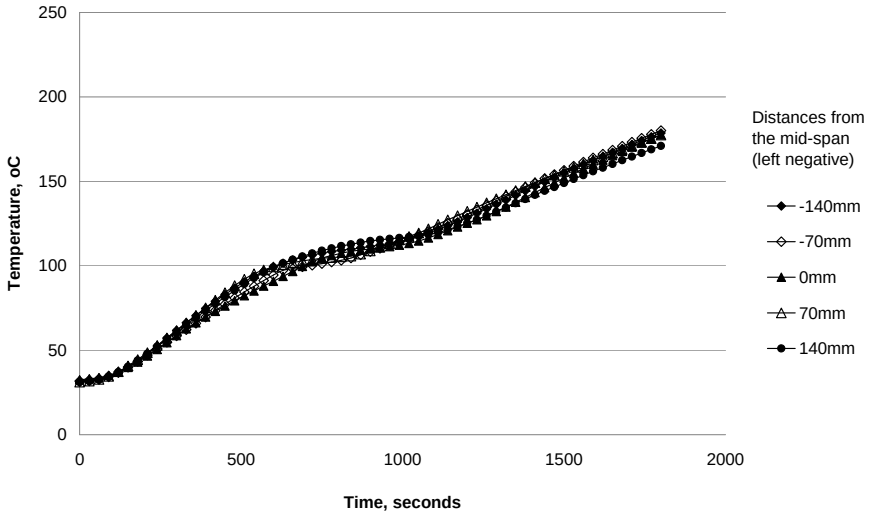

Figure 6.24: Plot of the thermal profile of the beams of mix with macro synthetic fibre. Illustrating that the thermal resistance is sustained.

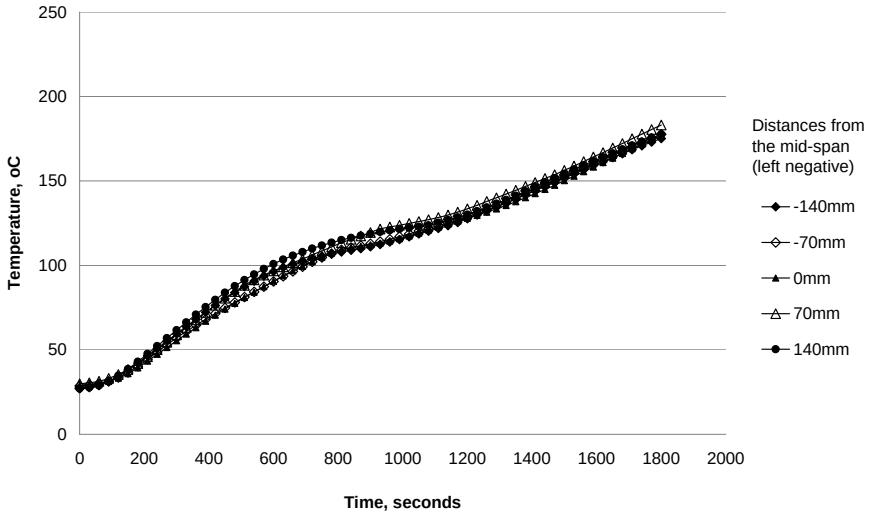

Figure 6.25: Plot of the thermal profile of the beams of mix with steel fibre. Illustrating that the thermal resistance is sustained.

6.5 Conclusions

The main conclusion of this investigation is that the addition of fibres significantly increased the cohesiveness of mechcanically crushed concrete throughout a thermally extreme event.

The addition of fibres increased the homogeneity of the concrete mix and, as a result, the compressive strains induced were more spread rather than localising in a small region as is the case for the non-fibrous members. This trait meant that the compressive strains at a given point within the fibrous members may not be as great as within a non-fibrous member. As a result, fibrous members are less susceptible to a loss of the concrete cover under mechanical loading. The increased homogeneity of the mix and reduction in localised failure allowed the fibrous concrete member to retain a proportion of the aggregate interlock, hence increasing the integrity of the concrete cover. Therefore, in spite of the notable drawback of the synthetic fibres melting at a relatively low temperature, the inclusion of the fibres enhances the aggregate interlock of the concrete throughout the mechanical loading which in turn helps the integrity of the cover when subjected to a thermal load.

Through this investigation it has been shown that the use of fibres to increase cohesiveness of a concrete member under a mechanically extreme event and a subsequent thermal event was significantly beneficial. The stability and integrity of the member was increased and, with a reduced loss of concrete cover, came an improved thermal resistance in comparison to a non-fibrous counterpart.

From Fig. 6.20 to Fig. 6.22 it can be seen that the beam with the micro synthetic fibres performed the best with the least cover lost, although all fibrous members enhanced the integrity of the concrete cover on a reinforced concrete member subjected to multiple extreme loads.

This information is particularly relevant for numerical simulations as it means that performing full 3-D simulations, that is currently required to capture the effects of concrete cover loss, may not be required. Enhancing the integrity of and designing

to retain the concrete cover under multiple and sequential extreme events allows for computational analysis of global structues to be completed much more simply through the use of 1-D elements.

Chapter 7

Conclusions

In this thesis the behaviour of reinforced concrete members and structures subjected to excessive mechanical and thermal loads has been investigated. The work has been focused on geometrical phenomena such as tensile cracking and concrete cover loss, with particular reference to the coupling of these effects to the thermal and thermo-mechanical behaviour. In addition, a method is proposed to eliminate or reduce these effects and to increase the stability and integrity of the concrete throughout mechanically extreme and thermally extreme events, even when these events happen sequentially.

Preliminary investigations were carried out into the inconsistancies within the design of reinforced concrete structures under a variety of extreme mechanical and thermal loads. The design for thermal loads is accomplished under the main assumption that the concrete cover is present and remains intact throughout. This is in direct contradiction to the design philosophy undertaken for reinforced concrete structures subjected to extreme mechanical loads, where there is an allowable level of damage the structure can endure with the aim of dissipating the kinetic energy.

These preliminary investigations clearly demonstrated the fundamental and major inconsistencies between the design philosophies. Indeed, considering the scenario where there is a fire following another extreme event, the thermal resistance design may become unreliable. The following presents the key conclusions from the research presented in this thesis.

7.1 Specific conclusions to the research

7.1.1 Tensile cracking

Tensile cracking is one of the main geometrical phenomenon that occurs within reinforced concrete structures when subjected to excessive loading. An experimental programme was undertaken to investigate this phenomenon and its effect on the thermal propagation through a section. From this several conclusions were drawn:

1. The main conclusion of this research was that there was no significant change detected in the thermal propagation through the tensile cracks of a concrete member where the cracks are up to the order of 10^1mm at the heated surface.

2. Although no significant change occurred in the thermal propagation, temperatures do in fact indicate a minor increase when the concrete becomes cracked. This is most likely due to small geometrical and concrete compositional differences.

3. During the design calculation of the thermal profiles through a section, it is not required to take tensile strain or crack widths into account.

4. In particular reference to numerical simulations, this information means that performing a thermal and then a mechanical analysis of heated structures sequentially, as is typically undertaken currently, remains a valid approach and a fully coupled analysis is not required.

5. It may be noted for further experimental investigations that the tensile cracking magnitude and pattern is not affected by the placement of the thermocouples, provided that they are orientated in a direction parallel to the crack progression.

6. The mechanism of convection was not explicity taken account of within this experimental programme. Therefore, this mechanism still needs to be studied in detail to fully understand the magnitude of its implications.

7.1.2 Loss of concrete cover

The loss of concrete cover was numerically investigated and its effect on the thermo-mechanical behaviour of a reinforced concrete frame studied. A new technique was created to simulate geometrical effects and was used for the automatic calculation of this concrete cover loss. The conclusions that were obtained from this investigation were:

1. The loss of a small proportion of concrete cover had a profound effect on the thermal profiles and thermo-mechanical behaviour of a reinforced concrete frame.

2. Loss of cover around the beam-column connections caused the greatest variation in behaviour. This was due to the reduction in rotational stiffness leading to a more flexible structure, meaning that the location of cover loss was extremely important.

3. Adoption of the automatic cover loss calculation technique allowed the user to apply a variety of mechanical loading scenarios with a subsequent variety of thermal loads without having to manually remove elements or manually alter the material properties to simulate the loss of concrete cover. This resulted in a significantly increased speed of the simulation.

4. However, the criterion used to define the loss of cover needs further investigation to encompass different variables such as a range of concrete strengths, different concrete cover depths and under increasing temperatures.

7.1.3 Fibre implementation

It was clear that a method was required to increase the integrity and stability of the concrete cover to avoid its loss. To achieve this, an experimental investigation was carried out using uniformly distributed fibres embedded within the concrete. Several conclusions were drawn from this research:

1. The addition of fibres does not significantly affect the initial elastic stiffness of the specimens nor does it significantly affect the ultimate tensile strength, but the addition of the fibres was shown to cause a slight decrease in the ultimate compressive strength.

2. The addition of fibres into the concrete mix significantly increased the cohesiveness of the crushed concrete member through both mechanically and thermally extreme events, resulting in little to no cover loss.

3. The use of fibres resulted in a more homogeneous mix and, therefore, induced compressive strains were more widespread rather than localising in a small region as was the case for the non-fibrous members.

4. The melting of the synthetic fibres does not have an adverse effect. During the mechanical loading, the fibres helped retain a portion of the concrete's tensile strength and aggregate interlock, which in turn resisted the thermal induced strains even when the fibres had melted and lost all strength.

7.2 General discussion and conclusions

The conclusions above are directly related to the individual investigations undertaken throughout this thesis. However, there are more general conclusions that can be drawn from this research which are further discussed below.

It is clear that the prediction of the behaviour of a reinforced concrete frame requires an in-depth understanding and application of the material properties. However, the behaviour of reinforced concrete not only depends on the material properties but also on the geometrical phenomena that can occur during extreme loading events.

In this thesis, it has been shown through experimentation, that tensile cracking does not significantly affect the thermal propagation and therefore does not significantly affect the thermal resistance. However, on the other hand, it has been shown that the loss of the concrete cover not only has a profound effect on both the thermal propagation and thermo-mechanical performance of a reinforced concrete frame, but also affects the ultimate strength of the frame at high horizontal deformations. Therefore, to completely capture the structural behaviour of a reinforced concrete frame, it is essential to explicitly take account of the loss of concrete cover.

The technique detailed in Chapter 4 has shown that these geometrical effects can be explicitly simulated by altering material properties to conform to a set of criterion, without directly changing the geometry of the model. Although this technique has solely been used to simulate the loss of concrete cover, it also has the potential to be programmed to simulate the effect of thermal spalling by including temperature and tension strain parameters. However, to use this technique to accurately model these geometrical effects, it is necessary to generate the numerical model completely in three dimensions as discussed in Appendix H. This quickly becomes computationally uneconomical due to the very large number of elements needed when considering a full scale building. For example, the frame simulated in Chapter 5 is only a relatively small section of the full structure, yet it took over two weeks to complete one full simulation while utilizing 8 (2.6GHz) processors running in parallel. Therefore, although this re-

search has clearly shown that the geometrical effects brought about by extreme loading scenarios have a profound effect on the mechanical, thermal and thermo-mechanical behaviour of a reinforced concrete structure, it is uneconomical to explicitly model them.

In order to bypass the need for explicitly modelling these geometrical effects, it is suggested that the overall integrity of the concrete is enhanced, which in this research, has been achieved by the use of uniformly distributed embedded fibres in the concrete mix. Through the use of a fibrous mix, it is possible to reduce or eliminate these geometrical effects. For instance, the addition of fibres into a concrete mix, as performed in Chapter 6, led to the mix being more homogeneous. This, in turn, resulted in a reduced localization of tensile cracks and compressive strains leading to the overall enhanced integrity and stability of the concrete cover and structure. This ability adds to the already mounting and compelling reasons, which include spalling prevention as discussed in Chapter 6, for the use of a fibre reinforced concrete mix over a non-fibrous mix.

Therefore, a significant finding of this research is that the use of uniformly distributed embedded fibres into the concrete mix clearly enhances the the overall mechanical, thermal and thermo-mechanical behaviour of reinforced concrete subjected to mutilple and sequential extreme loading conditions.

7.3 Further Work

Although, it has been concluded that tensile cracks do not significantly affect the thermal propagation, these cracks were of the order of 10^1mm at the heated surface. Therefore, further research may be required into the limits of the crack widths in which the radiation and buoyancy effects become more dominant.

The technique detailed in Chapter 5 for the simulation of loss of concrete cover also has the potential to encompass further geometrical effects such as tensile cracking and

thermal spalling and how these affect the mechanical and thermal behaviour. However, for this to be possible the addition of further experimental data on the crushing strains, cover loss strains and pore pressure calculation are required to develop suitable criteria.

The research presented in Chapter 6 provides a small glimpse of what fibrous concrete can achieve. However, further research would be required into the areas of:

1. - fibre types, to include carbon fibre as an alternative to steel or polypropylene,

2. - fibre dosages required to provide an adequate increase in cohesion of the concrete.

3. - location of the fibres within the member as they are only required within the concrete cover.

References

Ali, F., 2002. Is high strength concrete more susceptible to explosive spalling than normal strength concrete in fire? Fire and Materials 26, 127 – 130.

Anderberg, Y., 1988. Modelling steel behaviour. Fire Safety Journal 21, 17 – 26.

Bagchi, A., Kodur, V. K. R., Mousavi, S., 2008. A review of post-earthquake fire hazard to building structures. Canadian Journal of Civil Engineering 35 (7), 689 – 698.

Beeby, A. W., Scott, R. H., 2005. Cracking and deformation of axially reinforced members subjeced to pure tension. Magazine of Concrete Research 57 (10), 611 – 621.

Biolzi, L., Cattaneo, S., Rosati, G., 2008. Evaluating residual properties of thermally damaged concrete. Cement and Concrete Composites 30, 907 – 916.

Bisby, L. A., Take, W. A., 2009. Strain localizations in frp confined concrete: New insights. Structures and Buildings 162 (5), 301–309.

Bratina, S., Cas, B., Saje, M., Planinc, I., 2005. Numerical modelling of behaviour of reinforced concrete columns in fire and comparison with eurocode 2. International Journal of Solids and Structures 42, 5715–5733.

BSI, 2000a. Cement. composition, specifications and conformity criteria for common cements (amd 15209) (amd 17352) (bs en 197-1:2000).

BSI, 2000b. Testing hardened concrete. tensile splitting strength of test specimens(bs en 12390-6:2000).

BSI, 2002. Testing hardened concrete. compressive strength of test specimens (bs en 12390-3:2002).

BSI, 2009. Testing fresh concrete. slump-test (bs en 12350-2:2009).

REFERENCES

Buchanan, A. H., 2001. Structural Design for Fire Safety 1st Edition. John Wiley & Sons Ltd.

Cooke, G. M. E., 1988. An introduction to the mechanical properties of structural steel at elevated temperatures. Fire Safety Journal 13, 45 – 54.

Cosenza, E., Manfredi, G., 2000. Damage indices and damage measures. Progress in Structural Engineering and Materials 5, 50 – 59.

D'Ambrisi, A., Filippou, F. C., 1999. Modelling of cyclic shear behaviour in rc members. Journal of structural engineering 125, 1143 – 1150.

Deeny, S., 2010. The implications of compartment fire non-uniformity for the membrane action of reinforced concrete slabs. Ph.D. thesis, University of Edinburgh.

Duan, K., Hu, X. Z., Wittmann, F. H., March 2003. Size effect on fracture energy resistance and fracture energy of concrete. Materials and Structures 36, 74 – 80.

Elghazouli, A. Y., Cashell, K. A., Izzuddin, B. A., 2009. Experimental evaluation of the mechanical properties of steel reinforcement at elevated temperature. Fire Safety Journal 44, 909 919.

Eurocode, 2004. Eurocode 2: Design of concrete structures - part 1-2:general - structural fire design.

Eurocode, 2005. Eurocode 1: Actions on structures part 1-1: General actions densities, self-weight and imposed loads.

Feenstra, P. H., de Borst, R., 1995. Constitutive model for reinforced concrete. Journal of Engineering Mechanics 121 (5), 587 – 595.

Guo, X. H., Gilbert, R. I., 2000. The effect of specimen size on the fracture energy and softening function of concrete. Materials and Structures 33, 309 – 316.

Haddad, R. H., Al-Saleh, R. J., Al-Akhras, N. M., 2008. Effect of elevated temperature on bond between steel reinforcement and fiber reinforced concrete. Fire Safety Journal 43, 334 – 343.

Harder, N. A., 1992. Brittleness, fracture energy and size effect in theory and in reality. Materials and Structures 25, 102–106.

Hertz, K. D., 2003. Limits of spalling of fire-exposed concrete. Fire Safety Journal 38, 103 – 116.

Hillerborg, A., Modeer, M., Petersson, P. E., 1976. Analysis of crack formation and crack growth in concrete by means of fracture mechanics and finite elements. Cement and Concrete Research 6, 773 – 782.

Holberg, S., Anderberg, Y., 1993. Computer simulations and design method for fire-exposed concrete columns. Tech. rep., Swedish Fire Research Board, S-115 87 STOCKHOLM, research Park, Ideon, Lund.

Kappos, A. J., 1997. Seismic damage indices for rc buildings. Progress in Structural Engineering and Materials 1 (1), 78 – 87.

Karsan, I. D., Jirsa, J. O., 1969. Behaviour of comncrete under compressive loadings. Journal of the Structural Division, ASCE 95, 1519 – 1526.

Khoury, G., 2000. Effect of fire on concrete and concrete structures. Progress in Structural Engineering and Materials 2 (4), 429 – 447.

Khoury, G. A., 2006. Strain of heated concrete during two thermal cycles. part 1: strain over two cycles, during first heating and at subsequent constant temperature. Magazine of Concrete Research 58, 367 – 385.

Khoury, G. A., 2008. Polypropylene fibres in heated concrete part 2: Pressure relief mechanisms and modelling criteria. Magazine of Concrete Research 60 (3), 189 – 204.

Kim, K. H., Jeon, S. E., Kim, J. K., Yang, S., 2003. An experimental study on thermal conductivity of concrete. Cement and Concrete Research 33, 363 – 371.

Kirby, B. B., Preston, R. R., 1988. High temperature properties of hot-rolled, structural steels for use in fire engineering design studies. Fire Safety Journal 13, 27 – 37.

Kodour, V. K. R., Dwaikat, M., 2007. Performance-based fire safety design of reinforced concrete beams. Journal of Fire Protection Engineering 17, 293 – 320.

Kodur, V. F., Dwaikat, M., Fike, R., 2010. High-temperature properties of steel for fire resistance modeling of structures. Journal of Materials in Civil Engineering 22 (5), 423 – 434.

Kong, K. L., Beeby, A. W., Forth, J. P., Scott, R. H., 2007. Cracking and tension zone behaviour in rc flexural members. Structures & Buildings 160 (SB3), 165 – 172.

Lam, Y. Y., 1980. Behaviour of plain concrete under cyclic compressive loading. Master's thesis, Massachusetts Institute of Technology.

Law, A., 2010. The assessment and response of concrete structures subject to fire. Ph.D. thesis, University of Edinburgh.

Lee, J., Fenves, G. L., 1998a. A plastic-damage concrete model for earthquake analysis of dams. Earthquake Engineering and Structural Dynamics 27, 937 – 956.

Lee, J., Fenves, G. L., 1998b. Plastic-damage model for cyclic loading of concrete structures. Journal of Engineering Mechanics 124 (8), 892 – 900.

Legeron, F., Paultre, P., Mazars, J., 2005. Damage mechanics modelling of nonlinear seismic behaviour of concrete structures. Journal of Structural Engineering 131 (6), 946 – 955.

Lie, T. T., Kodur, V. K. R., 1995. Thermal properties of fibre-reinforced concrete at elevated temperatures. Tech. rep., National Research Conuncil Canada.

Long-yuan, L., Purkiss, J., 2005. Stress-strain constitutive equations of concrete at elevated temperatures. Fire Safety Journal 40 (7), 669 – 686.

Naus, D. J., 2006. Effects of elevated temperature on high-strength concrete materials and structures. US Nuclear Regulatory Commission.

Neville, A. M., 1996. Properties of Concrete. Addison Wesley Longman Limited.

Outinen, J., Makelainen, P., 2002. Mechanical properties of structrual steel at elevated temperatures and after cooling down. In: Second International Workshop, Structures in Fire - Christchurch.

Pankaj, P., 1990. Finite element analysis in strain softening and localisation problems. Ph.D. thesis, University of Roorkee, Roorkee.

Pankaj, P., Knox, J. J., Usmani, A. S., 2008. The behaviour of pre-damaged reinforced concrete structural systems in fire. In: The 14th World Conference on Earthquake Engineering, Beijing, China.

Petkovski, M., 2010. Effects of stress during heating on strength and stiffness of concrete at elevated temperature. Cement and Concrete Research 40, 1744 – 1755.

Petkovski, M., Crouch, R. S., 2008. Strains under transient hygro-thermal states in concrete loaded in multiaxial compression and heated to 250 c. Cement and Concrete Research 38, 586 – 596.

Scawthorn, C., M., E. J., Schiff, A. J., 2005. Fire Following Earthquake. ASCE publications.

Shi, X., Tan, T.-H., Tan, K.-H., Guo, Z., 2004. Influence of concrete cover on the fire resistance of reinforced concrete flexural members. Journal of Structural Engineering 130 (8), 1225 – 1234.

Sideris, K. K., Manita, P., Chaniotakis, E., 2009. Performance of thermally damaged fibre reinforced concretes. Construction and Building Materials 23, 1232 – 1239.

Spacone, E., Ciampi, V., Filippou, F. C., 1992. A beam element for seismic damage analysis. Master's thesis, University of California, Berkeley.

Standard, I., 2002. Criteria for earthquake resistant design of structures: Part 1 general provisions and buildings.

Tanyildizi, H., Coskun, A., Somunkiran, I., 2008. An experimental investigation of bond and compressive strength of concrete with mineral admixtures at high temperatures. The Arabain Journal for Science and Engineering 33, 443 – 449.

Teychenne, D. C., Franklin, R. E., Erntroy, H. C., 1988. Design of normal concrete mixes, second edition. Building Research Establishment.

Trunk, B., Wittmann, F. H., 2001. Influence of size of fracture energy of concrete. Materials and Structures 34, 260 – 265.

Twilt, L., 1988. Strength and deformations properties of steel at eleveated temperatures: Some practical implications. Fire Safety Journal 13, 9 –15.

van der Heijden, G. H. A., van Bijnen, R. M. W., Pel, L., Huinink, H. P., 2007. Moisture transport in heated concrete, as studied by nmr, and its consequences for fire spalling. Cement and Concrete Research 37, 894 – 901.

Vejmelkov, E., Padevet, P., Cerny, R., 2008. Effect of cracks on hygric and thermal characteristics of concrete. Bauphysik 30 (6), 438 – 444.

Wan, S., Loh, C. H., Peng, S. Y., 2001. Experimental and theoretical study on softening and pinching effects of bridge column. Soil dynamics and earthquake engineering 21, 75 – 81.

White, D., Take, W., Bolton, M., 2003. Soil deformation measurement using particle image velocimetry (piv) and photogrammetry. Geotechnique 53 (7), 619 – 631.

Wittmann, F. H., 2002. Crack formation and fracture energy of normal and high strength concrete. Sadhana 27 (4), 413–423.

Zollo, R. F., 1997. Fibre-reinforced concrete: an overview after 30 years of development. Cement and Concrete Composites 19, 107 – 122.

Appendices

Appendix A

Concrete mix for use in experimentation

The concrete mix specified in this appendix is designed to be of normal strength concrete of 35kN/m^2. It has been designed using the "Design for normal concrete mixes" (1988), therefore all figure and table names and references with the following tables are referring to this document. Samples of both the coarse and fine aggregates were taken and weighed. The samples were then placed in an oven set at 90^{o}C for 24 hours to remove all the water from the sample. The samples were then weighed again to determine the amount of water held within the aggregates. It was calculated that the water content of the coarse and fine aggregates 3.68% and 7.96% respectively. Assuming that the coarse aggregate retains 1% of the moisture and the fine aggregate retains 2.15% of the moisture, the concrete component volumes were adjusted and recorded in Table. A.3. This mix is used for both experimenal investigations detailed in Chapter 3 and Chapter 6 with the only difference being the change in volume of water added to account for the absorbsion of the synthetic fibres as detailed in Appendix B.

Table A.1: Details of the concrete mix design used for Chapter 3 and Chapter 4.

Stage	Item	Reference or Calculation	Values
1	1.1 Characteristic strength	Specified	35 N/mm^2 at 28 days with 5% defective
	1.2 Standard deviation	Fig 3	8 N/mm^2
	1.3 Margin	C1	(k = 1.64): 1.64 * 8 = 13.12 N/mm^2
	1.4 Target mean strength	c2	13.12 + 35 = 48.12 N/mm^2
	1.5 Cement class		42.5/~~52.5~~
	1.6 Aggregate type		~~crushed~~/uncrushed
	1.7 Free-water/cement ratio	Table 2 Fig 4	0.45
2	2.1 Slump or Vebe time	Specified	30-60 mm
	2.2 Maximum aggregate size	Specified	10 mm
	2.3 Free-water content	Table 3	205 kg/m^3
3	3.1 Cement content	C3	205 / 0.45 = 455.56 kg/m^3
	3.2 Maximum cement content	Specified	N/A
	3.3 Minimum cement content	Specified	N/A
4	4.1 Relative density of aggregate	(SSD)	2.6 ~~known~~/assumed
	4.2 Concrete density	Fig 5	2335 kg/m^3
	4.3 Total aggregate concrete	C4	2335 - 456 - 205 = 1674 kg/m^3
5	5.1 Grading of fine aggregate	% passing 600μm	80%
	5.2 Proportion of fine aggregate	Fig 6	35%
	5.3 Fine aggregate content	C5	1674 * 0.35 = 585.9 kg/m^3
	5.4 Course aggregate content	C5	1674 - 585.9 = 1088.1 kg/m^3

Table A.2: Summary of the concrete mix design based on above table only.

Quantities	Cement (kg)	Course aggregate (kg)	Fine aggregate (kg)	Water (kg)
per m^3	455	1090	585	205
per trial mix of 0.37 m^3	16.835	40.33	21.645	7.585

Table A.3: Summary of the concrete mix design used for Chapter 3 and Chapter 4 taking into account the moisture given by the aggregates.

Quantities	Cement (kg)	Course aggregate (kg)	Fine aggregate (kg)	Water (kg)
per m^3	455	1129.73	635.14	137.84
per trial mix of 0.37 m^3	16.835	40.33	21.645	7.585

Appendix B

Water absorption of synthetic fibres

The addition of fibres into a concrete mix reduces the workability by two mechanisms. The first mechanism is by increasing the stiffness of the fresh concrete. The second mechanism, which is more relevant with synthetic fibres, is that the fibres will absorb some of the free water added to the mix. In this appendix the absorption of the synthetic fibres is calculated and the the free water added to the mixture is altered to accommodate this absorption.

Initially 1kg of distilled water is added to 50g of each type of synthetic fibre. The fibres were then left submerged for 24 hours, after which they were removed and sieved out of the water. The fibres were also shaken while in the sieve to remove any small pockets of water trapped between fibres. The mass of the fibres and the remaining water were then measured and recorded in Table. B.1.

Table B.1: Details of the water absorption of synthetic fibres (i.e. micro and macro as defined in Chapter 6.

	Micro fibres	Macro fibres
Initial mass (kg)	0.05	0.05
Final mass (kg)	0.2344	0.0766
Mass gained (kg)	0.1844	0.0266
Mass of fibres in mix (kg/m^3)	2	3.06
Additional water added (kg)	7.376	1.532

Appendix C

Thermocouple placement techniques

The precise placement of thermocouples can be extremely sensitive when dealing with concrete. Obstacles brought about by the aggregate and the forces that indicatively occur during the settlement of the concrete can cause precise placement of the thermocouples to be influenced. The following describes the methods used to place the thermocouples within the concrete specimens with the greatest accuracy.

C.1 Method one: post-casting placement

The method used for the experimental investigation into tensile cracking as carried out in chapter 3 was done by placing the thermocouples post-casting. Placing the thermocouples post-casting reduces the chances of the thermocouples placement being affected by the concrete flow and settlement during the casting. Further measures are taken to reduce the interaction of the aggregate on the thermocouples as outlined in the methodology below.

(a) Before mixing and casting, the thermocouples of each line are first twisted together into clusters and glued in place as shown in Fig. C.1. This is done to increase the strength of an individual line of thermocouples and improve the accuracy of the placement.

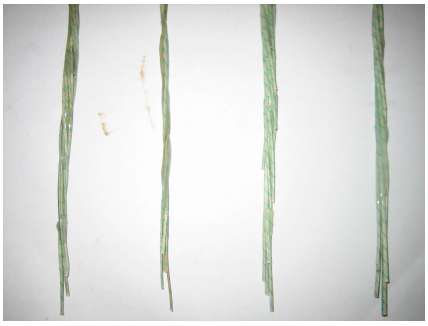

Figure C.1: Example of a thermocouple clusters.

Figure C.2: Aggregate displacement rods (ADR's).

(b) The concrete mix, as set-out in Appendix A, is then cast. Prior to the curing process, the following steps were carried out.

(c) Aggregate displacement rods (ADR's) (Fig. C.2) are pushed vertically through the wet concrete to displace any course pieces of aggregate that lie in the direct proposed path of the thermocouples.

(d) The ADR's are then completely removed (vertically).

(e) The thermocouples are strapped into place and pushed vertically through the concrete at their proposed locations and through the newly made channels (Fig. C.3).

(f) The sides of the beam mold are then lightly knocked with a 0.85kg rubber mallet 3-4 times on each of the vertical sides to allow the concrete to settle back around the thermocouples.

(g) The concrete is then allowed to cure with the thermocouples secured within.

(h) The beam is then broken out of the mold and the strapping is removed from the thermocouples to leave a specimen ready for testing (Fig. C.4.

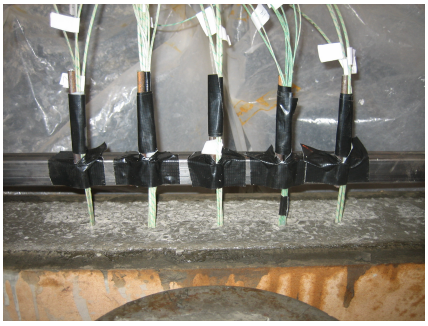

Figure C.3: Placement of the thermocouples within the wet concrete.

Figure C.4: Placement of the thermocouples within the cured concrete.

C.2 Method two: pre-casting placement

For the experimental investigation into the use of fibres to increase the cohesiveness of a concrete specimen or member as carried out in Chapter 6 two methods were adopted for the placement of the thermocouples. Placing the thermocouples throughout the depth of the beam was achieved by the first method as described in the previous section. However, placement of the thermocouples on the compressive reinforcement was carried out pre-casting of the concrete.

(a) First the thermocouples were fed along the length of each of the compression reinforcement bars to a specified longitudinal location.

(b) The end of the thermocouple is then positioned at the mid-depth of the compression reinforcement and on the inner side.

(c) Finally the thermocouple is secured to the compression reinforcement with the use of tieing wire.

(d) The concrete is then cast and allowed to cure with the thermocouples secured within.

Appendix D

Calculation of necking and rupture strains in reinforcing steel

The material properties of reinforcing steel under high strains is uncertain. Therefore, the work provided in this appendix aims to determine the strain levels at which necking or softening and rupture occurs. This investigation was carried out using 10mm deformed high tensile steel (nominal yield of 500MPa) at ambient temperatures. Four reinforcing bars were tested in tension while the axial load and elongation were measured and recorded until failure through rupture. Fig. D.1 plots the average stress-strain curve obtained from the testing of the reinforcement with error bars showing the variation between the specimens. It can be seen that the stress-strain behaviour of the reinforcement follows the generalised behaviour given in Chapter 2 where the initial yielding occurs at approximately 500N/m^2. As yielding occurs the stress increases to approximately 580N/m^2 at a strain of 0.026. When considering the original cross-sectional area, the stress is maintained until a strain of 0.1 where necking or softening of the steel reinforcement begins to occur. However, when considering the area change due to Poisson's ratio, the stress increases slightly to approximately 590N/m^2. At this point the the stress that the reinforcing bar can sustain begins to reduce and continues until the strain of 0.21 where final rupture of the reinforcement occurred where the final stress reduces from 500N/m^2 to zero.

D. CALCULATION OF NECKING AND RUPTURE STRAINS IN REINFORCING STEEL

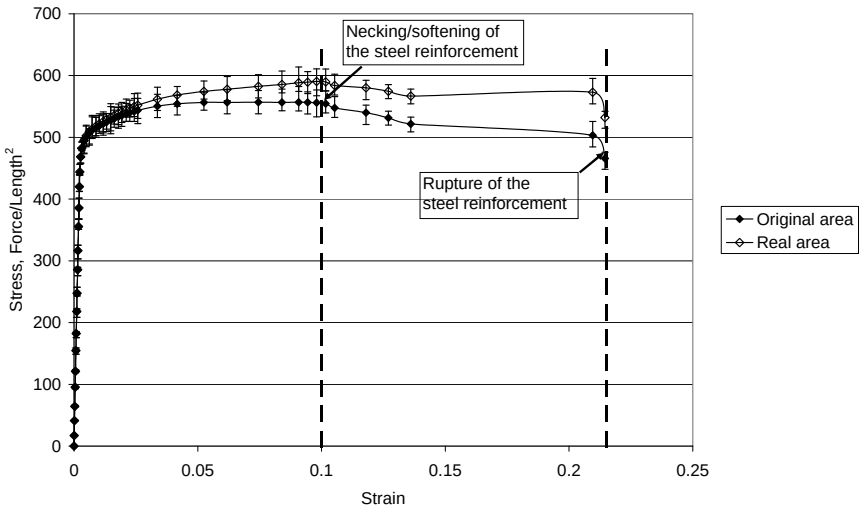

Figure D.1: Plot showing the results of an experimental investigation into the stress-strain behaviour of steel subjected to high strains at ambient temperatures. The results are calculated using the original area of the steel bars as well as taking account for the change in area due to Poisson's ratio. It is clear that for 10mmϕ bars the stress-strain behaviour does change. However, this behaviour is not hugely significant for numerical inputs.

Table D.1: Tabulated summary of the stress-strain relationship of steel at ambient temperature for calculations using both original area of the bar and the modified or real area of the bar.

Stress N/m^2(original area)	Stress N/m^2(real area)	Strain
0	0	
500	500	0.003
560	575	0.05
560	590	0.1
500	570	0.21

Appendix E

Digital imaging correlation technique

E.1 Digital Image Correlation (DIC)

Digital image correlation (DIC) can be used to remotely calculate deformations occurring on the surface of the specimen or member. For concrete specimens or members, these deformations can be used to determine phenomenon such as crack widths or compressive strains. Due to the remote measurement nature of the method, it can be used with great accuracy throughout the mechanical and thermal phases.

Example: measure crack width

Digital image correlation (DIC) was used to calculate the crack widths throughout both the mechanical loading and thermal loading phases. The crack widths were measured by tracking the relative displacement of the concrete on either side of the crack, as shown schematically in Fig. E.1. Digital image correlation was chosen over more traditional methods of crack width measurement because it is a non-contact measurement method that does not affect the thermal properties of the specimen, can be used during heated tests, and does not require the crack positions to be known in advance. Bisby and Take (2009) have previously used the same method to track displacements during experiments on concrete specimens.

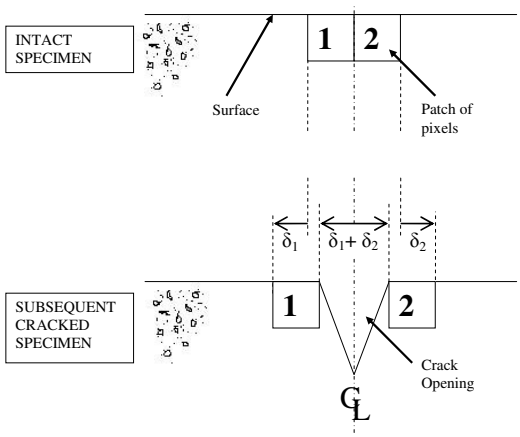

Figure E.1: Example illustrating the concept behind the technique of Digital Image Correlation. This example is for calculating crack widths (not to scale).

The sides of the beam are painted in a high-contrast speckle pattern prior to testing (Fig. E.2), they are lit using halogen lights, and 12 MPixel digital photographs of the constant moment region are recorded at 5s intervals during the tests (Fig. E.3). The images were post-processed using a bespoke image processing algorithm developed by White et al. (2003) to obtain the displacement of patches of pixels just to the left (δ_1) and just to the right (δ_2) of a crack (Fig. E.1). The crack opening width was calculate for each observed crack as ($\delta_1 + \delta_2$).

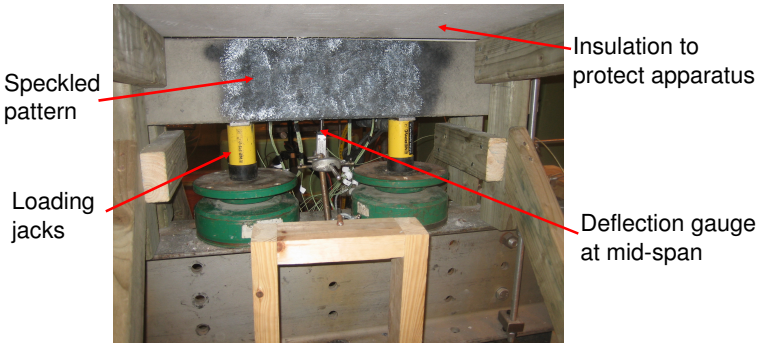

Figure E.2: Photo: The loading set-up used to produce the tensile cracking of the tensile surface. The jacks have a maximum output capacity of 10 tonnes each. The speckled area (black and white pattern) used for displacement measurements is also shown as well as the deflection meter at the mid-span of the beam. Copy from Chapter 3.

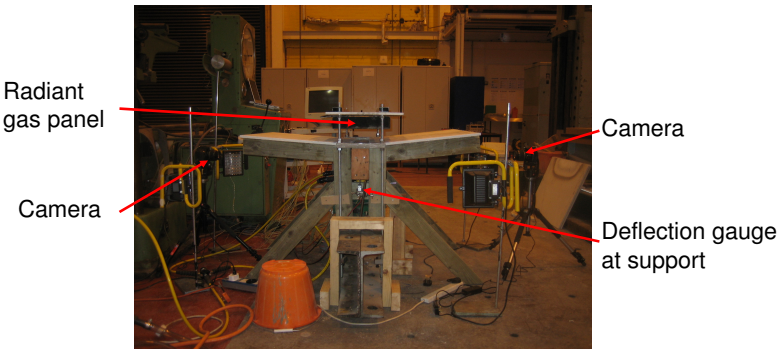

Figure E.3: Photo: Overall set-up for the thermal testing of the tensile cracked beams (before testing commenced), showing the digital image correlation method set-up, support deflection gauges, radiant heat panel and insulation set-up. Copy from Chapter 3.

Appendix F

Study of the radiant heat flux uniformity from the radiant heating panels

When heating the beams as shown in the arrangement in Chapter 6 it was necessary to use two heating panels in parallel due to size requirements. The sample being heated was of dimensions 350x210mm (i.e. heating two beams within their compressed zone). The aim was to provide the beams with an even radiative heat flux, therefore the main variables considered when determining the arrangement were:

(a) - the normal distance from the surface of the radiant panel to the surface of the sample,

(b) - the fuel mixture provide to the radiant panels, and

(c) - the time allotted for the panel to warm up and stabilise.

The variables listed above are not mutually exclusive and as a result, over the course of the study, normal distances ranging from 100mm to 150mm were considered, each with fuel mixtures ranging from a gas mass flow rate 0.5g/s to 0.54g/s while the air flow is kept constant.

It can clearly be seen in Fig. F.1 that when the gas mass flow rate is high (0.54g/s) and there is a relatively large normal distance, the heat flux is quite low, not very

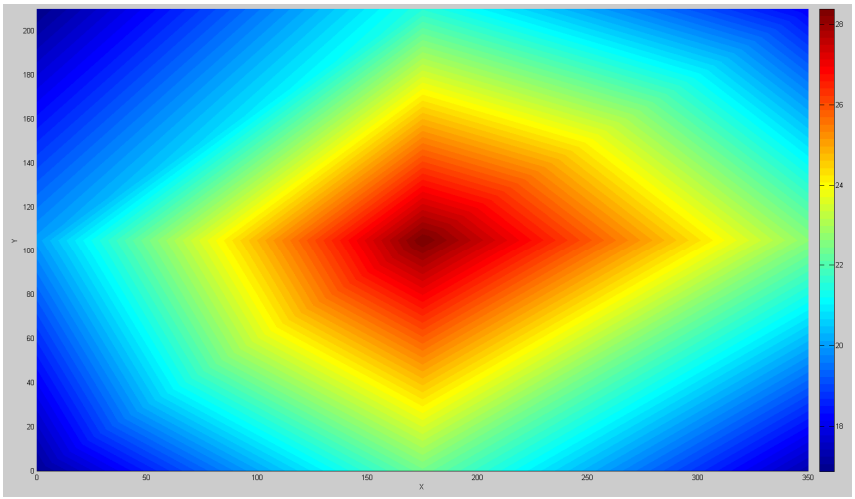

Figure F.1: Plot illustrating the heat flux variation when considering a relatively high gas mass flow rate (0.54g/s) and a relatively large normal distance between the panel and beam surface of 150mm at 30 minutes after ignition. Shows that the distribution is not very uniform and the fluxes produced are quite low and with large variations.

uniform with a hot spot in the center and a variation in heat flux of 32%. On the other hand if the gas mass flow rate is lowered to 0.5g/s and the normal distance is reduced to 100mm (see Fig. F.2), the heat flux becomes more uniform and increases. However, the variation over the area considered is still quite large with a 31% difference bewteen max and min.

Fig. F.3 and Fig. F.4 illustrate the heat flux for the a setup using a gas mass flow rate of 0.5g/s and a normal distance of 120mm for 15min and 30min after ignition respectively. It can be seen that this set up produces a relatively high and uniform heat flux with a variation of only 10%, which stabilises at approximately 15-20 minutes.

It should be noted that the results for this study were obtained by Adam Ervine and Thomas Lowry but Fig. F.1 to Fig. F.4 were compiled by Cristian Maluk with the use of MATLAB.

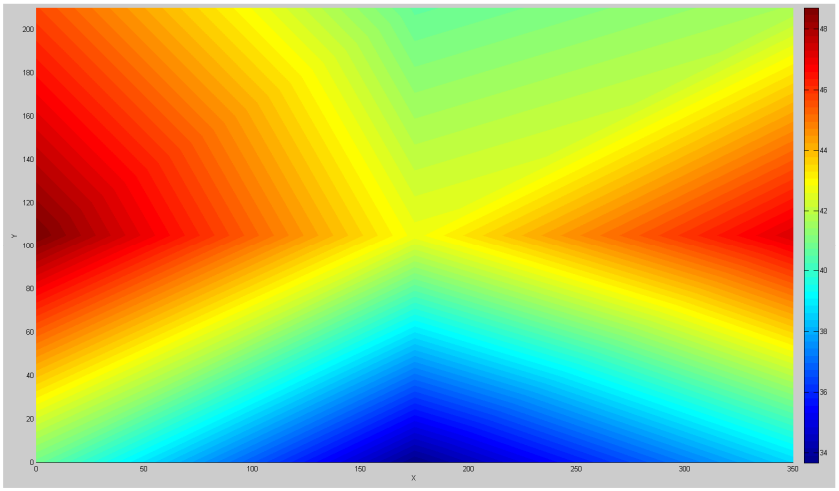

Figure F.2: Plot illustrating the heat flux variation when considering a relatively low gas mass flow rate (0.5g/s) and a relatively small normal distance between the panel and beam surface of 100mm at 30 minutes after ignition. Shows that the distribution has become more uniform and the fluxes produced are relatively high but the variations are high.

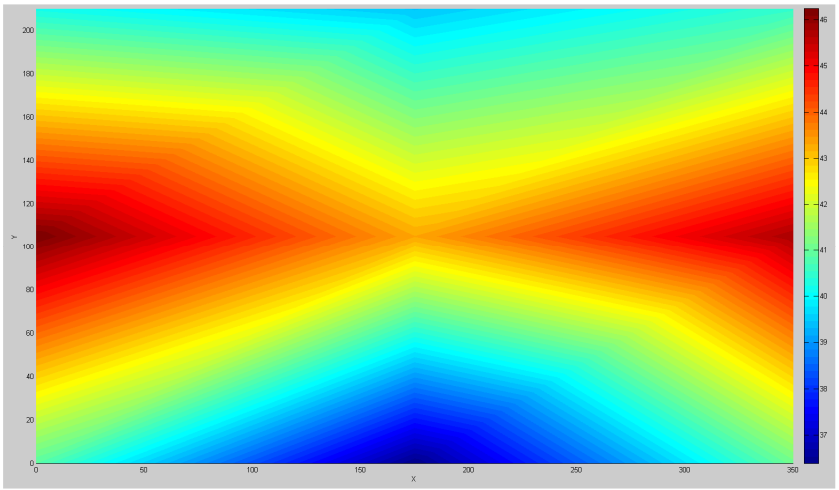

Figure F.3: Plot illustrating the heat flux variation when considering a relatively low gas mass flow rate (0.50g/s) and a normal distance between the panel and beam surface of 120mm at 15 minutes after ignition. Shows that the distribution has become more uniform and the fluxes produced are relatively high with variations that are within 10%.

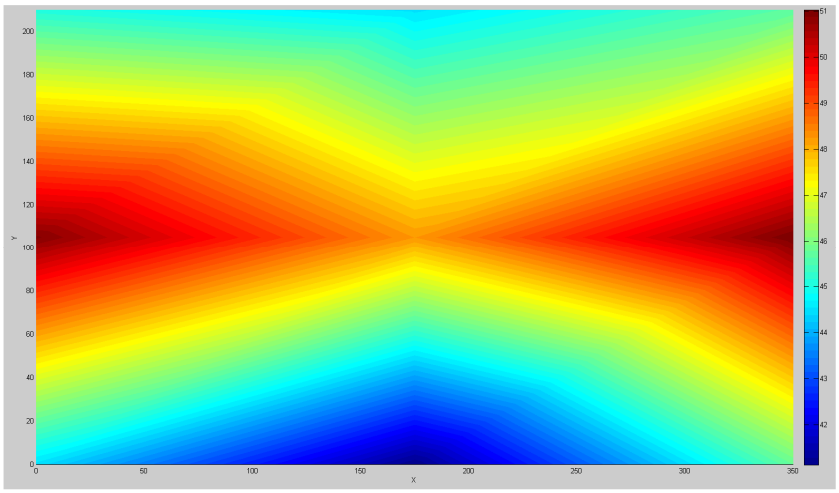

Figure F.4: Plot illustrating the heat flux variation when considering a relatively low gas mass flow rate (0.50g/s) and a normal distance between the panel and beam surface of 120mm at 30 minutes after ignition. Shows that the distribution has remained uniform and the fluxes produced are still relatively high and the variations have remained within 10%.

Appendix G

Numerical convergence study on the element density required for the accurate modelling of bending using solid elements

The use of solid elements to modelling structural bending is not as accurate as using beam elements. This is due to the inherent stiffness of the solid elements. Therefore to use solid elements to model bending accurately and effectively, the element density (number of elements through the section in the direction of bending) needs to be sufficient to overcome the stiffness and yield suitably accurate results.

To determine the element density required for the solid elements to yield suitably accurate results, a small convergence study was carried out as detailed below. A simply supported horizontal perfectly elastic steel beam of 3m span and cross section of 0.3m wide and 0.23m deep was made. The beam was then subjected to a uniformly distributed load of $2x10^6$N/m acting vertically on its top surface as illustrated in Fig. G.1. The dimensions of this beam were chosen to be close in comparison to the dimensions of the numerical models defined in Chapter 4 and Chapter 5.

The beam was then meshed with different mesh densities as defined in Table G.1 and the mid-span deflection measured and compared to the analytical result.

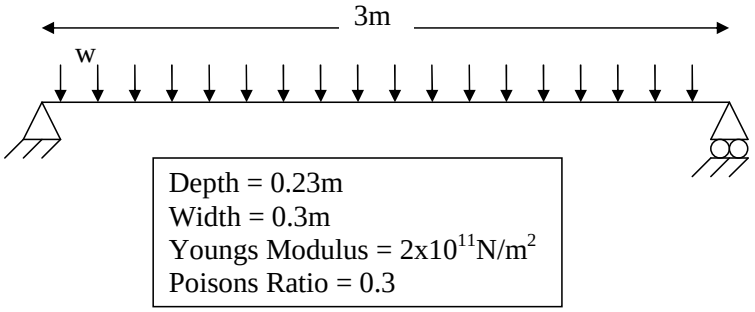

Figure G.1: Illustration of the numerical model set-up. Showing general dimensions and material properties.

Analysis

$$\text{Mid-span deflection,}\delta = \frac{5\omega.L^4}{384EI} \tag{G.1}$$

$$\text{Mid-span deflection,}\delta = \frac{5.2\text{x}10^6.3^4}{384.2\text{x}10^{11}.\frac{0.3\text{x}0.23^3}{12}} \tag{G.2}$$

$$\text{Mid-span deflection,}\delta = 0.0352m \tag{G.3}$$

Table G.1: Summary table showing the mesh density and numerical mid-span deflection of each case and their corresponding % error with the analytical value. The analytical value as calculated above is 0.0352m

Mesh Density (DxL)	Mid-span deflection, m	Error, %
2 x 30	0.0472	34.02
4 x 60	0.03743	6.39
8 x 120	0.0357	1.42
10 x 132	0.0355	0.88
16 x 240	0.0353	0.27

G. NUMERICAL CONVERGENCE STUDY ON THE ELEMENT DENSITY REQUIRED FOR THE ACCURATE MODELLING OF BENDING USING SOLID ELEMENTS

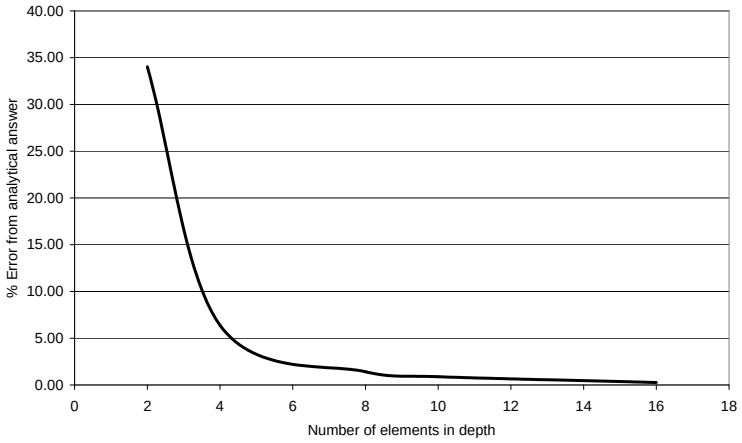

Figure G.2: Plot showing how an increase in element density increases the accuracy of the analysis. It can be concluded that an element density of "10" through the depth, provides a result of reasonable accuracy and will have a reduced computational work load when compared to and element density of "16".

Appendix H

Discussion on the element type for the modelling of reinforced concrete structures under extreme loading conditions

When deciding on the setup and type of numerical model to be used for the simulation of reinforced concrete structures under extreme loading, many variations were attempted before settling on the model defined in Chapter 5. This appendix presents a brief summary of the types of models considered with their pros and cons. It must be noted that all numerical work performed was done within ABAQUS and it is acknowledged that some of the issues may be specific to this program.

From the start, it was realised that the use of solid elements would be computationally intensive. Therefore many different models where considered and tested to determine whether it was possible to produce an accurate simulation with a significantly reduced computational work load.

Beam elements

First considered was to use beam elements to model the concrete which would allow the bending behaviour to be captured easily. As beam elements are one dimensional, no shear reinforcement is required for confinement purposes, and as a result, only

the longitudinal reinforcement needs to be defined. This could be defined in multiple ways. First the reinforcement could be discretely defined and constrained to the beam elements or second, the command "*REBAR" could be used. This *REBAR command places a fictional layer into the beam elements themselves with the properties of steel (or whatever material is considered) to simulate the presence of the reinforcement. This is extremely beneficial as this method will keep the number of DoF's to a minimum and hence, have a low computational work load.

However, it was quickly realised that 3D beam elements can not utilise the concrete damaged plasticity (CDP) model that would be required to capture the complexities of the simulation. Furthermore, although it is possible for beam elements to perform heat transfer along their length are unable to perform a heat transfer analysis through its cross-section. Therefore, beam elements can simply not be used for the simulation of the reinforced concrete structures under extreme loading conditions.

Shell elements

Shell elements were then considered as a step up from beam elements. Like beam elements, shell elements, if orientated correctly, can easily capture the bending behaviour with the in additional capability of utilise the CDP model and perform heat transfer analyses in all directions. Also like beam elements, shell elements do not require the modelling of shear reinforcement and so to can use the *REBAR command.

However, it was realised that although the stress-strain state of the fictional layer that denoted the reinforcement was able to be calculated, transfer of the temperature DoF to this reinforcement did not occur. This meant that the reinforcement remained at ambient temperatures throughout the analysis which was unrealistic.

Another option using shell elements was to discreetly model the reinforcement through the use of truss elements and constrain it to the shell elements in all DoF's. This would allow the transfer of stresses, strains and temperatures into the reinforcement.

However, it must be noted that, while the shell elements have a number of integration (calculation) points throughout their depth, the truss elements have only one integration point. This becomes extremely important when constraining the two elements together. In this case, the entirety of the reinforcement, which has only one DoF becomes constrained to the first DoF of the concrete shell elements. This means that as the thermal boundary condition was applied to the shell elements and a heat transfer analysis was performed, the reinforcement became a uniform temperature throughout equalling the temperature calculated at integration point one within the shell. Therefore, it was concluded that shell elements were not suitable for determining the thermo-mechanical behaviour of a reinforced concrete frame.

Solid elements

Finally, as beam and shell elements were deemed unsuitable for the analyses, solid elements had to be used to model the concrete and truss elements to model the reinforcement. Although this meant that the computational work load was significant, the use of solid elements still easily allowed the capture of the bending behaviour, provided sufficient element density was used as studied in Appendix G, could utilise the CDP material model and perform heat transfer analyses in all directions. Furthermore, the use of solid elements allowed the transfer of all DoF's between the solid elements of the concrete and the truss elements of the reinforcement in the appropriate and realistic manner.

As a further advantage over beam and shell elements, solid modelling has the resolution throughout the members to provide the the analyses with the opportunity to use the subroutine, as detailed in Chapter 4, to simulate the loss of concrete cover.

Appendix I

Numerical model material inputs, including subroutine simulating loss of concrete cover

This section details the material properties used for the numerical modelling that is carried out throughout this thesis.

The steel properties include the rupture properties defined as “damage initiation” and “damage evolution”.

The concrete properties include the softening behaviour in both compression and tension and the damage parameter in compression “D_c” used to alter the elastic stiffness.

The material properties used for the concrete cover is identical to the concrete core except for the properties stated in the following section which include the conductivity, expansion and compression stress-strain behaviour.

I.1 Material model for steel reinforcement

Table I.1: Mechanical properties of steel

Young's Modulus, N/m^2	Poisson's Ratio	Temperature, ^{o}C
2x10^{11}	0.3	20
2x10^{11}	0.3	100
1.8x10^{11}	0.3	200
1.6x10^{11}	0.3	300
1.4x10^{11}	0.3	400
1.2x10^{11}	0.3	500
6.2x10^{10}	0.3	600
2.6x10^{10}	0.3	700
1.8x10^{10}	0.3	800
1.4x10^{10}	0.3	900
8x10^9	0.3	1000
Expansion, x10$^{-5}/^o$C	Temperature, ^{o}C	–
0	20	–
1.25	100	–
1.29	200	–
1.33	300	–
1.37	400	–
1.41	500	–
1.45	600	–
1.49	700	–
1.50	800	–
1.41	900	–
1.34	1000	–

Table I.2: Mechanical properties of steel: continued

Yield stress, N/m^2	Yield strain	Temperature, ^oC
4.15x10^8	0	20
4.15x10^8	0	100
3.59x10^8	0	200
3.93x10^8	0.005	200
4.09x10^8	0.01	200
4.15x10^8	0.0375	200
2.84079x10^8	0	300
3.65724x10^8	0.005	300
3.982x10^8	0.01	300
4.15x10^8	0.038	300
2.30077x10^8	0	400
3.42068x10^8	0.005	400
3.89991x10^8	0.01	400
4.15x10^8	0.038	400
1.91315x10^8	0	500
2.71629x10^8	0.005	500
3.05851x10^8	0.01	500
3.237x10^8	0.038	500
1.02543x10^8	0	600
1.58335x10^8	0.005	600
1.82448x10^8	0.01	600
1.9505x10^8	0.038	600
4.41005x10^7	0	700
7.47433x10^7	0.005	700
8.8325x10^7	0.01	700
9.545x10^7	0.038	700
2.71709x10^7	0	800
3.83225x10^7	0.005	800
4.31353x10^7	0.01	800
4.565x10^7	0.038	800
1.89196x10^7	0	900
2.25463x10^7	0.005	900
2.40931x10^7	0.01	900
2.49x10^7	0.038	900
1.06818x10^7	0	1000
1.42347x10^7	0.005	1000
1.57873x10^7	0.01	1000
1.66x10^7	0.038	1000

Table I.3: Damage properties

		Notes
Damage Initiation, criterion=Ductile	0.1	
Damage evolution, type-displacement	0.0033	Element length=0.03m

Table I.4: Thermal properties of steel

Density, kg/m^2	Temperature, ^{o}C
7850	All temperatures
Conductivity, W/m.K	Temperature, ^{o}C
53.33	20
50.67	100
47.34	200
44.01	300
40.68	400
37.35	500
34.02	600
30.69	700
27.30	800
27.30	900
27.30	1000
Specific heat capacity, J/kg.K	Temperature, ^{o}C
439.80	20
487.62	100
529.76	200
564.74	300
605.88	400
666.50	500
760.22	600
1008.16	700
803.26	800
650	900
650	1000

I.2 Material model for normal concrete

Table I.5: Mechanical properties of concrete

Dilation angle, ^{o}	15	–
Flow potential eccentricity	0.1	–
σ_{b0}/σ_{c0}	1.16	–
K_c	0.667	–
Viscosity parameter, s	0	–
Young's Modulus, N/m^2	Poisson's Ratio	Temperature, ^{o}C
1.79x10^{10}	0.25	20
1.12x10^{10}	0.25	100
7.90x10^9	0.25	200
5.82x10^9	0.25	300
3.80x10^9	0.25	400
2.21x10^9	0.25	500
1.07x10^9	0.25	600
7.70x10^8	0.25	700
4.84x10^8	0.25	800
2.68x10^8	0.25	900
1.07x10^8	0.25	1000
8x10^9	0.25	1000
Expansion, x10$^{-5}/^o$C	Temperature, ^{o}C	–
0	20	–
0.62	100	–
0.66	200	–
0.74	300	–
0.84	400	–
0.97	500	–
1.12	600	–
1.31	700	–
1.52	800	–
1.36	900	–
1.22	1000	–

Table I.6: Compression properties of concrete

Yield stress, N/m^2	Yield strain	Temperature, ^{o}C
8.96414x10^6	0	20
1.74419x10^7	0.0005	20
2.43682x10^7	0.001	20
2.86624x10^7	0.0015	20
3x10^7	0.002	20
89641.4	0.0095	20
8.96414x10^6	0	100
1.74419x10^7	0.0008	100
2.43682x10^7	0.0016	100
2.86624x10^7	0.0024	100
3x10^7	0.0032	100
89641.4	0.0117	100
8.69522x10^6	0.	200
1.69186x10^7	0.0011	200
2.36372x10^7	0.0022	200
2.78025x10^7	0.0033	200
2.91x10^7	0.0044	200
86952.2	0.0139	200
8.15737x10^6	0.	300
1.58721x10^7	0.0014	300
2.21751x10^7	0.0028	300
2.60828x10^7	0.0042	300
2.73x10^7	0.0056	300
81573.7	0.0161	300
7.61952x10^6	0.	400
1.48256x10^7	0.002	400
2.0713x10^7	0.004	400
2.43631x10^7	0.006	400
2.55x10^7	0.008	400
76195.2	0.018	400
6.63347x10^6	0.	500
1.2907x10^7	0.003	500
1.80325x10^7	0.006	500
2.12102x10^7	0.009	500
2.22x10^7	0.012	500
66334.7	0.0195	500

Table I.7: Compression properties of concrete: continued

Yield stress, N/m^2	Yield strain	Temperature, ^oC
5.37849x10^6	0.	600
1.04651x10^7	0.005	600
1.46209x10^7	0.01	600
1.71975x10^7	0.015	600
1.8x10^7	0.02	600
53784.9	0.03	600
3.85458x10^6	0.	700
7.5x10^6	0.01	700
1.04783x10^7	0.015	700
1.23248x10^7	0.02	700
1.29x10^7	0.025	700
38545.8	0.0375	700
2.42032x10^6	0.	800
4.7093x10^6	0.005	800
6.57942x10^6	0.01	800
7.73885x10^6	0.015	800
8.1x10^6	0.02	800
24203.2	0.035	800
1.34462x10^6	0.	900
2.61628x10^6	0.005	900
3.65523x10^6	0.01	900
4.29936x10^6	0.015	900
4.5x10^6	0.02	900
13446.2	0.0375	900
537849	0.	1000
1.04651x10^6	0.005	1000
1.46209x10^6	0.01	1000
1.71975x10^6	0.015	1000
1.8x10^6	0.02	1000
5378.49	0.04	1000

Table I.8: Compression damage properties of concrete

Damage parameter, D	Yield strain	Temperature, ^{o}C
0	0	20
0	0.002	20
0.8	0.0095	20
0	0	100
0	0.0032	100
0.8	0.0117	100
0	0	200
0	0.0044	200
0.8	0.0139	200
0	0	300
0	0.0042	300
0.8	0.0161	300
0	0	400
0	0.008	400
0.8	0.018	400
0	0	500
0	0.012	500
0.8	0.0195	500
0	0	600
0	0.02	600
0.8	0.03	600
0	0	700
0	0.025	700
0.8	0.0375	700
0	0	800
0	0.02	800
0.8	0.035	800
0	0	900
0	0.02	900
0.8	0.0375	900
0	0	1000
0	0.02	1000
0.8	0.04	1000

I. NUMERICAL MODEL MATERIAL INPUTS, INCLUDING SUBROUTINE SIMULATING LOSS OF CONCRETE COVER

Table I.9: Tensile properties of concrete

Yield stress, N/m^2	Yield strain	Temperature, ^oC
$3x10^6$	0	20
$3x10^6$	0.000610444	20
$3x10^6$	0.00154967	20
30000	0.00190767	20
$3x10^6$	0	100
$3x10^6$	0.000510044	100
$3x10^6$	0.00144927	100
30000	0.00180727	100
$2.91x10^6$	0	200
$2.91x10^6$	0.000433699	200
$2.91x10^6$	0.00155158	200
29100	0.00193742	200
$2.73x10^6$	0	300
$2.73x10^6$	0.000386168	300
$2.73x10^6$	0.001718	300
27300	0.00212522	300
$2.55x10^6$	0	400
$2.55x10^6$	0.000245699	400
$2.55x10^6$	0.00186024	400
25500	0.00229495	400
$2.22x10^6$	0	500
$2.22x10^6$	4.70511e-05	500
$2.22x10^6$	0.00125197	500
22200	0.0016935	500

Table I.10: Thermal properties of concrete

Density, kg/m^2	Temperature, ^{o}C
2400	All temperatures
Conductivity, W/m.K	Temperature, ^{o}C
1.951	20
1.765	100
1.552	200
1.361	300
1.191	400
1.042	500
0.915	600
0.809	700
0.724	800
0.661	900
0.619	1000
Specific heat capacity, J/kg.K	Temperature, ^{o}C
900	20
900	100
1000	200
1050	300
1100	400
1100	500
1100	600
1100	700
1100	800
1100	900
1100	1000

I.3 Material model for concrete cover

Table I.11: Mechanical properties of concrete cover

Expansion, x$10^{-5}/^{o}$C	Temperature, ^{o}C	Field variable
0	20	0
0.62	100	0
0.66	200	0
0.74	300	0
0.84	400	0
0.97	500	0
1.12	600	0
1.31	700	0
1.52	800	0
1.36	900	0
1.22	1000	0
0	20	0.00405
0.62	100	0.00525
0.66	200	0.00645
0.74	300	0.00765
0.84	400	0.01005
0.97	500	0.01405
1.12	600	0.02205
1.31	700	0.02705
1.52	800	0.02205
1.36	900	0.02205
1.22	1000	0.02205
0	20	0.00415
0	100	0.00535
0	200	0.00655
0	300	0.00775
0	400	0.01015
0	500	0.01415
0	600	0.02215
0	700	0.02715
0	800	0.02215
0	900	0.02215
0	1000	0.02215

Table I.12: Compression properties of concrete cover

Yield stress, N/m^m	Yield strain	Temperature, ^{o}C
8.96414x10^6	0	20
1.74419x10^7	0.0005	20
2.43682x10^7	0.001	20
2.86624x10^7	0.0015	20
3x10^7	0.002	20
2.18x10^7	0.00405	20
89641.4	0.00415	20
8.96414x10^6	0	100
1.74419x10^7	0.0008	100
2.43682x10^7	0.0016	100
2.86624x10^7	0.0024	100
3x10^7	0.0032	100
2.28x10^7	0.00525	100
89641.4	0.00535	100
8.69522x10^6	0	200
1.69186x10^7	0.0011	200
2.36372x10^7	0.0022	200
2.78025x10^7	0.0033	200
2.91x10^7	0.0044	200
2.28x10^7	0.00645	200
86952.2	0.00655	200
8.15737x10^6	0	300
1.58721x10^7	0.0014	300
2.21751x10^7	0.0028	300
2.60828x10^7	0.0042	300
2.73x10^7	0.0056	300
2.20x10^7	0.00765	300
81573.7	0.00775	300
7.61952x10^6	0	400
1.48256x10^7	0.002	400
2.0713x10^7	0.004	400
2.43631x10^7	0.006	400
2.55x10^7	0.008	400
2.03x10^7	0.01005	400
76195.2	0.01015	400
6.63347x10^6	0	500
1.2907x10^7	0.003	500
1.80325x10^7	0.006	500
2.12102x10^7	0.009	500

Table I.13: Compression properties of concrete cover: continued

Yield stress, N/m^m	Yield strain	Temperature, ^{o}C
2.22x10^7	0.012	500
1.61x10^7	0.01405	500
66334.7	0.01415	500
5.37849x10^6	0	600
1.04651x10^7	0.005	600
1.46209x10^7	0.01	600
1.71975x10^7	0.015	600
1.8x10^7	0.02	600
1.43x10^7	0.02205	600
53784.9	0.02215	600
3.85458x10^6	0	700
7.5x10^6	0.01	700
1.04783x10^7	0.015	700
1.23248x10^7	0.02	700
1.29x10^7	0.025	700
1.08x10^7	0.02705	700
38545.8	0.02715	700
2.42032x10^6	0	800
4.7093x10^6	0.005	800
6.57942x10^6	0.01	800
7.73885x10^6	0.015	800
8.1x10^6	0.02	800
6.99x10^6	0.02205	800
24203.2	0.02215	800
1.34462x10^6	0	900
2.61628x10^6	0.005	900
3.65523x10^6	0.01	900
4.29936x10^6	0.015	900
4.5x10^6	0.02	900
3.97x10^6	0.02205	900
13446.2	0.02215	900
537849	0	1000
1.04651x10^6	0.005	1000
1.46209x10^6	0.01	1000
1.71975x10^6	0.015	1000
1.8x10^6	0.02	1000
1.62x10^6	0.02205	1000
5378.49	0.02215	1000

Table I.14: Thermal properties of concrete

Conductivity, W/m.K	Temperature, ^{o}C	field variable
1.951	20	0
1.765	100	0
1.552	200	0
1.361	300	0
1.191	400	0
1.042	500	0
0.915	600	0
0.809	700	0
0.724	800	0
0.661	900	0
0.619	1000	0
1.951	20	0.00405
1.765	100	0.00525
1.552	200	0.00645
1.361	300	0.00765
1.191	400	0.01005
1.042	500	0.01405
0.915	600	0.02205
0.809	700	0.02705
0.724	800	0.02205
0.661	900	0.02205
0.619	1000	0.02205
1951	20	0.00415
1765	100	0.00535
1552	200	0.00655
1361	300	0.00775
1191	400	0.01015
1042	500	0.01415
915	600	0.02215
809	700	0.02715
724	800	0.02215
661	900	0.02215
619	1000	0.02215

I.4 Subroutine incorporated for simulating loss of concrete cover

```
c
dimension jElem(nblock), coordMp(nblock,*),
* direct(nblock,3,3), T(nblock,3,3),
* charLength(nblock), props(nprops),
* stateOld(nblock,nstatev),
* stateNew(nblock,nstatev),
* field(nblock,nfieldv)
character*80 cmname
c
c     Local arrays from vgetvrm are dimensioned to
c     maximum block size (maxblk)
c
parameter( nrData=6 )
character*3 cData(maxblk*nrData)
dimension rData(maxblk*nrData), jData(maxblk*nrData)
c
jStatus=1
call VGETVRM('PEEQ',rData, jData, cData, jStatus)
call setField( nblock, nstatev, nfieldv, nrData,
* rData, stateOld, stateNew, field)
c
return
end
c
subroutine setField( nblock, nstatev, nfieldv, nrData,
* strain, stateOld, stateNew, field )
```

```
c
include 'vaba_param.inc'
c
dimension stateOld(nblock,nstatev), stateNew(nblock,nstatev),
* field(nblock,nfieldv), strain(nblock,nrData)
c
do k = 1, nblock
stateNew(k,1)=stateOld(k,1)
c
c     Value of maximum principle plastic strain (3D):
PEEQ = strain(k,1)
c
Oldf = field(k,1)
c
if(PEEQ.le.Oldf)then
field(k,1) = Oldf
else
field(k,1) = PEEQ
endif
c
c     Store the maximum plastic strain as a solution dependent
c     state variable
stateNew(k,1) = field(k,1)
c
end do
c
return
end
```

Appendix J

Calculations of the applied loading for the "case study" frame

It should be noted that all dead loads produced by the frame is taken account of by specifying a density and applying gravity loading directly to the frame.

J.1 Load placed on top of the slab

The load applied to the slab directly is a purely the live loading with the addition of the floor finishing that is applied to that floor only.

$$\text{Pressure} = 2000 + 1000 \tag{J.1}$$

$$\text{Pressure} = 3000N/m^2 \tag{J.2}$$

J.2 Load placed on top of the columns

Dead loading

$$\text{Slab} = \text{Thickness x Area x Density} \tag{J.3}$$

$$\text{Slab} = 0.12\text{x}(3\text{x}3)\text{x}25 = 27kN \tag{J.4}$$

$$\text{Three slab levels} = 3\text{x}27 = 81kN \tag{J.5}$$

$$\text{Beams} = \text{Width x depth x Length x Density} \tag{J.6}$$

$$\text{Beams} = 0.11\text{x}0.23\text{x}5.4\text{x}25 = 3.42kN \tag{J.7}$$

$$\text{Three beam levels} = 3\text{x}3.42 = 10.25kN \tag{J.8}$$

$$\text{Floor finishes} = \text{Area x Density} \tag{J.9}$$

$$\text{Floor finishes} = (3\text{x}3)\text{x}1 = 9kN \tag{J.10}$$

$$\text{Three floor levels} = 3\text{x}9 = 27kN \tag{J.11}$$

$$\text{Columns} = \text{Width x Breath x Length x Density} \tag{J.12}$$

$$\text{Columns} = (0.3\text{x}0.3)\text{x}3\text{x}25 = 6.88kN \tag{J.13}$$

$$\text{Three lengths } = 3\text{x}6.88 = 20.64kN \tag{J.14}$$

$$\text{Total dead loading on columns} = 81 + 10.25 + 27 + 20.64 = 138.89kN \tag{J.15}$$

J. CALCULATIONS OF THE APPLIED LOADING FOR THE "CASE STUDY" FRAME

Live loading

$$\text{Live load on floors} = \text{Loading x Area} \tag{J.16}$$

$$\text{Live load on floors} = 2\text{x}(3\text{x}3) = 18kN \tag{J.17}$$

$$\text{Three floor levels} = 3\text{x}18 = 54kN \tag{J.18}$$

$$\text{Total live loading on columns} = 54kN \tag{J.19}$$

Total pressure on top of columns

$$\text{Pressure} = \frac{\text{Dead + Live}}{\text{Area}} \tag{J.20}$$

$$\text{Pressure} = \frac{(138.89 + 54)\text{x}1000}{(0.3\text{x}0.3)} \tag{J.21}$$

$$\text{Pressure} = 2.143\text{x}10^6 N/m^2 \tag{J.22}$$